

SUBPICOSECOND ELECTRO-OPTIC SAMPLING

by

Janis A. Valdmanis

**Submitted in Partial Fulfillment
of the
Requirements for the Degree**

DOCTOR OF PHILOSOPHY

**Supervised by Professors Conger W. Gabel and Gerard Mourou
The Institute of Optics**

**University of Rochester
Rochester, New York**

1983

CURRICULUM VITAE

Janis A. Valdmanis was born in Old Windsor, England on June 10, 1956 and emigrated to the United States in 1967. He attended Purdue University from 1974 until 1978 and was granted the B.S. in both Physics (with honors) and Mathematics. In the fall of 1978, he entered the Ph.D. program at the University of Rochester's Institute of Optics. During his first year of graduate study, Mr. Valdmanis was a fellow of the Institute of Optics. Since that time, he has been a fellow of the Laboratory for Laser Energetics, working toward the Ph.D. in Optics under the supervision of Professors Conger W. Gabel and Gerard Mourou. Mr. Valdmanis is also a member of the Optical Society of America.

ACKNOWLEDGEMENTS

It is a genuine pleasure to acknowledge the invaluable expertise of my advisors, Professors Conger W. Gabel and Gerard Mourou. In the course of this thesis work, they have greatly influenced my development both personally and as a scientist. I consider myself extremely fortunate to have spent my graduate career under their enthusiastic guidance.

Many thanks go to the students, faculty and staff of both the Institute of Optics and the Laboratory for Laser Energetics with whom I have had discussions or from whose technical skills I have benefited. Special thanks must go to all the members of Gerard's picosecond group for their assistance and cooperation in the ultrafast lane and also to Bob Keck for sharing his experience in the digital world.

I would also like to express my gratitude to the Institute of Optics and the Laboratory for Laser Energetics for their financial support during my stay at the University.

Above all, I am thankful to my parents for their constant encouragement and belief in my ability throughout my scholastic career.

Milš paldies

ABSTRACT

This dissertation documents the development of a novel, state of the art optical sampling technique for the characterization of picosecond electrical transients. The technique is based upon the interaction of subpicosecond optical pulses and the unknown electrical transient in a traveling-wave Pockels cell employed as an ultrafast intensity modulator. All facets of the design, construction, performance, and application of the system are discussed. A theoretical model for temporal performance is also introduced and applied to the experimental situations.

The Pockels, or electro-optic, sampling technique discussed here has significantly extended the regime of electrical signal analysis in the picosecond domain and is the only technique that has achieved a subpicosecond temporal resolution. The technique exploits the availability of high repetition rate, subpicosecond, mode-locked laser pulses and the ultrafast response of the Pockels effect (a special case of parametric three-wave mixing).

The system, to date, has achieved a temporal resolution of 550 femtoseconds, in excellent agreement with the results of the theoretical model. The theory indicates that resolutions of near 200 femtoseconds should be attainable. The high repetition rate of the sampling process (91 MHz)

enables the use of signal averaging techniques to enhance the sensitivity of the Pockels effect. With signal averaging, sensitivities of better than 100 μV have been observed.

TABLE OF CONTENTS

	Page
CURRICULUM VITAE	ii
ACKNOWLEDGEMENTS	iii
ABSTRACT	iv
TABLE OF CONTENTS	vi
LIST OF TABLES	ix
LIST OF FIGURES	x
CHAPTER	
I. INTRODUCTION	1
A. Motivation	1
B. High speed electrical measurement schemes ..	2
1. Measurement system parameters	3
2. Conventional oscilloscopes	6
3. Sampling oscilloscopes	9
4. Superconducting sampling	12
5. Indirect optical (photoconductive) sampling	12
6. Summary	16
C. Overview of dissertation	17
II. THEORY OF ELECTRO-OPTIC SAMPLING	20
A. Introduction to direct electro-optic sampling	20
B. The electro-optic effect	24
1. The electro-optic mechanism	25

	Page
2. Intensity modulation	35
3. Electro-optic material properties	43
4. Lithium tantalate modulators	50
C. The traveling-wave Pockels cell	56
1. Stripline electrical characteristics ...	57
2. The electro-optical interaction and resolution	71
D. Noise, sensitivity and signal processing ...	87
E. Transient sampling theory	98
III. THE EXPERIMENT	103
A. The experimental arrangement	103
1. The sampling heads	104
2. The CPM dye laser system	110
3. The system configuration	114
B. Experimental operation	120
1. Calibration	120
2. Measurement procedure	125
C. Experimental results	128
1. Basic system characteristics	130
a. Linearity	130
b. Sensitivity	130
c. Stability and time constant effects	134
2. Bandwidth	136
3. Electrical dispersion	152

	Page
4. Applications	162
a. The effective dielectric constant ..	162
b. Cable and connector bandwidths	167
c. Indium phosphide detectors	169
D. Experimental noise limits to sensitivity ...	172
IV. SUMMARY	178
APPENDICES	
A. LASER PULSEWIDTH MEASUREMENT	182
B. THE PHOTOCONDUCTIVE EFFECT	186
REFERENCES	191

LIST OF TABLES

Table		Page
I-1	Comparison of high speed measurement techniques	18
II-1	Modulator parameters	62
III-1	Sampling head halfwave voltages	123

LIST OF FIGURES

Figure		Page
I-1	Definition of risetime, T	4
I-2	Oscilloscope deflection plates	7
I-3	Sampling waveforms	10
I-4	Indirect optical (photoconductive) sampling	14
II-1	Direct optical sampling	22
II-2	General behaviour of the dielectric constant versus frequency	28
II-3	Index ellipsoid for a uniaxial crystal	34
II-4	Intensity modulator transmission function	37
II-5	Transverse electro-optic modulator geometry	39
II-6	Transmission function slope versus polarizer extinction ratio	42
II-7	Dispersion of the optical indices for lithium tantalate	45
II-8	Lithium tantalate electro-optic tensor	46
II-9	Transverse modulator geometry	47
II-10	Indicatrix distortion due to an applied electric field	47
II-11	Traveling-wave modulators	53
II-12	Velocity matching geometry	54
II-13	Comparison of microstrip and balanced transmission lines	58

Figure		Page
II-14	Modulator electrode configuration	61
II-15	Behaviour of modulator parameters as a function of the electrode aspect ratio	63
II-16	Behaviour of modulator parameters as a function of frequency	67
II-17	Frequency dependence of the dielectric constant as a function of aspect ratio	69
II-18	Waist size and rayleigh range for a focussed gaussian beam	73
II-19	Pulse propagation through the modulator crystal	74
II-20	Detail of the velocity matching geometry	76
II-21	Comparison of gaussian beam waist sizes in air and in the crystal	80
II-22	Temporal resolution as a function of the incident angle	81
II-23	Temporal resolution as a function of the incident angle	82
II-24	Sources of noise in the detection circuitry	89
II-25	Differential detection arrangement for noise subtraction	96
II-26	Electrical signals at various points of the sampling system	99

Figure		Page
III-1	Optical and electrical field orientation within the electro-optic crystal	105
III-2	The electro-optic crystal mount	107
III-3	Connector and crystal configuration	107
III-4	Sampling head configuration for an external signal source	109
III-5	Sampling head configuration for an integrated signal source	111
III-6	Colliding pulse mode-locked laser schematic and typical auto-correlation trace	113
III-7	The complete electro-optic sampling system	116
III-8	Detector bias and conditioning circuitry	118
III-9	Risetime limit as a function of delay line speed and lock-in amplifier time constant	129
III-10	Demonstration of modulator response linearity	131
III-11	Typical system output trace	132
III-12	Demonstration of system stability	135
III-13	Measurement of a 210 fs delay	135
III-14	Demonstration of risetime as a function of time constant, TC	137
III-15	Demonstration of the ability to time-resolve direct and indirect (reflected) modes	140

Figure	Page
III-16 Demonstration of the effects of optical beam position and orientation	142
III-17 Demonstration of the effects of crystal thickness and optical beam spot size	145
III-18 Geometry for the observation of higher order modes	148
III-19 Trace of a 550 fs effective risetime and the associated electrode geometry	149
III-20 Fourier transform of a 550 fs risetime signal ..	151
III-21 Geometry for investigating stripline dispersive effects	153
III-22 Progressive dispersion in the 500 μm thick modulator	155
III-23 Progressive dispersion in the 250 μm thick modulator	156
III-24 Progressive dispersion in the 100 μm thick modulator	157
III-25 Comparison of the dispersive effects for the 500 μm and 250 μm thick modulators	160
III-26 Electrical dispersion in the 100 μm thick modulator	161
III-27 Delayed traces for measurement of the effective dielectric constant	164

Figure	Page
III-28	Sampling geometry and corresponding trace for the characterization of the dielectric constant 166
III-29	Characterization of cable and connector bandwidths 168
III-30	Sampling geometries and the associated traces for two indium phosphide detectors 171
III-31	CPM laser noise spectrum 176
A-1	Scanning auto-correlator configuration and a typical trace from the CPM dye laser 183
B-1	Photoconductive detector geometry and the circuit equivalent 187

CHAPTER I

INTRODUCTION

I.A. Motivation

The availability of picosecond and subpicosecond optical pulses as generated by mode-locked lasers¹⁻⁴ has made possible the investigation of material processes in the picosecond time regime. For the most part, these studies have been of an optical nature.⁷⁵ Recently, however, an increasing amount of research is being conducted in the investigation and development of picosecond electronic materials and devices. Examples include photodetectors, photoconductive materials, and ultrafast transistors. Successful development of these new devices requires a measurement system with the ability to characterize electrical performance on a picosecond time scale.

It is well known that sampling techniques for electrical signal characterization provide superior temporal performance. In sampling systems, the temporal resolution, ideally, is determined by the duration of the sampling gate. Hence, a high resolution sampling system requires a narrow sampling gate width. For many years now, measurement techniques have been dependent on electronic sampling gates having durations of no less than 25 picoseconds. In this thesis, we propose and investigate a novel, alternative,

sampling technique that is based upon the direct use of sub-picosecond optical pulses as the sampling gates.⁵⁻⁷ We can exploit the availability of such ultrashort optical pulses by employing electro-optic crystals as an interaction medium for the optical and unknown electrical signals. The electro-optic, or Pockels, effect is ideally suited for picosecond sampling because the mechanism responsible for the effect poses no temporal response limit, even into the femtosecond regime. Thus, the direct use of optical pulses enables us to achieve a similar subpicosecond temporal resolution for sampling electrical signals.

Experimental results verify the attainment of an unprecedented temporal resolution of approximately 500 femtoseconds, which represents an improvement of almost two orders of magnitude over conventional electronic sampling systems.

I.B. High speed electrical measurement schemes

This section reviews several existing techniques for the measurement of high speed electrical signals. We begin by discussing the important parameters of any electrical measurement technique. These parameters will then be used as a basis for comparing the variety of current technologies to the new technique developed in this thesis. Since we are most interested in high speed performance, the limiting tem-

poral effects of each technique will be emphasized.

I.B.1. Measurement system parameters

Most electrical measurement systems measure voltage as a function of time. Since "voltage" per se cannot be "seen" by a human observer, the measurement system can be considered to be a device that converts voltage to another type of "secondary" signal that allows the waveform to be either directly visualized, or recorded, or both. Ideally, the secondary signal should generate an exact, noise free, replica of any input waveform both in time and amplitude. The ideal case, however, is never achieved.

The accuracy with which a real system can actually measure an unknown waveform is usually described by the following parameters: temporal resolution (related to bandwidth), sensitivity, and dynamic range. A measure of the temporal response for any system is the temporal resolution which we will denote as τ . Given a perfect step function as the input signal, τ is defined as the risetime of the secondary or output signal. Usually, the risetime is measured between the 10% and 90% points of the rising signal as shown in Figure I-1. Thus, τ is a measure of the speed of the conversion process. The shorter τ becomes, the more ideal the temporal conversion. The reciprocal of τ yields an equivalent frequency, f_{\max} , that corresponds to the maximum resolvable frequency and is defined as:

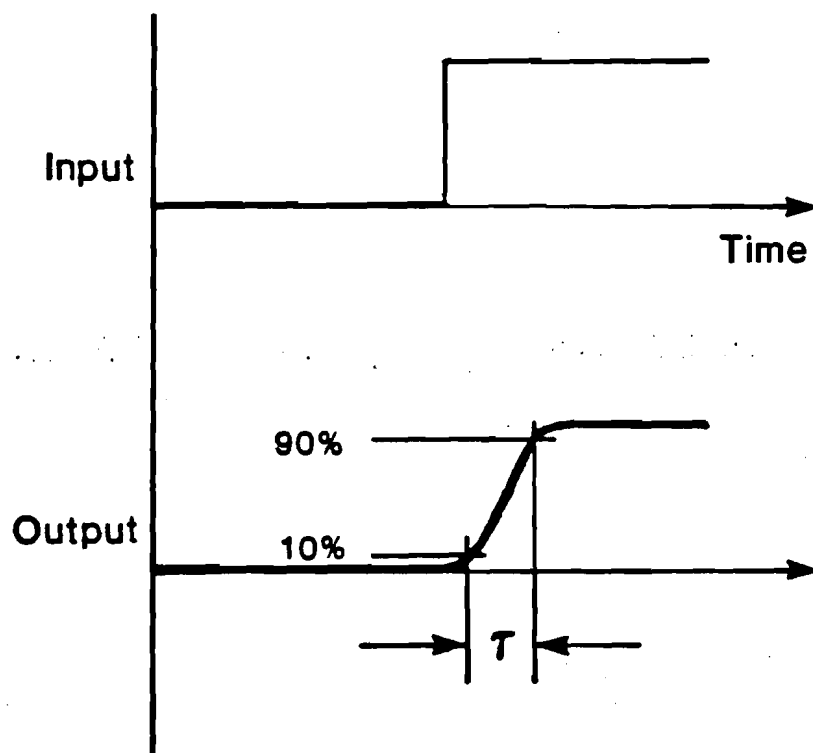


Figure I-1 Definition of risetime, T

$$f_{\max} = \frac{0.35}{\tau}.$$

I-1

Another way of expressing the temporal performance is the bandwidth, B. The bandwidth is defined as the frequency range over which the conversion process is constant with frequency. If the low frequency range of a converter extends to DC, as is often times the case, then the bandwidth is simply f_{\max} .

Minimum sensitivity is commonly defined as the applied voltage level that yields a signal to noise ratio of unity in the secondary signal. A lower sensitivity figure allows one to measure smaller input signals. The dynamic range refers to the range of voltages that can be accurately measured, which in turn defines the maximum voltage to which the system responds linearly.

In the ideal case,⁷⁶ both the minimum sensitivity and the temporal resolution, τ , of a measurement system would be infinitely small. A $\tau=0$ implies an interaction time of zero for the conversion process. Experimentally, however, we find that to achieve a reasonable sensitivity, the conversion interaction must take a FINITE amount of time. As a result of this finite interaction time, the secondary signal is no longer a perfect replica of the input signal either in time or amplitude. These imperfections manifest themselves as either a limited high frequency capability or a reduction

in sensitivity. However, as will be seen in most cases, the temporal inaccuracy is traded off against the sensitivity in order to satisfy the specific experimental requirements. As will be seen, for many devices, \mathcal{T} is exactly the interaction time between the voltage and the secondary signal. More complex devices (eg. traveling-wave oscilloscopes) can attain a \mathcal{T} significantly less than the interaction time, and in doing so, increase their frequency response without sacrificing sensitivity.

I.B.2. Conventional oscilloscopes

The most common, and by far the most versatile, voltage waveform measuring device is the conventional cathode ray oscilloscope. It accepts an input voltage and converts it to a luminous plot of voltage versus time on a fluorescent screen. The secondary signal is an electron beam focussed onto the screen. The conversion is from voltage to deflection of the electron beam. The deflection is accomplished by propagating the beam of electrons through two orthogonal sets of deflection plates. The horizontal set is used to generate the temporal axis, while the vertical set has an amplified voltage replica of the input signal applied to it.

The ultimate limit in temporal response for a conventional oscilloscope is dictated by its vertical deflection plate geometry.⁸ A typical geometry is represented in Figure I-2. An electron traveling between the plates experiences a

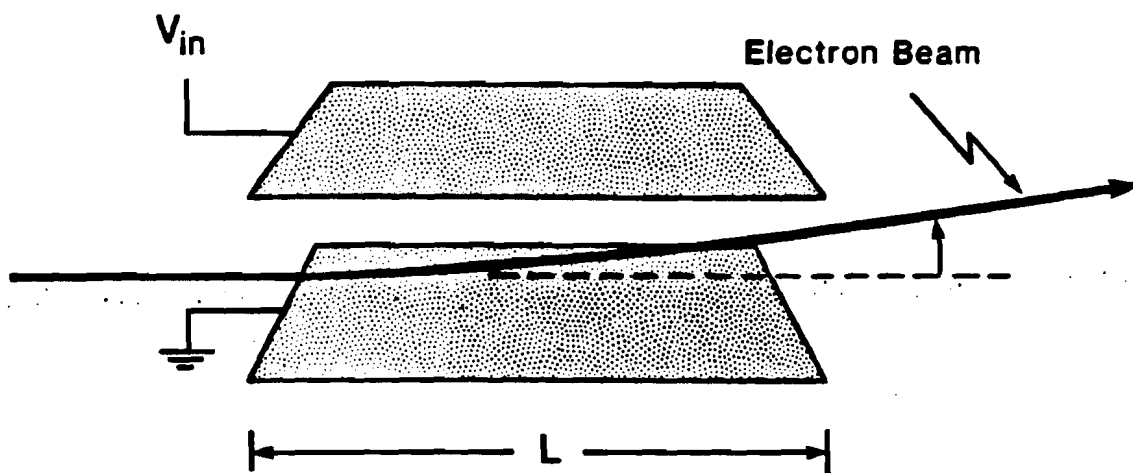


Figure I-2 Oscilloscope deflection plates

deflection proportional to both the input voltage, V_{in} , and the length of the plates, L . If the time an electron spends between the plates (transit time) is short compared to the temporal characteristics of V_{in} , then an accurate replica of the input voltage waveform will be generated. Distortion arises when V_{in} varies on a time scale less than the electron transit time, in which case an electron experiences a changing field as it passes through the plates.

Consider the application of a perfect step function to the plates. The deflection a particular electron experiences depends upon where it is with respect to the deflection plates at the onset of the step. If it is between the plates when the step function arrives, then its deflection will be proportional to the remaining distance it must travel through the plates. It can be shown that the resulting risetime, τ , is equal to the electron transit time through the plates. This effect is referred to as the transit time limitation for temporal resolution, and is an example of τ being equal to the interaction time. The fastest oscilloscopes of this type have a τ on the order of one nanosecond. To obtain better temporal resolution, L must be shortened and hence, sensitivity is sacrificed.

The problem of the transit time limitation is solved in most cases by some form of traveling-wave system. Here the deflection plates are either broken up into a number of seg-

ments or formed into a coiled helixical line so that the signal travels parallel to the electron beam at the same speed as the electrons. Thus, any electron is deflected by the same signal component throughout its entire interaction time. Typical maximum frequencies that can be resolved using traveling-wave oscilloscopes are on the order of a few gigahertz which corresponds to a resolution approaching 100 picoseconds. Sensitivities tend to be extremely poor, ranging from a few volts to several tens of volts per trace width as compared with about 1 mV for many conventional slower oscilloscopes. Temporal limitations arise from difficulties encountered in coupling high frequency signals into the complex deflection structures and also in generating the high frequency horizontal sweep.

I.B.3. Sampling oscilloscopes

A different approach is possible when the signal to be observed is repetitive. This approach involves an amplitude sampling technique using a short gating pulse of about 25 ps duration. The basic waveforms are illustrated in Figure I-3. Samples of the input signal are taken at ever increasing times, T , at each recurrence of the signal. Thus, the conversion process is not continuous, as in the oscilloscope, but rather is an accumulation of discrete portions, or samples. These samples are amplified, lengthened in time, and subsequently displayed on a conventional oscillo-

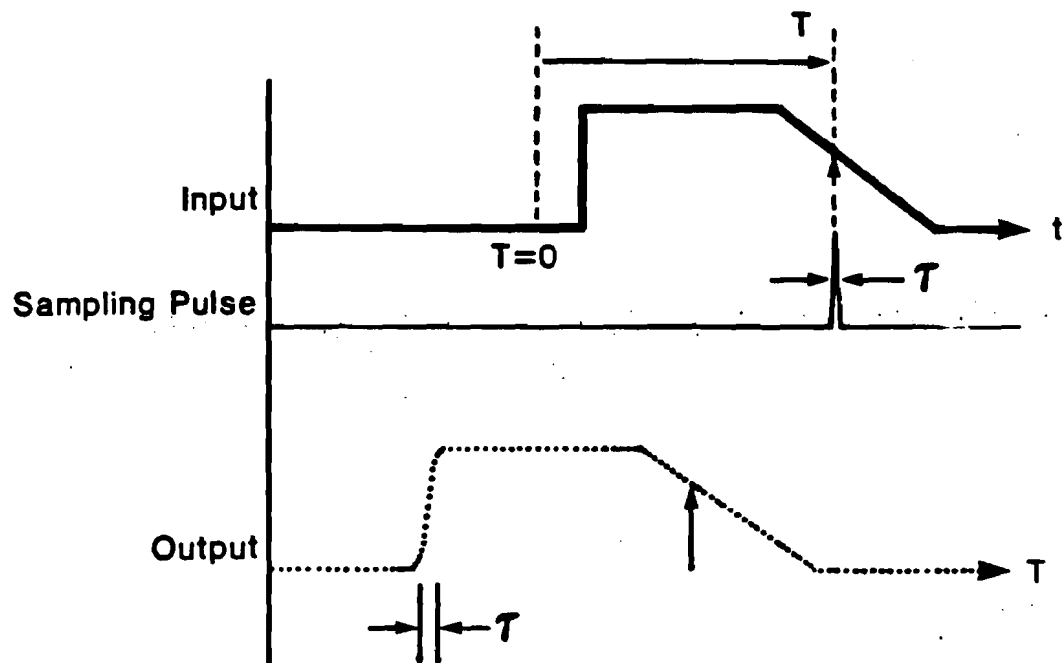


Figure I-3 Sampling waveforms

scope as a function of T . The sampling process allows the oscilloscope to operate at a sweep speed much slower than would be required to observe the signal directly.

The temporal resolution of the sampling technique is, however, still dictated by the interaction time. Here, the input signal interacts with the sampling gate pulse to generate the proportional sample voltage. The temporal resolution, \mathcal{T} , is therefore determined solely by the sampling pulse width, and manifests itself as a risetime in exactly the same way as before. Figure I-3 shows the resultant risetime of \mathcal{T} given a step function input.

The best sampling oscilloscopes developed to date have specified temporal resolutions of 25 ps,⁹ but due to temporal instabilities that randomly vary the position of the sampling pulse, called jitter, the effective resolution is reduced to approximately 100 ps. Sensitivity is on the order of a few millivolts with a linearity range limited to about 10 V. In addition, spurious signals of a few millivolts in amplitude and several nanoseconds in duration can be emitted from the input of the sampling gate¹⁰ possibly interfering with the input signal. The sampling oscilloscope has been used for many years not only because of its availability, but also because of the lack of a better alternative.

I.B.4. Superconducting sampling

Due to efforts to increase the speed of computer circuits, much work has been done in the field of superconductive switches. Some switches, known as Josephson devices (JD), combine high speed operation with low-power dissipation, but being superconductive, require a cryogenic environment. Recently, Faris¹¹ has demonstrated that current pulses in the picosecond regime can be generated and measured using JD's as sampling gates. Tuckerman,¹² subsequently has employed similar JD's as sampling gates to develop a sampling system that has achieved a temporal resolution of under 10 ps with a sensitivity of near 10 μ V. The major obstacle, of course, is the cryogenic environment which presents great difficulties in being able to couple high speed signals into or out of the sampling device. A 10 GHz transmission line to room temperature has been implemented, but otherwise the sampler is limited to analyzing high speed signals that are generated within the low temperature environment.

I.B.5. Indirect optical (photoconductive) sampling

An attractive alternative to conventional sampling gates are photoconductive switches. These devices are based on semi-insulating materials that become conducting when they absorb light. The photoconductivity process can be exceedingly fast, and if the activating light is in the form

of picosecond pulses, then many photoconductors can be employed as sampling gates on the same time scale. The photoconductive switch is essentially a direct replacement for the conventional electronic sampling gate, operated in an entirely analogous manner.

Figure I-4 depicts a typical sampling arrangement employing a photoconductive gate.¹³ A train of picosecond optical pulses is generated by a mode-locked laser and divided in two. The beam splitter yields two perfectly synchronized pulse trains. An unknown waveform is optically triggered by one of the trains and propagated along a strip transmission line that has a photoconductive material positioned somewhere along its length. As the signal passes the photoconductor, an optical pulse from the second train illuminates the gate and allows a sample of the unknown signal to be extracted along a second transmission line. Successive samples of the signal are accumulated and averaged. The sampling process occurs at the repetition rate dictated by the pulse train, which is typically around 100 MHz. A proportional replica of the unknown signal is generated by varying the relative delay between the two pulse trains, while mapping the sampled values as a function of the delay.

The most significant aspect of this sampling scheme that differentiates it from previous methods is that it is optically controlled. The use of optical pulses coupled

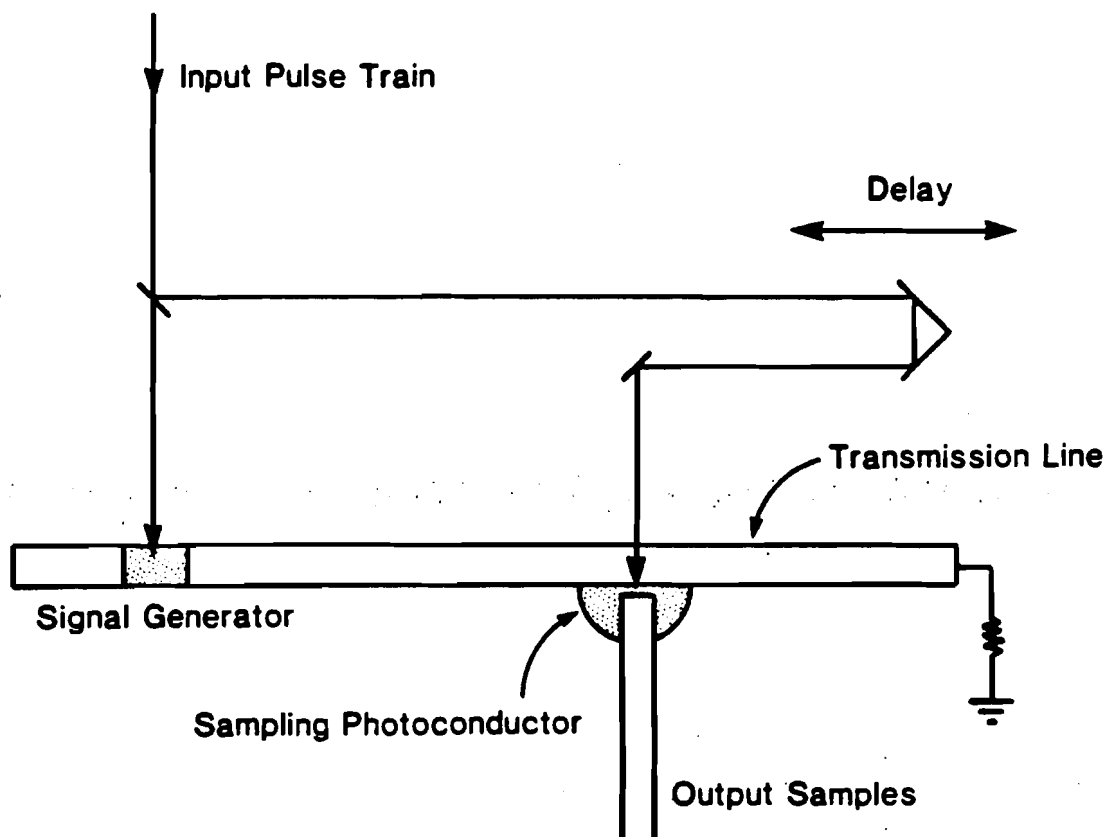


Figure I-4 Indirect optical (photoconductive) sampling
(see Reference 13)

with the photoconductive effect leads to several distinct advantages over conventional electronic sampling schemes.

The temporal resolution, τ , for photoconductive sampling is precisely the duration of the photo-induced conductivity, which is determined by the length of the optical pulse and the photoconductive material characteristics. It has been shown (see Appendix B) that the risetime of the gating pulse follows the integral of the optical excitation pulse, while the fall time is generally dictated by carrier recombination kinetics of the photoconductor. Many materials have been investigated,¹⁴⁻¹⁶ but the most recent work by Auston¹⁷ indicates that gate widths, and hence temporal resolutions, of less than three picoseconds have been obtained by using radiation damaged silicon as the photoconductor. We refer to this gating technique as "indirect" optical sampling, because the sampling gate, although optically triggered, still depends on electronic material parameters to determine its ultimate duration.

Due to the integral relationship between the optical pulse and the gating pulse, there is essentially no jitter between the two signals. If the unknown signal can also be generated in a jitter-free manner with respect to its optical triggering pulse, then the timing between the signal and the sampling gate also becomes free of jitter. The precise synchronism between signals enables the temporal resolution

to be truly limited by only the gate width and not by fluctuating relative waveform positions, as was the case in electronic sampling.

Several systems utilizing photoconductors as sampling gates have been experimentally investigated and implemented.^{10,13,16,18} Auston and Smith^{16,19,20} have demonstrated the versatility of their system by characterizing the electrical behaviour of high-speed semi-conductors, photodetectors and field-effect transistors. The voltage sensitivity of this method is excellent due to the inherently low-noise nature of photoconductive devices. Sensitivities as low as $10\text{ }\mu\text{V}$ can be attained with the use of signal averaging techniques.¹³

I.B.6. Summary

We have found that conventional oscilloscopes, although extremely versatile, have temporal resolutions limited to the regime of greater than several hundred picoseconds. Sampling oscilloscopes, employing electronic sampling gates can attain effective temporal resolutions near 25 ps but are limited by jitter and noise in the sampling circuitry. Superconducting electronics is able to sample with better than 10 ps resolution, but only in the severely restricted cryogenic environment. The best temporal resolution achieved before the work described in this dissertation, employs picosecond optical techniques to control photocon-

ductive sampling gates (indirect optical sampling). Although the precision of optical control and triggering is exploited, the temporal resolution of 3 ps that has been achieved is still limited by material parameters. Table I-1 summarizes the key parameters for the variety of measurement systems and techniques we have considered in this review. The table also includes the achievements of this thesis work on electro-optic sampling for comparative purposes.

I.C. Overview of dissertation

Chapter II begins by introducing the concept of direct electro-optic sampling. This is followed by a discussion of the electro-optic effect. We consider its suitability for sampling electrical signals and the method of implementation. Several electro-optic materials and types of high speed modulators are compared resulting in the decision to use lithium tantalate in a traveling-wave Pockels cell geometry. Section II.C. considers the electrical and optical characteristics of the traveling-wave geometry. A simple theory for predicting the temporal resolution is derived and applied to several modulators. The theory indicates that a resolution of a few hundred femtoseconds is achievable. The chapter concludes with an introduction to the various sources of noise and considers how they affect the overall sensitivity of the electro-optic technique.

Technique	Temporal Res. (Bandwidth)	Sensitivity	Maximum Voltage	Comments
Conventional Oscilloscope	1 ns (350 MHz)	10 μ V	10 V	Readily available
Trav. Wave Oscilloscope	100-300 ps (1-3 GHz)	1-10 V	100 V	Insensitive
Sampling Oscilloscope	100 ps (3 GHz)	1 mV	10 V	Jitter
Supercond. Sampling	10 ps (30 GHz)	10 μ V	100mV	Cryogenic
Ind. Optical Sampling	3 ps (100 GHz)	10 μ V	>1 kV	Need ps laser; No Jitter Material limit
Electro-optic Sampling	500 fs (\sim 1 THz)	<50 μ V	>1 kV	Need sub-ps laser No Jitter; Optical Limit

TABLE I-1 Comparison of high speed measurement techniques

Chapter III considers the experimental system and also presents a variety of results. The construction of the key elements is detailed together with a description of the laser and the overall system configuration. Calibration procedures for both time and sensitivity are presented, followed by an outline of the measurement procedure. Section III.C. contains results demonstrating the temporal resolution and sensitivity as well as the effects of dispersion for several modulators. A few demonstrative applications of picosecond electronics are also included. The chapter concludes with an experimental investigation of noise sources and an evaluation of the effectiveness of signal to noise enhancement techniques.

Chapter IV is a summary of the results and conclusions of the thesis work.

Appendix A discusses the method of auto-correlation by which the laser pulsewidth is determined. Appendix B elaborates on the electrical signal generated by a photoconductive detector.

CHAPTER II

THEORY OF ELECTRO-OPTIC SAMPLING

In this chapter we present the theoretical basis for choosing the electro-optic effect as the mechanism for sampling picosecond electrical transients. A brief introduction will serve to delineate the differences between the technique we have developed and previous ones. The second section describes the origin and implementation of the electro-optic effect in birefringent media. Several materials and types of modulators are considered. This discussion is followed by an analysis of the operation of the traveling-wave modulator geometry. The modulator's electrical and optical properties are established and a theoretical model is derived to predict its ultimate temporal resolution. We also discuss the major sources of noise, their effect on system sensitivity, and how the application of signal recovery techniques enhances the overall signal to noise ratio. Finally, we present an illustrative discussion of the transient measurement process.

II.A. Introduction to direct electro-optic sampling

To date, the use of optical pulses in the characterization of picosecond electrical signals has been of an indirect nature. Although the jitter-free property of the

optical pulse train has been exploited, the sampling gate itself has always been an electronic material property (photoconductivity) induced by the optical pulse. The goal of this work is to utilize picosecond and sub-picosecond optical pulses directly as the sampling elements. This approach implies that the optical pulse itself is the carrier of information about the amplitude of the electrical signal obtained at the instant of sampling.

We have chosen the linear electro-optic effect (Pockels effect) as the means of impressing electrical information onto the optical pulse. The Pockels effect alters the state of polarization of the optical beam in such a way that, viewed through a linear polarizer, the intensity of the transmitted beam changes linearly with the amplitude of the electrical signal. As will be seen, the electro-optic effect does not limit the speed of response. Temporal resolution is determined entirely by optical pulse properties and simple geometrical considerations. The electro-optic crystal is essentially passive and presents itself only as an interaction medium for the optical and electrical signals. For this reason, there is no jitter introduced between the optical and electrical signals during the sampling process. The absence of jitter allows the optical pulsewidth to be the final criterion of temporal resolution.

Figure II-1 depicts the conceptual elements in a direct

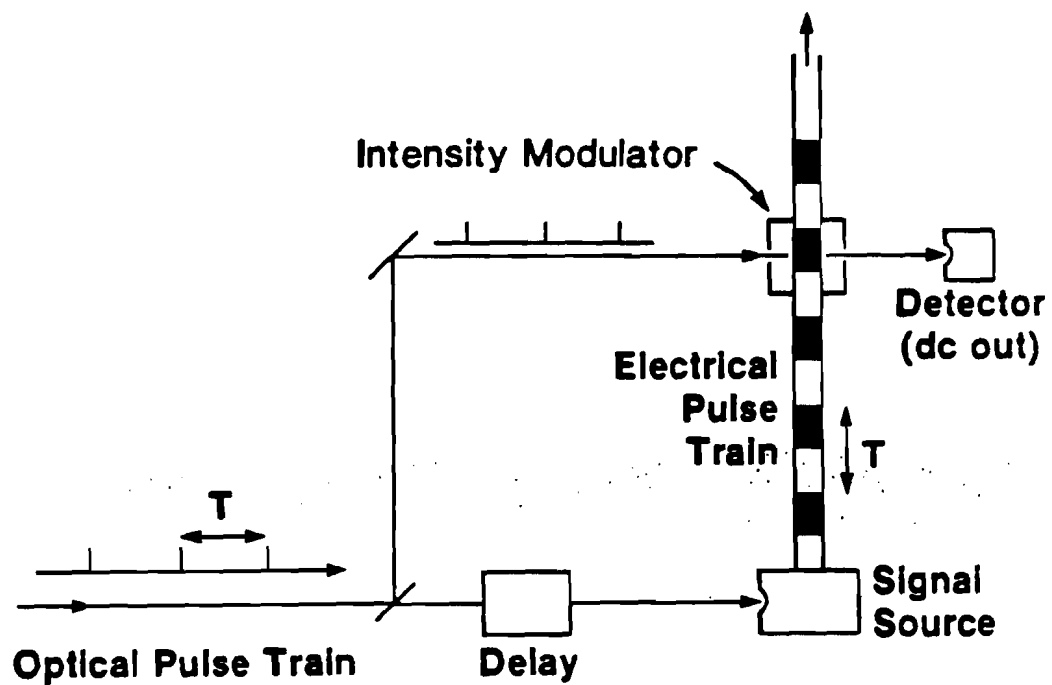


Figure II-1 Direct optical sampling

optical sampling system. A high repetition rate (1-100 MHz) train of short optical pulses is split, with one of the resultant beams triggering the electrical signal source while the other beam goes to the electro-optic modulator. The signal source generates a jitter free train of electrical pulses to be measured at the same rate as its incident optical pulse train. These two trains meet in perfect synchronism at the modulator. Because of this synchronization, each optical pulse interacts with precisely the same corresponding point of each electrical pulse as it passes through the electro-optic medium. In this way, the intensity of each optical pulse is altered by the exact same amount, in proportion with the amplitude of the electrical signal seen at that point in time. Thus, a slow detector measuring the average intensity of the output beam will yield a DC signal proportional to the amplitude of the sampled electrical signal. By slowly sweeping the optical delay, the detector signal will follow the amplitude of the unknown electrical signal.

Direct optical sampling has been employed before. In two cases, Auston²¹ and LeFur²² used the technique on a single shot basis to observe kilovolt electrical transients in a Pockels cell with a resolution of approximately 25 ps. More recently, a high repetition rate system was employed by Alferness et al.²³ to characterize the speed of electro-optic waveguide modulators with an effective tempo-

ral resolution of approximately 60 ps.

This work investigates the limits of a direct electro-optic sampling system as a measurement tool for the characterization of unknown electrical transients. Optical and electrical considerations of the Pockels cell are discussed in detail as well as the effects of electronic signal processing. We will demonstrate that sub-picosecond temporal resolution and voltage sensitivities of less than one hundred microvolts are possible.

II.B. The electro-optic effect

In this section we treat various aspects of the electro-optic effect and its application. We first present a discussion of the origin of the electro-optic mechanism and the particular properties which apply in our situation. This discussion is followed by a description of how the electro-optic effect is implemented in an intensity modulator, addressing the questions of linearity and sensitivity. The next section compares some commonly used electro-optic materials and reaches the conclusion that lithium tantalate is the optimal medium in this application. Finally we discuss the bandwidth aspects of various types of high speed lithium tantalate modulators in current use.

II.B.1. The electro-optic mechanism

The electro-optic, or Pockels, effect is a change in the optical dielectric properties of a medium (usually a crystal) in response to an applied electric field. The effect is commonly realized as a change in the index of refraction. In order to more completely understand the limits of this mechanism we must investigate the behaviour of the electronic charges within the medium.

The application of an external electric field to a medium displaces both the ions in the lattice and the electron orbits from their unperturbed positions and orientations. The displacements create electric dipoles whose macroscopic manifestation is the electric polarization, P . In any particular material, P is a function of the applied electric field E . The polarization can be represented by the following power series:²⁴

$$\bar{P}_i(\omega_p) = \chi_{ij}^{(1)} \bar{E}_j(\omega_p) + \chi_{ijk}^{(2)} \bar{E}_j(\omega_m) \bar{E}_k(\omega_n) + \dots \quad \text{II-1}$$

where $\chi^{(1)}$ and $\chi^{(2)}$ are tensors that relate the vectors P and E . i, j , and k are the cartesian indices that run from 1 to 3 and l, m , and n represent different frequency components. Each term is summed over all repeated indices according to the Einstein sum convention. We include only those terms that are of interest here. χ is a tensor, because in many materials, especially crystals, E and its

induced P are not necessarily colinear.

The $\chi_{(1)}$ term is dominant and is an extremely good approximation for P with small applied electric fields. It is this term that applies to all linear optics and yields the common index of refraction, n , and optical dielectric constant, ϵ , as follows:

$$n = \sqrt{\epsilon} = (1 + 4\pi\chi^{(1)})^{1/2}. \quad \text{II-2}$$

The $\chi_{(2)}$ term (containing 27 elements) gives rise to optical mixing, second harmonic generation and the Pockels effect. It exists only for crystals lacking an inversion symmetry. Otherwise, all components of the tensor vanish. In the general case, P can be written:

$$\bar{P}_i \begin{pmatrix} \omega_m + \omega_n \\ \omega_m - \omega_n \end{pmatrix} = \chi_{ijk}^{(2)} \bar{E}_j(\omega_m) \bar{E}_k(\omega_n) \quad \text{II-3}$$

which relates fields of three different frequencies. This equation describes the phenomenon of optical three-wave mixing. If $\omega_m = \omega_n$ then P has a frequency of $2\omega_n$ and second harmonic generation arises. If one of the fields is at DC, then $\chi_{(2)}$ gives rise to the Pockels effect, where the input and output frequencies are the same, and the effective $\chi_{(2)}$ becomes a function of the DC field, i.e.

$$\bar{P}_i(\omega_2) = \left(\chi_{ijk}^{(2)} E_k(\text{DC}) \right) \bar{E}_j(\omega_2). \quad \text{II-4}$$

Thus, similarly to the $\chi_{(1)}$ term, $\chi_{(2)}$ produces an index of refraction change that depends on the magnitude of the applied field. E_k does not necessarily have to be at DC, but can actually be extended well into the radio frequency (RF) regime without appreciably changing the frequency of the output field. As long as the input and output frequencies are essentially equal, the change of index is still considered to be the Pockels effect.

In most electro-optic materials, the linear dielectric constant is a strong function of frequency.²⁵ Figure II-2 depicts the general behaviour of ϵ and displays several resonances where ϵ changes markedly. There are usually several acoustic resonances that depend upon physical parameters of the crystal such as size and mounting configuration. High frequency behaviour is caused by lattice resonance near 10 THz and electronic resonance in the ultra-violet regime near 1000 THz. Between resonances, dielectric dispersion is negligible.

It is not surprising that the non-linear coefficients, χ , exhibit similar resonance behaviour. A modulating field E at frequency ω_m , below the lattice resonance, induces two independent components of change in the susceptibility $\chi(\omega_o)$. These contributions sum to yield a total change of $d\chi(\omega_o)/dE(\omega_m)$. In the optical regime, this perturbation is due solely to the deformation of the electron potential

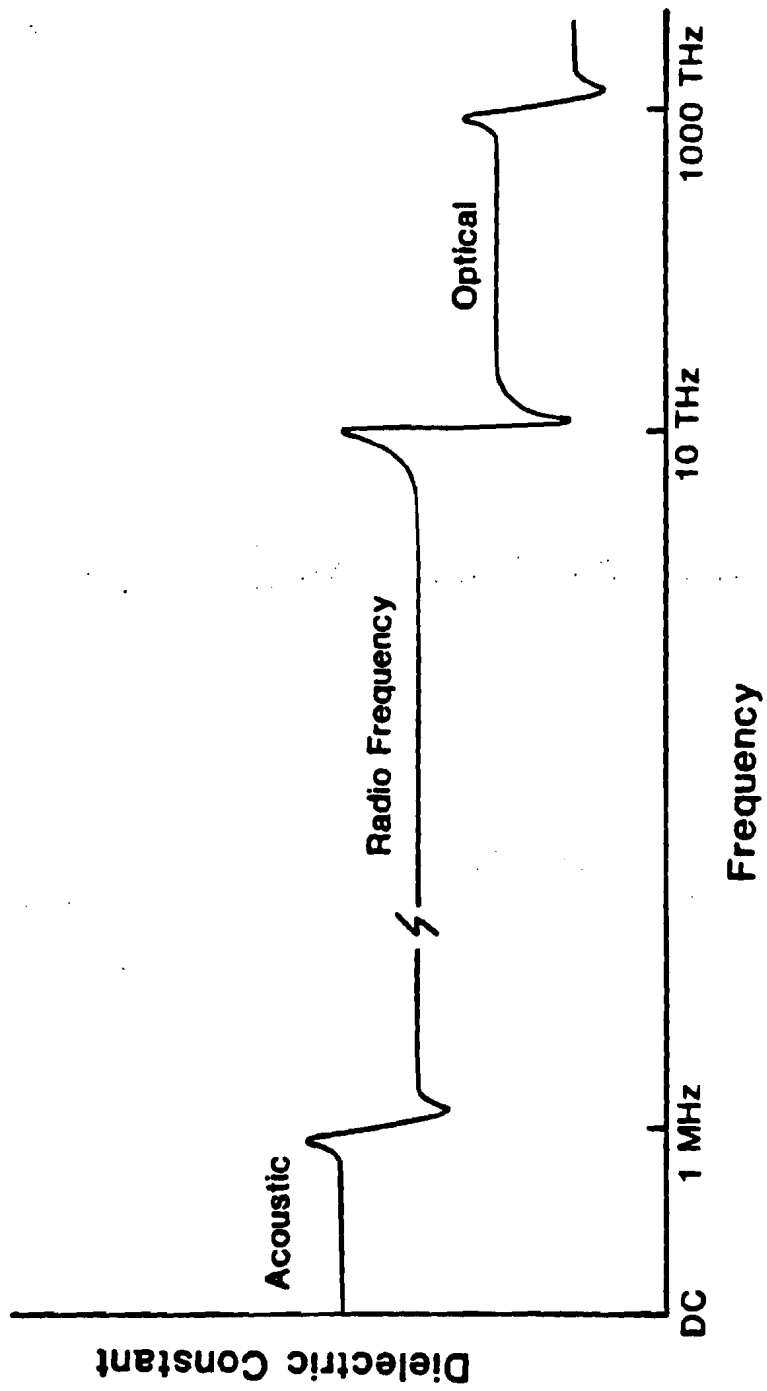


Figure II-2 General behaviour of the dielectric constant versus frequency

function by the direct action of the electric field. In the RF regime, an additional contribution arises from a deformation of the potential due to a change in the lattice spacing. Therefore we can represent the effect by:

$$\frac{d\chi^{(2)}(\omega_b)}{dE(\omega_m)} = \left. \frac{\partial \chi^{(2)}(\omega_b)}{\partial E(\omega_m)} \right|_{\text{electronic}} + \left. \frac{\partial \chi^{(2)}(\omega_b)}{\partial E(\omega_m)} \right|_{\text{lattice}}. \quad \text{II-5}$$

The electronic contribution is typically only about 10% of the lattice effect. Below acoustic resonances the Pockels effect accrues two more contributions from the elasto-optic and piezo-optic effects. These are experienced only if the crystal is "free" (constant stress) and therefore can be avoided by either physically clamping the crystal or simply operating at a frequency above the acoustical region.

Thus, we see that the mechanism responsible for the electro-optic effect is extremely fast, extending up to 1000 THz. The limiting physical phenomenon, however, is the anomalous behaviour of $\chi^{(2)}$ near the lattice resonance at approximately 10 THz. This behaviour indicates that the electro-optic mechanism would impose a limit to temporal response only when electrical signal characteristics were in the regime of tens of femtoseconds. Such a bandwidth is more than ample for our present aspirations.

The electro-optic effect can also be represented as a change in the relative optical impermeability B_{ij} , propor-

tional to the applied electric field E_k . By definition:

$$B_{ij} = \left(\frac{1}{\epsilon} \right)_{ij} - \left(\frac{1}{n^2} \right)_{ij} \quad \text{II-6}$$

It is through this quantity that the susceptibility, $\chi^{(2)}$, is related to the commonly tabulated electro-optic coefficient r_{ijk} .²⁶ The resultant tensor relationship is given by:

$$\Delta B_{ij} = r_{ijk} E_k \quad \text{II-7}$$

In this form, r_{ijk} has 27 components that correspond to the 27 components of the susceptibility tensor $\chi^{(2)}_{ijk}$. From permutation relations it can be shown²⁵ that (ijk) is equivalent to (jik) and hence a reduced form of the electro-optic tensor, r_{pk} , can be employed. This tensor contains 18 elements of which many are usually equal or identically zero owing to crystal symmetry properties. p refers to the contracted notation for (ij) , ie. $1=(11)$, $2=(22)$, $3=(33)$, $4=(23)$, $5=(13)$, $6=(12)$. This results in a simplified form of equation II-7:

$$\Delta B_p = r_{pk} E_k \quad \text{II-8}$$

which can be transformed to relate the change in index of refraction to the applied electric field.

$$\Delta B_p = r_{pk} E_k = \Delta \left(\frac{1}{n_p^2} \right) = - \frac{2 \Delta n_p}{n_p^3} \quad \text{II-9}$$

for $\Delta n_p \ll n_p$ as is usually the case. Thus we obtain the

common electro-optic relation:

$$\Delta n_p = -\frac{1}{2} n_p^3 r_{pk} E_k \quad \text{II-10}$$

Two values of r_{pk} are commonly specified. If the crystal is at constant stress, or "free", then the electro-optic coefficient is denoted with a superscript T, e.g. r_{pk}^T . The "free" condition is exemplified at low frequencies, below acoustic resonances, where the elasto-optic and piezo-optic effects can contribute. If r_{pk} is determined at constant strain, or "clamped", the electro-optic coefficient is written with a superscript S. r_{pk}^S is the value of the electro-optic coefficient obtained in the RF regime, ie. between the acoustic and lattice resonances.

In order to understand how the tensor index change, Δn_p , alters the birefringent characteristics of the medium, we must introduce the index indicatrix or index ellipsoid. The indicatrix, a mathematical construct, is used to depict the anisotropic index properties of birefringent crystals of which electro-optic media are a subset. In these crystals, for any particular direction, only two linearly and orthogonally polarized waves will propagate. They will usually experience different indices and hence travel at different velocities. In general, the index indicatrix is a triaxial ellipsoid. Any central plane cross-section is an ellipse. The lengths of any pair of orthogonal axes within that

ellipse are proportional to the indices experienced by waves polarized along those same axes and traveling normal to the plane of the ellipse.

The general form of the index ellipsoid in an arbitrary cartesian coordinate system is:

$$\frac{X^2}{N_1^2} + \frac{Y^2}{N_2^2} + \frac{Z^2}{N_3^2} + \frac{2YZ}{N_4^2} + \frac{2XZ}{N_5^2} + \frac{2XY}{N_6^2} = 1 \quad \text{II-11}$$

where the subscripts 1-6 again are the reduced form of the cartesian coordinates, 1=xx, 2=yy, 3=zz, 4=yz, 5=xz, 6=xy. By reorienting the axes, equation II-11 can take a simpler form:

$$\frac{X^2}{n_1^2} + \frac{Y^2}{n_2^2} + \frac{Z^2}{n_3^2} = 1 \quad \text{II-12}$$

In this case, the major and minor axes of the ellipsoid are oriented along the cartesian axes. These are called the principal axes of the crystal and have corresponding principal indices n_1 , n_2 , n_3 .

Many common electro-optic crystals are uniaxial. This implies that for one particular direction within the medium, the indices for both polarizations are equal. Thus, the plane cross-section of the index ellipsoid normal to this direction is a circle. This direction is usually referred to as the optic axis or c-axis, and in a cartesian coordi-

nate system is oriented along the z-axis. Figure II-3 illustrates the index ellipsoid and its principal cross-sections for a uniaxial crystal in its principal axis coordinate system. The indicatrix equation in the principal axis system becomes:

$$\frac{x^2}{n_o^2} + \frac{y^2}{n_o^2} + \frac{z^2}{n_e^2} = 1 . \quad \text{II-13}$$

Light traveling in the x-y plane is resolved into two orthogonal polarizations along the principal axes of the crystal. The polarization component perpendicular to the optic axis is referred to as the ordinary ray and experiences the ordinary index, n_o . The other wave experiences the extraordinary index, n_e , and hence is called extraordinary. If light were to propagate along the z-axis, it would see no birefringence, because in this direction $n_e = n_o$.

Any electro-optic crystal in its unperturbed state can be represented by equation II-11. The application of an electric field can distort the indicatrix by changing not only its symmetry, but also its overall size and orientation due to the tensor nature of the electro-optic coefficient.

The previously derived equation II-10 describes the change of the indices N_1 - N_6 with respect to the applied field. The equation can be rewritten in a more convenient form applicable to use with the indicatrix equation

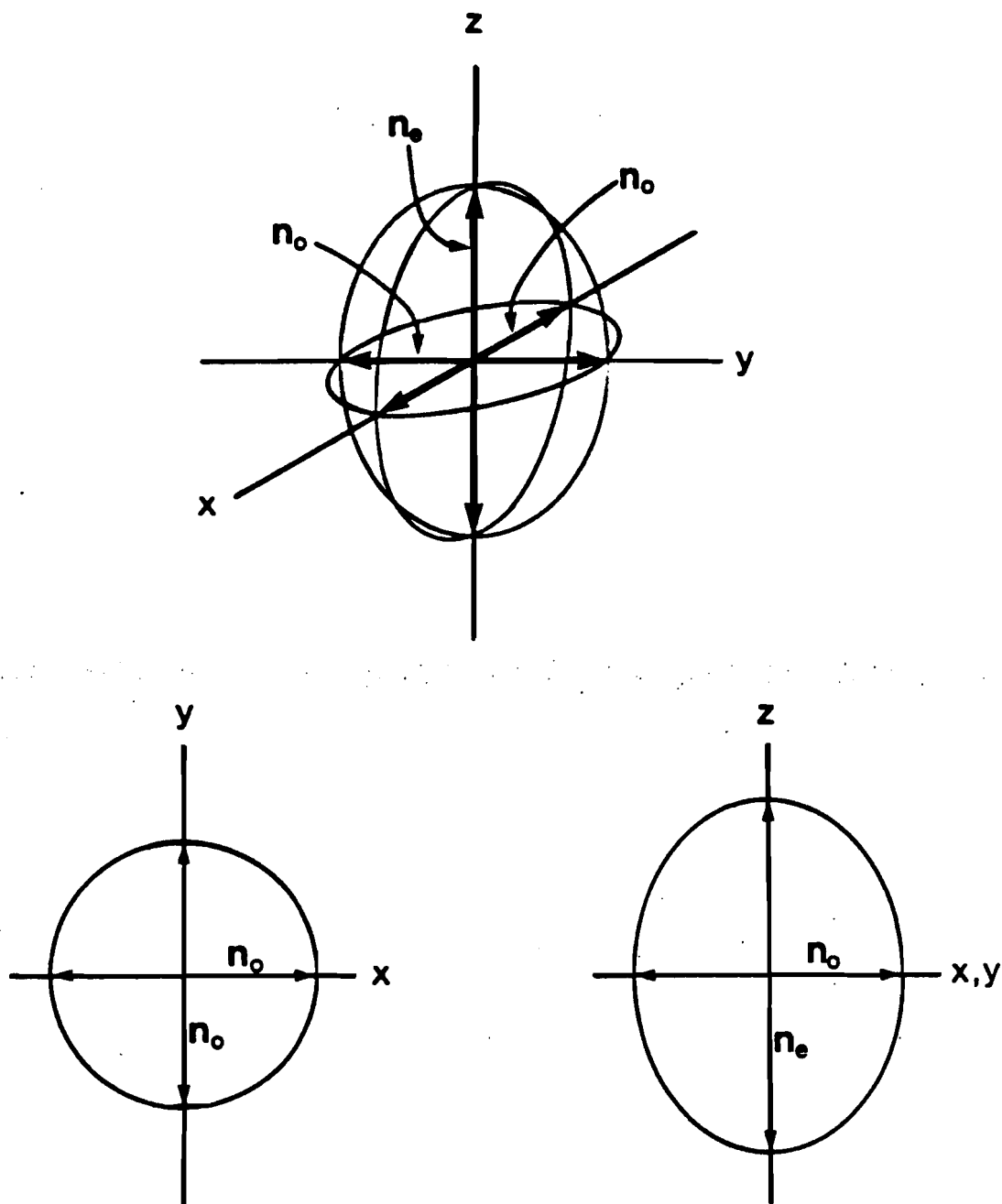


Figure II-3 Index ellipsoid for a uniaxial crystal
(In the principal axis coordinate system)

as follows:

$$\Delta\left(\frac{1}{n_p^2}\right) = r_{pk} E_k \quad \text{II-14}$$

where as before $p=1,2,\dots,6$ and $k=1,2,3$. We now have the equations necessary to understand how electro-optic materials can be applied as intensity modulators.

II.B.2. Intensity modulation

Coherent light that impinges on an electro-optic crystal is resolved into two orthogonal components, each experiencing, in general, a different index. After propagating through a length l , of the medium, a phase difference of δ between the waves is accrued according to the equation:

$$\delta = \frac{2\pi}{\lambda} l \Delta n \quad \text{II-15}$$

where λ is the free space wavelength and Δn is the birefringence. Thus the state of polarization of the emergent beam is altered from the input unless δ is an integer multiple of 2π . This change in polarization can be converted to an intensity change by placing the crystal between crossed linear polarizers. By orienting the input polarization to the crystal at 45 degrees to its principal axes, the most efficient change of intensity for a given δ is attained. The resultant intensity modulation function is periodic in δ with period π :

$$I = I_0 \sin^2\left(\frac{\delta}{2}\right) \quad \text{II-16}$$

where I and I_0 are the output and input intensities. T is the transmission defined by $T=I/I_0$. See Figure II-4. Thus by the application of an external electric field we can modulate the birefringence and hence δ , thereby achieving intensity modulation.

As can be seen, the intensity modulator is best operated at its 50% transmission point. In this regime the slope of the modulation function (equivalent to sensitivity) is at its maximum value and the response is also linear for small values of induced retardance relative to π . In order to operate the modulator at this point, the static birefringence (ie. with no applied field) between polarizers, δ_s , should be an odd multiple of $\pi/2$ radians. A retardance of $\pi/2$ radians is the same as a retardance of one quarter wavelength and hence 50% transmission is referred to as the quarter wave point. For 1% maximum linearity error, the total retardance including that from the applied field must be less than 0.08π radians. 5% error occurs at a retardance of 0.18π radians.

The net retardance between polarizers can have several components. The electro-optic crystal itself has a static birefringence giving rise to a retardance, δ_x . If δ_x does not place the modulator at its quarter wave point, then an

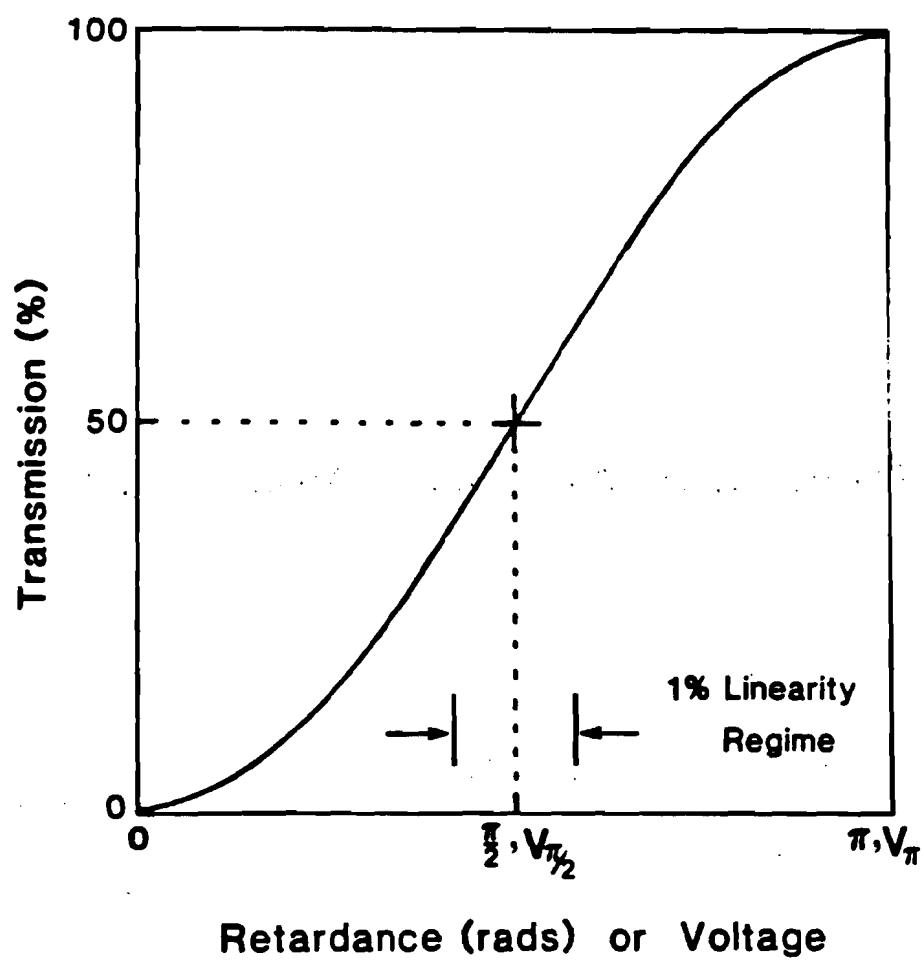


Figure II-4 Intensity modulator transmission function

additional static compensating retardance, δ_c must be introduced (usually another crystal). The total phase retardance, δ_T , which also includes the field induced component, δ_F , can therefore be represented as:

$$\delta_T = \delta_S + \delta_F \quad \text{where} \quad \delta_S = \delta_X + \delta_C \quad . \quad \text{II-17}$$

The static components are given by:

$$\delta_X = \frac{2\pi}{\lambda} l \Delta n \quad \text{II-18}$$

and

$$\delta_C = \left(2\pi S + \frac{\pi}{2}\right) - \delta_S \quad (S \text{ is an integer}) \quad . \quad \text{II-19}$$

We now consider, in general terms, how δ_F is related to an applied voltage V . Figure II-5 shows the general case of a crystal in a transverse geometry, having length L , and electrode spacing (thickness), d . The applied electric field is given by:

$$E = \frac{V}{d} \quad \text{II-20}$$

where V is the voltage between the electrodes. Once we know the material and the configuration it will be used in, we can linearly relate δ_F to V by using equations II-10, II-15 and II-20 to yield:

$$\delta_F = -\frac{\pi}{\lambda} n^3 r \frac{L}{d} V \quad . \quad \text{II-21}$$

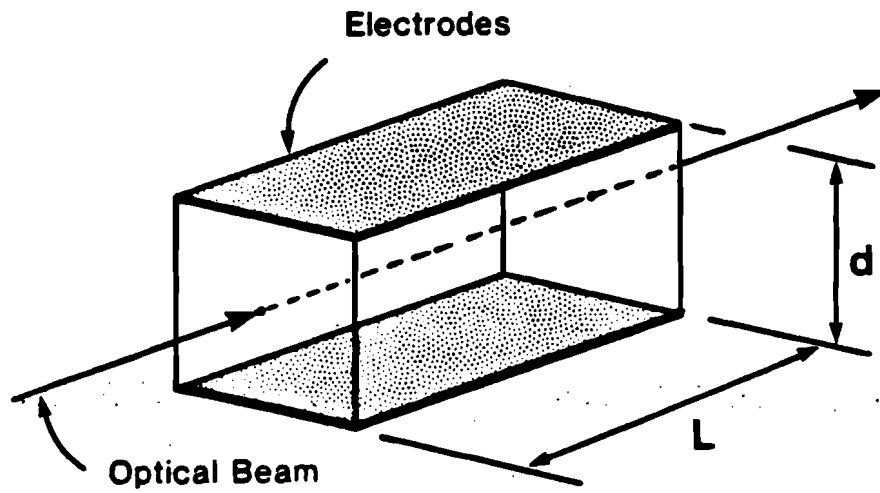


Figure II-5 Transverse electro-optic modulator geometry

Because of this linear relationship, we can label the horizontal axis in Figure II-4 by either ϕ_F or V .

The sensitivity of a particular intensity modulator to an applied voltage can be specified in two related ways. One can specify either the modulator's halfwave voltage, V_π , or the slope of the transmission function at the quarter wave point. The halfwave voltage is the voltage necessary, in a specific geometry, to induce a $\phi_F = \pi$ and hence achieve 100% intensity modulation. We can also define a non-geometry specific halfwave voltage V_π^* by:

$$V_\pi^* = V_\pi \frac{L}{d} \quad \text{II-22}$$

which is the halfwave voltage necessary for a crystal with $L=d$.

Given the halfwave voltage, one can calculate the birefringence induced by a voltage, ΔV , from the following relation:

$$\phi_F = \pi \frac{\Delta V}{V_\pi} \quad \text{II-23}$$

The subsequent intensity modulation can then be determined by using equation II-16:

$$I = I_0 \sin^2 \left(\frac{\phi_F}{2} \right) \quad \text{II-24}$$

The more direct method by which to specify the sensitivity is to merely determine the slope of the transmission

function, $\Delta T/\Delta V$. The slope is easily experimentally determined, and immediately relates an applied voltage to a change in transmission. By evaluating the derivative of the transmission function at the quarter wave point, we can relate the slope to the halfwave voltage by:

$$\frac{\Delta T}{\Delta V} = \frac{\pi/2}{V_{\pi}} . \quad \text{II-25}$$

Thus, merely by measuring ΔT and knowing either the slope of the transmission function or the modulator's halfwave voltage, one has enough information to determine the amplitude of an unknown applied voltage. For this measurement, equation II-25 is usually rewritten as:

$$\Delta V = \frac{\Delta T}{1.57} V_{\pi} . \quad \text{II-26}$$

We must also consider the effect of incomplete extinction for the crossed polarizers as is often the experimental case. Incomplete extinction leads to an effective reduction in sensitivity for the intensity modulator, because the slope of the transmission function decreases. Polarizers are characterized by their extinction ratio, X . X is the ratio of the transmitted light intensity for a pair of parallel polarizers over that for crossed polarizers. Typical values range from 100 to over 1000. Figure II-6 depicts the slope of the transmission function versus X . It is seen that even a terribly poor X of only 10 still yields

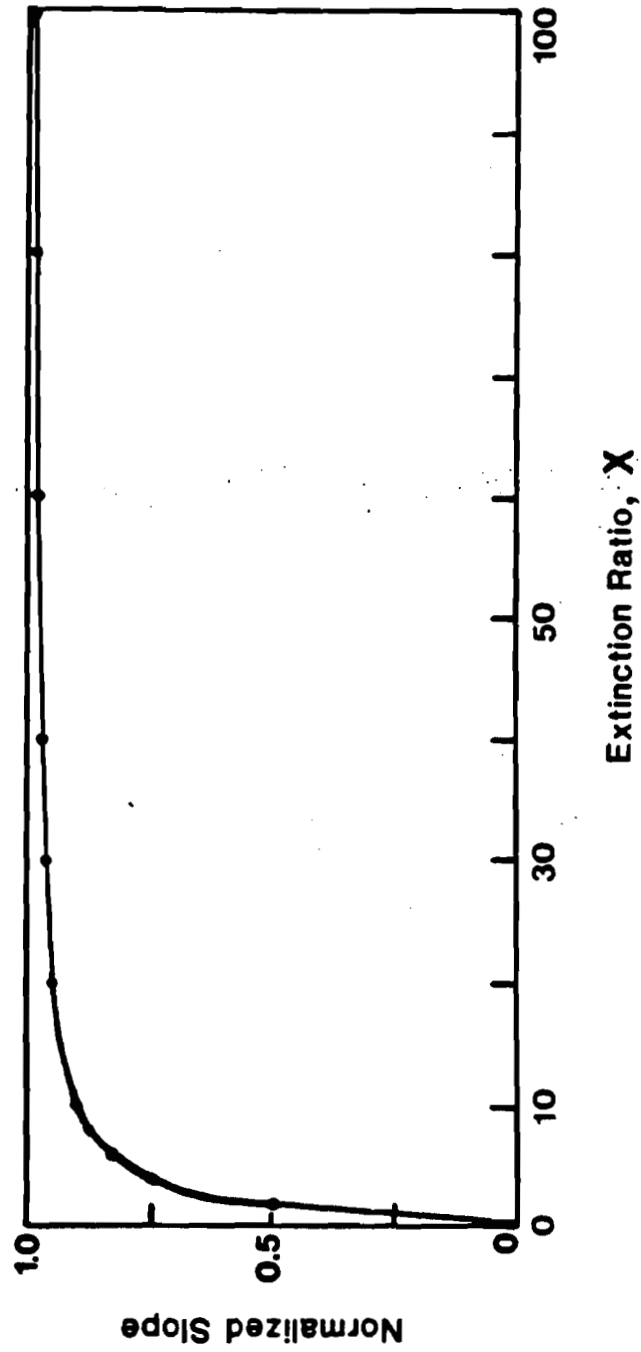


Figure II-6 Transmission function slope versus
polarizer extinction ratio

90% of the optimum slope. Thus we find that the X is not a critical parameter for intensity modulation in this geometry.

II.B.3. Electro-optic material properties

There are literally hundreds of crystals that exhibit an electro-optic effect. The three most common types of crystal used in modulators today are: 1) potassium dihydrogen phosphate (KDP) and its isomorphs, 2) lithium niobate and 3) lithium tantalate. All of these crystals are uniaxial.^{27,28} KDP and its isomorphs are the most widely used. They are readily obtained and exhibit excellent optical qualities of transparency, freedom from strains and high resistance to optical damage. However, KDP type crystals are grown from a water solution and hence are soft, require special handling and must be environmentally isolated to prevent surface degradation. Even though ADP and deuterated KDP have good electro-optic coefficients, the handling problems make their experimental use difficult.

Both lithium niobate and lithium tantalate have rhombohedral crystal structure and are in the point group $3m$, which identifies the structure of the electro-optic tensor. The crystals are grown at high temperatures and, once poled, can be readily fabricated using conventional techniques. Environmentally stable, they can also be readily cleaned using common solvents. Both crystals exhibit super-

rior electro-optic coefficients relative to other materials, typically requiring a halfwave voltage four times less than ADP. An advantage of lithium tantalate is that it has a static birefringence 18 times less than that of its niobate counterpart. This small birefringence relaxes fabrication tolerances, enables a larger entrance cone angle when focussing through the crystal, and also reduces multiple order retardance effects for large bandwidth optical pulses. Figure II-7 shows the optical dispersion curves that also exhibit a relatively constant birefringence. Tantalate is also much less susceptible to optical damage when exposed to intense laser beams than is niobate. A minor disadvantage that can be experimentally eliminated is that the birefringence is quite temperature sensitive, having a magnitude of 5×10^{-5} per degree celsius. Overall, the choice of lithium tantalate for our purposes is evident.

We will now consider the specifics of lithium tantalate as it is employed in most modulator configurations, including ours. The electro-optic tensor, r_{pk} , and its component values are shown in Figure II-8.

The largest electro-optic effect in lithium tantalate is realized when the electric field is applied along the z-axis and light is propagated in the x-y plane normal to the electric field. This arrangement is known as the transverse geometry and is shown in Figure II-9.

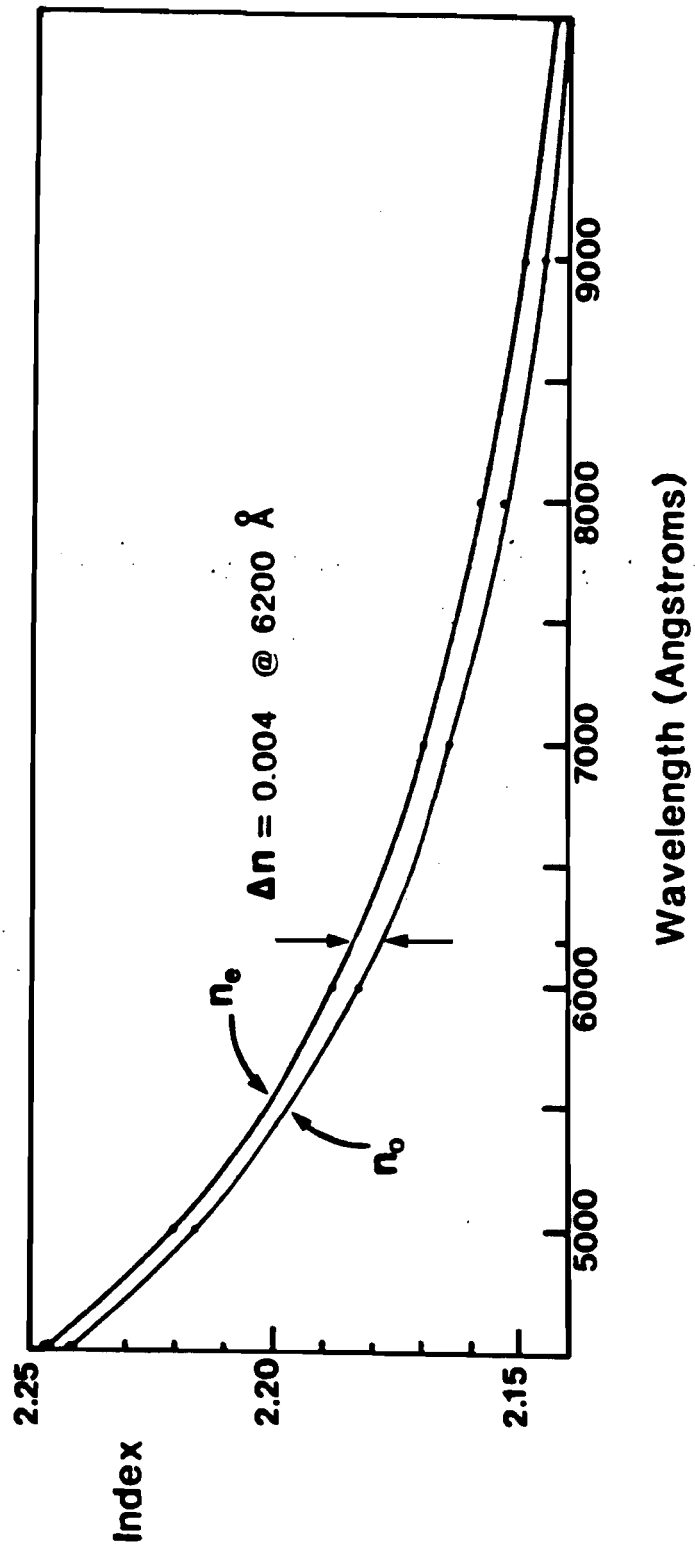


Figure II-7 Dispersion of the optical indices for lithium tantalate

$$r_{pk} = \begin{Bmatrix} 0 & -r_{22} & r_{13} \\ 0 & r_{22} & r_{13} \\ 0 & 0 & r_{33} \\ 0 & r_{51} & 0 \\ r_{51} & 0 & 0 \\ -r_{22} & 0 & 0 \end{Bmatrix}$$

$$\begin{aligned} r_{12} &= -r_{22} = r_{61} \\ r_{13} &= r_{23} \\ r_{42} &= r_{51} \end{aligned}$$

$$\left. \begin{aligned} r_{33} &= 30.3 \times 10^{-12} \text{ m/V} \\ r_{13} &= 7.0 \times 10^{-12} \\ r_{51} &= 20.0 \times 10^{-12} \\ r_{22} &\approx 1.0 \times 10^{-12} \end{aligned} \right\} @ 6328 \text{ \AA}$$

Figure II-8 Lithium tantalate electro-optic tensor

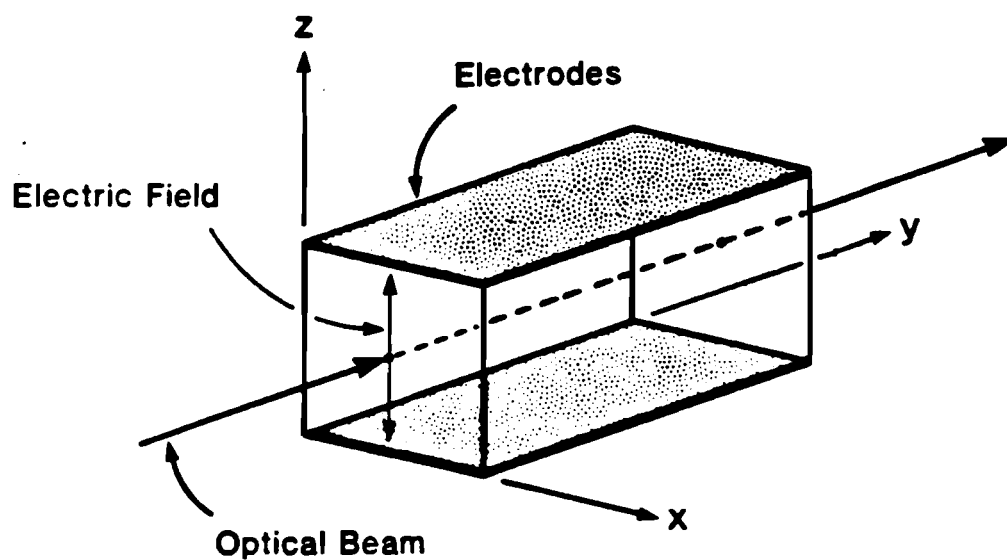


Figure II-9 Transverse modulator geometry

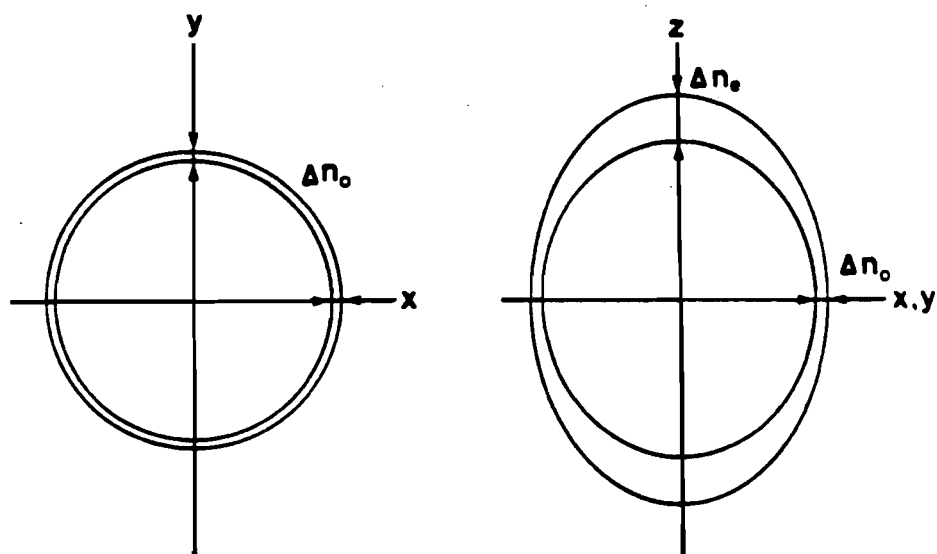


Figure II-10

Indicatrix distortion due to an applied electric field

Applying equation II-14 to the principal axis form of the index indicatrix for this electric field direction we get:

$$\left(\frac{1}{n_o^2} + r_{12} E_z\right)(x^2 + y^2) + \left(\frac{1}{n_e^2} + r_{33} E_z\right)z^2 = 1 \quad \text{II-27}$$

where:

$$\Delta\left(\frac{1}{n_o^2}\right) = r_{12} E_z \quad \text{and} \quad \Delta\left(\frac{1}{n_e^2}\right) = r_{33} E_z . \quad \text{II-28}$$

The direct index changes are:

$$\Delta n_o = -\frac{1}{2} n_o r_{12} E_z$$

and

$$(E_z = E_3) \quad \text{II-29}$$

$$\Delta n_e = -\frac{1}{2} n_e r_{33} E_z .$$

The change of the indicatrix is depicted in Figure II-10. For a positive E_z , both principal indices decrease, and no cross terms are introduced. Only the size and symmetry of the ellipsoid change. No rotation is induced, and it is still rotationally symmetric about the optic axis. It turns out that this is an important property for velocity matching considerations. The field induced retardance can now be written as:

$$\delta_F = \frac{2\pi}{\lambda} (\Delta n_e - \Delta n_o) L = \frac{\pi}{\lambda} (n_e^3 r_{33} - n_o^3 r_{12}) V \frac{L}{d} . \quad \text{II-30}$$

Using the equation for δ_r and equation II-22, we can calculate V_π^* for the crystal as follows:

$$V_\pi^* = \frac{\lambda}{(n_e^3 r_{33} - n_o^3 r_{13})} \quad , \quad \text{II-31}$$

which yields a $V_\pi^* = 2580$ V for lithium tantalate.

The static birefringence introduces two effects that can affect proper operation of the intensity modulator. The temperature dependance of the birefringence necessitates that for an intensity modulator to remain linear to within $\pm 0.05\%$ the temperature of a 1 mm long crystal must be maintained within 1 degree Celsius. The use of short sampling pulses, that have a large optical bandwidth poses the second problem. In this case all wavelengths will not experience the same amount of retardance and hence will be of different polarizations. If the wavelengths all fall within a 0.5 radian range then this is of minimal consequence, since they are all still on the linear portion of the transmission function (equation II-16). If the retardance is too great, the wavelengths can emerge in different retardance orders and render the modulator ineffective.

Both birefringent effects can be compensated for by introducing a second crystal of precisely the same thickness as the first, but oriented so that its principal axes are interchanged so as to "unwind" the accumulated static retardance. Thus, as long as both crystals are held close to the

same temperature, static birefringent effects are virtually eliminated and all wavelengths appear in the zero order.

II.B.4. Lithium tantalate modulators

An ideal intensity modulator⁷⁶ would impress an electrical signal onto an optical beam with a one-to-one correspondence between temporal points. Such a device would have infinite bandwidth and infinitely narrow temporal resolution. Experimentally, two effects usually prevent this desirable situation from being realized. The first arises because the modulating device simply distorts the proper electrical signal. The second effect, as discussed in the introductory review, arises from having more than one point in the electrical signal influence a single optical point. The converse is also true, ie. several optical points receive contributions from a single electrical point. Thus, the information is smeared out in time (and usually space). Just how long this smearing occurs within the modulator is precisely the temporal resolution, τ , with which the optical beam duplicates the electrical signal.

In order to evaluate the performance of several existing modulators, we will compare the most common specification, bandwidth, denoted by B . As defined in the introduction, the bandwidth usually represents the maximum frequency that can be effectively impressed on the optical carrier. It is directly related to the temporal resolution,

τ , by:

$$B = \frac{0.35}{\tau} \quad . \quad \text{II-32}$$

For our purposes, a bandwidth specification translates to the temporal resolution with which sampling can be done in that particular geometry.

The simplest geometry for a lithium tantalate transverse modulator is a slab of crystal having dimensions L and d between electrodes as depicted in Figure II-9. In this geometry we encounter the distortion effect, because the electrical response is limited by the RC time constant of the cell, which appears as a capacitor. For this reason it operates as a lumped circuit element and risetimes are usually limited to the nanosecond regime. Good examples of such modulators are given in Biazzo²⁹ and Denton et al.²⁸ In order to circumvent circuit difficulties, Kaminow et al.³⁰ have placed crystals in microwave cavities and attained bandwidths of 4 GHz corresponding to a τ of less than 100 ps. 100 ps is approximately equal to the transit time for the optical beam to pass through the crystal. The optical transit time is entirely analagous to the transit time for an oscilloscope as discussed in section I.B.2.

To further enhance response bandwidth and hence temporal resolution, traveling-wave geometries must be employed. This arrangement allows the electrical signal to propagate

as a traveling-wave along stripline electrodes, thus avoiding the lumped circuit parameters that were the previous limit. If the optical signal also travels in the same direction, then one could expect a reduced effective transit time and hence larger bandwidth. The geometry is pictured in Figure II-11a. White and Chin³¹ and Peters³² both employed this scheme and demonstrated bandwidths up to 2.9 GHz.

The colinear propagation case is limited by the mismatch of electrical and optical velocities, V_e and V_o , respectively, given by:

$$V_e = \frac{c}{\sqrt{\epsilon_{eff}}} \quad \text{and} \quad V_o = \frac{c}{n} \quad \text{II-33}$$

where c is the speed of light in vacuum, n is the optical index = 2.18, and ϵ_{eff} is the effective dielectric constant. ϵ_{eff} depends on the geometry and frequency employed. By using the velocity compensating geometry shown in Figure II-11b, where some of the electric field is excluded from the crystal, Rigrod and Kaminow³³ were able to lower ϵ_{eff} and hence raise the electrical velocity to enable a better velocity match leading to a bandwidth of over 9 GHz.

A more effective way of matching velocities, however, is to decrease the effective optical velocity in the direction of V_e . The general arrangement is depicted in Figure II-12 and allows for the propagation of the electrical and

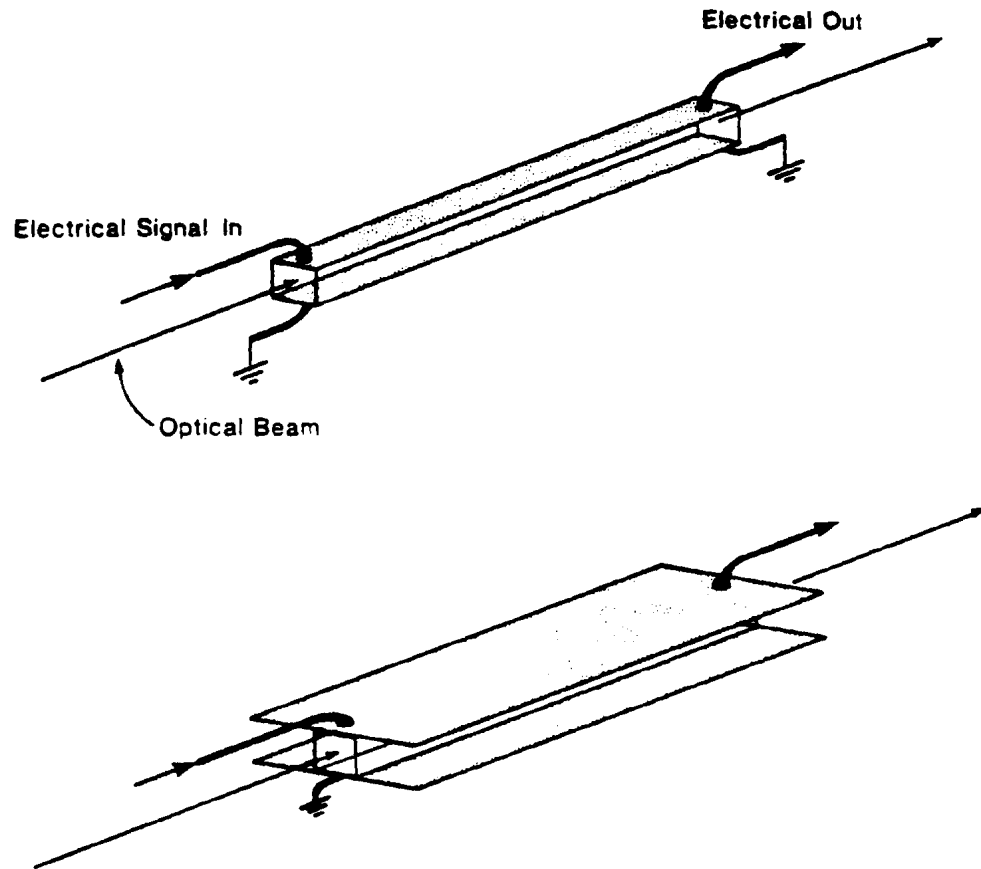


Figure II-11 Traveling-wave modulators

- a) Conventional electrode configuration
- b) Velocity compensated electrode configuration

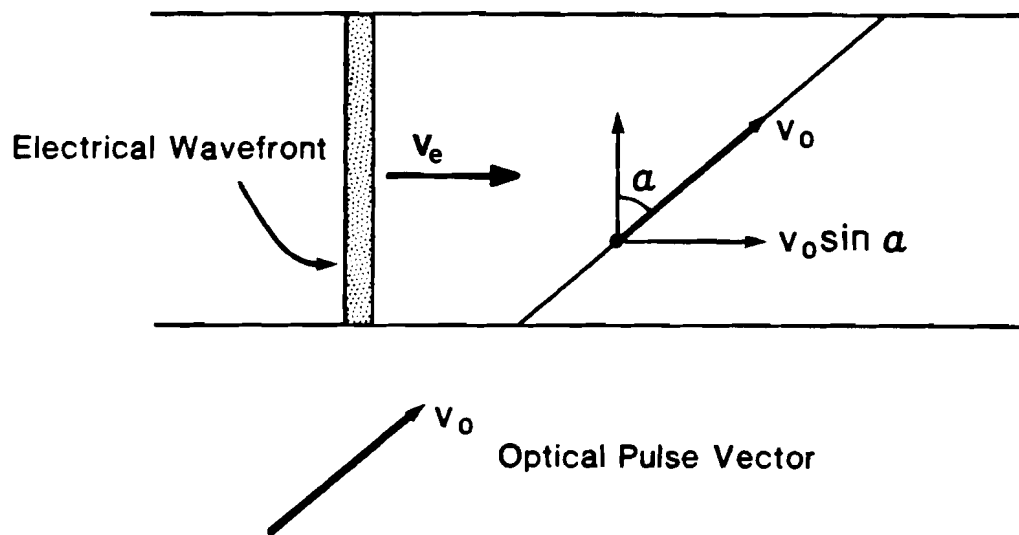


Figure II-12 Velocity matching geometry

optical signals with an angle of $(90-\alpha)$ between them. It is seen that if $V_o \sin \alpha = V_e$, a point on the optical beam will remain at precisely the same point of the electrical wavefront regardless of how far they copropagate. The optical pulse essentially "surfs" on the electrical wave.³⁴ This is the optimum condition for temporal resolution.

If the velocities are not equal, the optical pulse will not remain at precisely the same point on the electrical wavefront as they travel through the crystal and smearing will occur. Mathematically, this corresponds to a temporal smear or limiting resolution of \mathcal{T} as defined by:

$$\mathcal{T} = \frac{W}{c \cos \alpha} (n - \sqrt{\epsilon_{eff}} \sin \alpha). \quad \text{II-34}$$

In order to effect a perfect velocity match, an angle must be chosen so as to satisfy:

$$\sin \alpha = \frac{n}{\sqrt{\epsilon_{eff}}}. \quad \text{II-35}$$

Although precise velocity matching tends to be avoided in commercial modulators because of fabrication and implementation difficulties, the bandwidth performance is unsurpassed.

The velocity matched geometry has been discussed in several papers, for example DiDomenico and Anderson.³⁵ Kaminow and Liu³⁶ demonstrated that for the same crystal, they observed an increase in bandwidth from 3 GHz to 10 GHz by changing from the colinear to the velocity matched configu-

ration. The enhanced performance of the velocity matched method has also been shown by Auth³⁷ who achieved modulation up to 12 GHz. Kaminow et al.³⁸ has demonstrated the extreme bandwidth capability of the electro-optic effect used in this configuration by modulating the optical carrier wave at 964 GHz ($\tau < 1$ ps) using an infrared laser of the same frequency as the modulating electrical field.

From the above overview, we see that the electro-optic effect is ideally suited for high speed modulation when implemented as a traveling-wave modulator operating at the velocity matched angle. Theoretically⁷⁶ its temporal resolution could approach zero. The next section will detail the theoretical aspects of applying such modulators to the sampling of electrical transients with up to 1 terahertz bandwidth and subpicosecond temporal resolution.

II.C. The traveling-wave Pockels cell

From the previous section, we have found that the traveling-wave geometry for an electro-optic modulator offers the highest bandwidth capability. In this section, we will examine the various electrical and optical aspects of the traveling-wave configuration, with particular emphasis on the limiting operational parameters. The first part presents an analysis of stripline electrical characteristics as modelled by existing theories. The second part describes

the optical parameters and how they interact with the electrical wave. The interaction is modelled by a simple theory that predicts the best temporal resolution attainable in specific geometries.

II.C.1. Stripline electrical characteristics

The electrode geometry employed in traveling-wave Pockels cells is commonly referred to as a balanced strip transmission line. It is balanced, because both the signal and the ground electrodes are of the same width. We wish to investigate how such a transmission line behaves when used at extremely high frequencies with an electro-optic crystal as the dielectric medium.

Similar striplines, known as microstrip transmission lines are used extensively in microwave integrated circuits and have been theoretically modelled in great detail. Figure II-13 illustrates the differences in form as well electric field distribution for the balanced and microstrip geometries. It can be seen that the microstrip is basically half a balanced stripline. The form of the electric field is similar in both geometries, because the ground plane of the microstrip can be considered to be a mirror plane for the signal electrode. The signal electrode and its image form a balanced stripline of twice the microstrip thickness. For this reason, much of the theory that has evolved for the microstrip can be employed in analyzing the balanced line

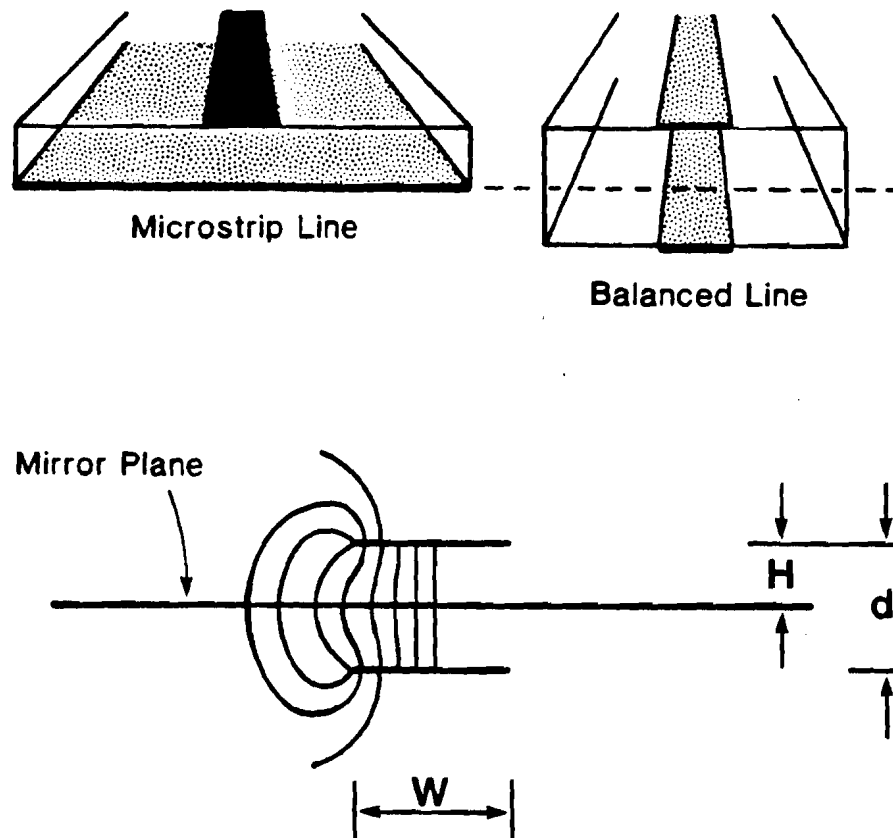


Figure II-13

Comparison of microstrip and balanced transmission lines

case as well. Mathematically, where the thickness between microstrip electrodes is specified, we use half the thickness of the balanced line.

Stripline electrode geometries are often referred to as open transmission lines because the form of the electrodes allows some of the electric field to reside outside the dielectric. The open geometry is in contrast to coaxial and wave guide geometries where all the field lines are contained within the dielectric medium. The distribution of the electric field between the dielectric and the surrounding medium in the open stripline case depends highly on the electrode width and separation, the relative dielectric constant and the frequency of the applied field. The form of the electric field distribution manifests itself as an effective dielectric constant, whose value, ϵ_{eff} , is less than that of the relative dielectric constant, ϵ_{rel} . ϵ_{eff} , in turn, affects the values of the impedance and electrical phase velocity.

In order to fully describe the variations of ϵ_{eff} , we must identify two frequency regimes in which the stripline exhibits different behaviour. At low frequencies, an induced electrical wave will propagate in a TEM-like mode having no longitudinal field components. The TEM-like mode is often referred to as a quasi-TEM mode due to the incomplete containment of the field lines within the dielectric

medium. In this low frequency regime, ϵ_{eff} is independent of frequency and is denoted by ϵ_{tem} . Since ϵ_{tem} is independent of frequency, both the impedance and the wave velocity are also independent of frequency. Thus the low frequency regime constitutes an ideal region of dispersionless operation. At higher frequencies, where the wavelength becomes comparable to the cross-sectional dimensions of the strip-line, ϵ_{eff} becomes a function of frequency, thereby making the transmission line dispersive. Dispersion is due to the propagation of higher order modes. Also, at higher frequencies, more field lines are contained within the dielectric and hence ϵ_{eff} increases. The limit is where no field lines emanate into the surroundings and ϵ_{eff} approaches ϵ_{rel} . The general relation can be written as:

$$\epsilon_{\text{tem}} \leq \epsilon_{\text{eff}} \leq \epsilon_{\text{rel}} . \quad \text{II-36}$$

Many methods have been used to define closed form expressions for the behaviour of ϵ_{eff} .³⁹⁻⁴⁵ A discussion of how these have evolved is given in Bahl and Trivedi.⁴⁶ We will only present calculations that apply to Pockels cell geometries that were used for the bulk of the experiments as well as one hypothetical case. Figure II-14 illustrates the form of the three modulator configurations that will be considered in detail. Only the first two were actually employed, while the third will be used to demonstrate the parameters of a possible ultra-high performance cell. The

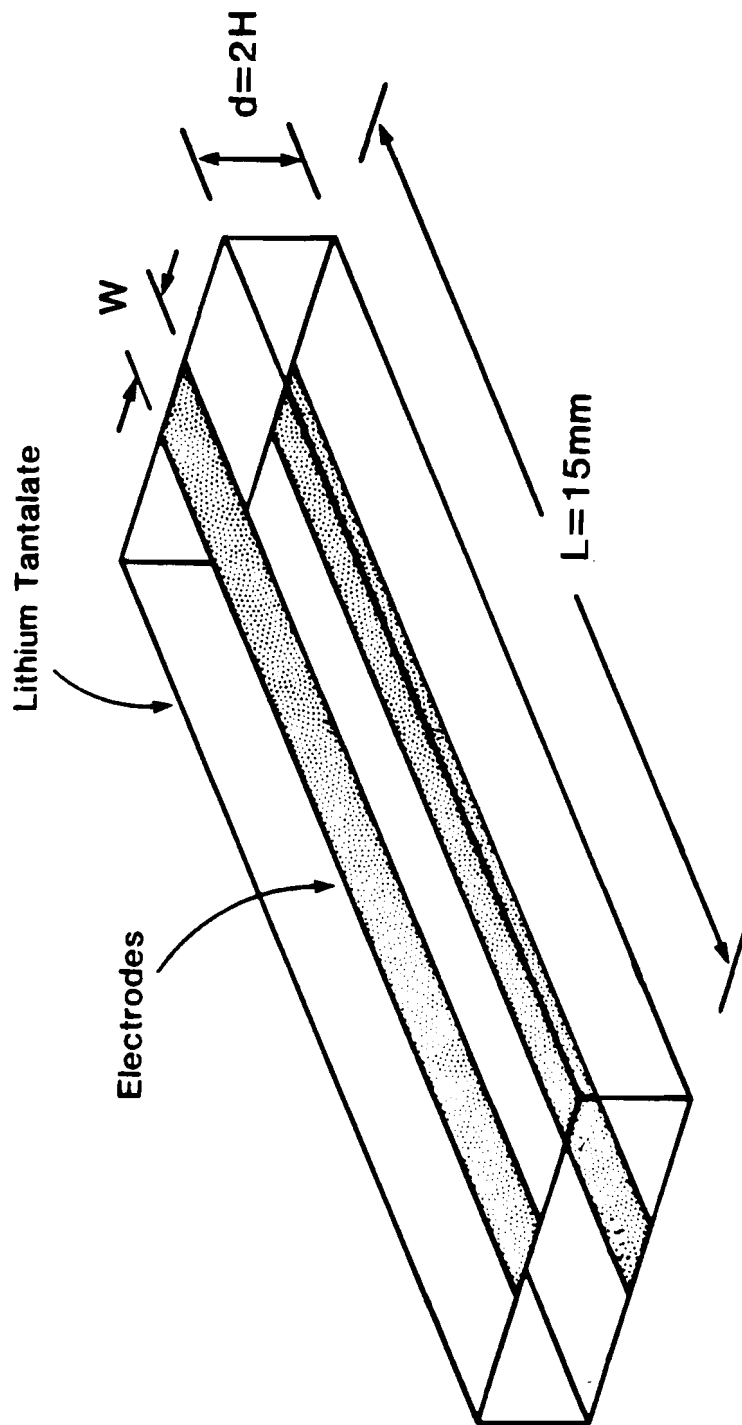


Figure II-14 Modulator electrode configuration

geometrical parameters of each cell are tabulated in Table II-1.

Mod.	d (μm)	H (μm)	W (μm)	H/W
A	250	125	300	0.42
B	100	50	125	0.40
C	10	5	10	0.50

TABLE II-1 Modulator Parameters

The most accurate and recent theory describing the quasi-TEM regime is given by Hammerstad.⁴⁷ In his work, equations are presented for \mathcal{E}_{tem} as a function of the height to width ratio of the electrodes, H/W , and \mathcal{E}_{rel} . Figure II-15a graphically displays this dependence for a lithium tantalate dielectric which has an $\mathcal{E}_{\text{rel}}=43$. The values of \mathcal{E}_{tem} are then used to calculate the TEM impedance, Z_{tem} , as a function of H/W (Figure II-15b). Since there is a significant fringing field, the extent of the electric field is wider than the actual electrode width. The fringing field gives rise to an effective TEM electrode width, W_{tem} , given by Owens⁴⁵ as:

$$W_{\text{tem}} = \frac{377 H}{Z_{\text{tem}} \sqrt{\mathcal{E}_{\text{tem}}}} \quad \text{II-37}$$

Figure II-15c shows W_{tem}/W as a function of H/W . From these graphs we can see that the effects of a larger H/W manifest themselves in several ways. An increased fringing field lowers the dielectric constant hence raising the electrical

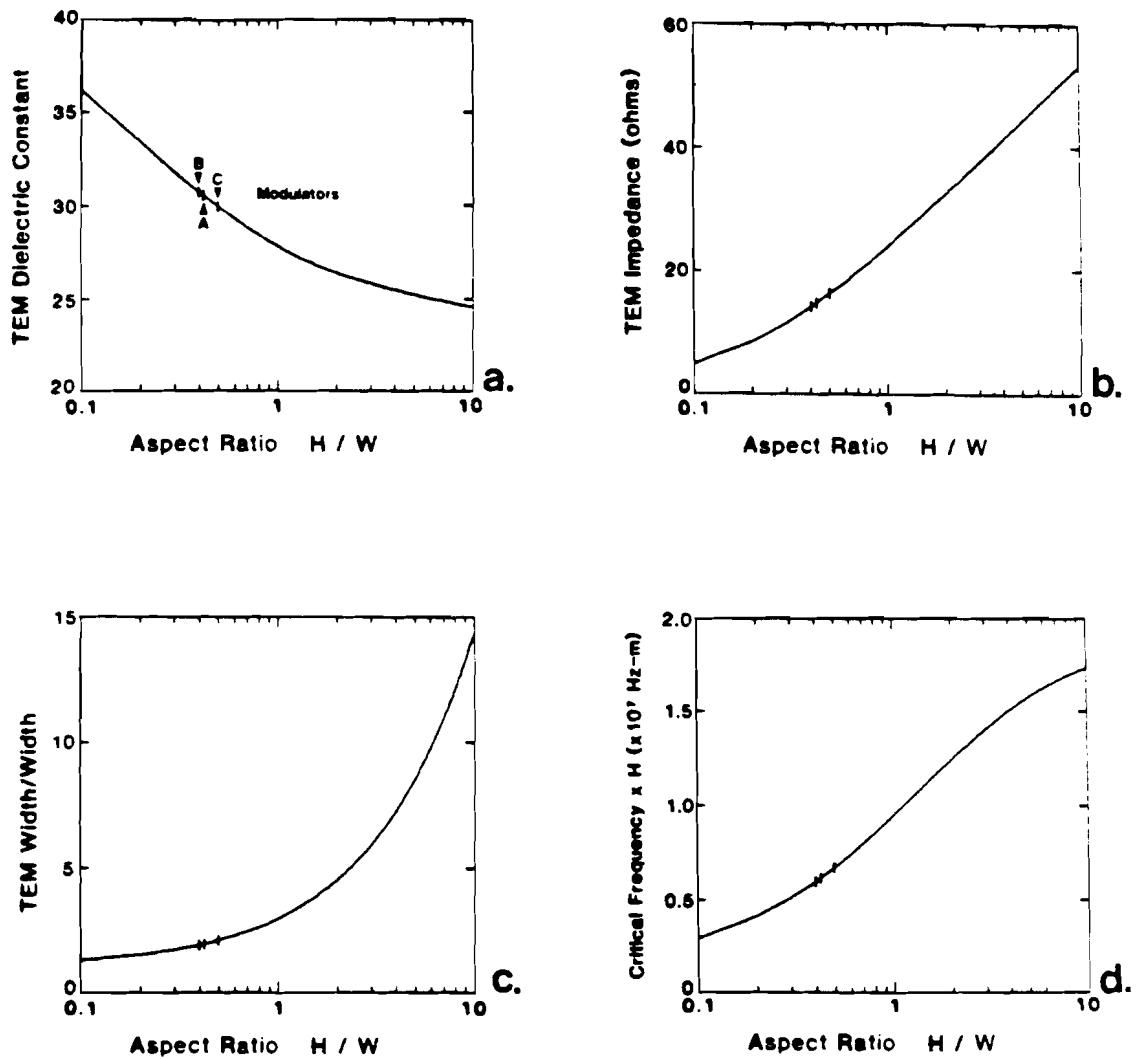


Figure II-15

Behaviour of modulator parameters as a function of the electrode aspect ratio

phase velocity. A smaller \mathcal{E} raises the impedance, while an enhanced fringe field also increases the effective width of the electrodes.

Our experimental geometries were chosen to optimize sensitivity while retaining the same basic aspect ratio from cell to cell. In this way, reducing the thickness in order to investigate frequency behaviour did not affect sensitivity or impedance matching considerations. The aspect ratios for each of the modulators considered are marked on the TEM value graphs. All configurations have an \mathcal{E}_{tem} of about 30, a Z_{tem} of about 15, and a W_{tem} of approximately twice the electrode width. The different characteristics of each modulator at high frequencies will be investigated using the following theoretical model.

Several empirical models for the frequency dependence of \mathcal{E}_{eff} have been developed.⁴²⁻⁴⁵ Recently, Yamashita et al.⁴⁸ have devised an approximate dispersion formula based on a rigorous theory.⁴⁹ This theory is more exact and applicable to a wider range of geometries and frequencies than previous models and hence is the model of choice. We further extend Yamashita's model to describe the dispersion of the effective impedance and effective electrode width.

As mentioned before, \mathcal{E}_{eff} ranges between \mathcal{E}_{tem} and \mathcal{E}_{rel} . The frequencies over which this dispersion takes place vary according to the stripline parameters, H/W and \mathcal{E}_{rel} .

Yamashita describes a critical frequency, f_c , within this dispersive regime, at which the onset of significant dispersive effects is realized. f_c corresponds to an electrical wavelength approximately equal to one quarter of the electrode spacing, H and is defined exactly by:

$$f_c = \frac{2.5c}{4KH\sqrt{\epsilon_{rel}-1}} \quad (c = 3 \times 10^8 \text{ m/s}) \quad \text{II-38}$$

where:

$$K = 0.5 + \left[1 + 2 \log \left(1 + \frac{W}{H} \right) \right]^2. \quad \text{II-39}$$

The above relationship is graphed in Figure II-15d by plotting the product of f_c and H as a function of H/W for $\epsilon_{rel}=43$. Thus, for a constant H/W we see that f_c is simply inversely proportional to H . By halving the electrode spacing we can expect to increase the dispersion free bandwidth to twice its original value. The above equation predicts that our modulators A, B, and C have critical frequencies of 49 GHz, 120 GHz, and 1300 GHz, respectively.

The dispersion relations for the dielectric constant, the electrode width, and the impedance are given by the following equations:

$$\sqrt{\epsilon_{eff}} = \sqrt{\epsilon_{tem}} + \frac{\sqrt{\epsilon_{rel}} - \sqrt{\epsilon_{tem}}}{1 + 4F^{-1.5}} \quad \text{II-40}$$

$$W_{eff} = W_{tem} - \frac{(W_{tem} - W)}{1 + 4F^{-1.5}} \quad \text{II-41}$$

$$Z_{\text{eff}} = \frac{377 H}{W_{\text{eff}} \sqrt{\epsilon_{\text{eff}}}} \quad \text{II-42}$$

where:

$$F = \frac{f H \sqrt{\epsilon_M - 1}}{7.5 \times 10^4} \left[\frac{1}{2} + \left\{ 1 + 2 \log \left(1 + \frac{W}{H} \right) \right\}^2 \right] . \quad \text{II-43}$$

The above relationships are all graphically depicted in Figure II-16 for modulators A and B. We see that ϵ_{eff} , W_{eff} , and Z_{eff} all follow the same functional form of the dispersion curve, but have shifted critical frequencies due to the difference in thickness. The shift in critical frequency implies that the thinner modulator B can propagate higher frequencies without dispersive effects.

Just as ϵ_{eff} varies between its two extreme values of ϵ_{tem} and ϵ_{rel} , we can define the high frequency values of Z_{eff} and W_{eff} , as Z_{rel} and W_{rel} , respectively. The following equations can thus be written:

$$Z_{\text{tem}} \leq Z_{\text{eff}} \leq Z_{\text{rel}} \quad \text{II-44}$$

and

$$W_{\text{tem}} \geq W_{\text{eff}} \geq W_{\text{rel}} (W) . \quad \text{II-45}$$

Figure II-16d is included to show that modulator C, with a thickness, H , of only $5 \mu\text{m}$ can propagate signals with

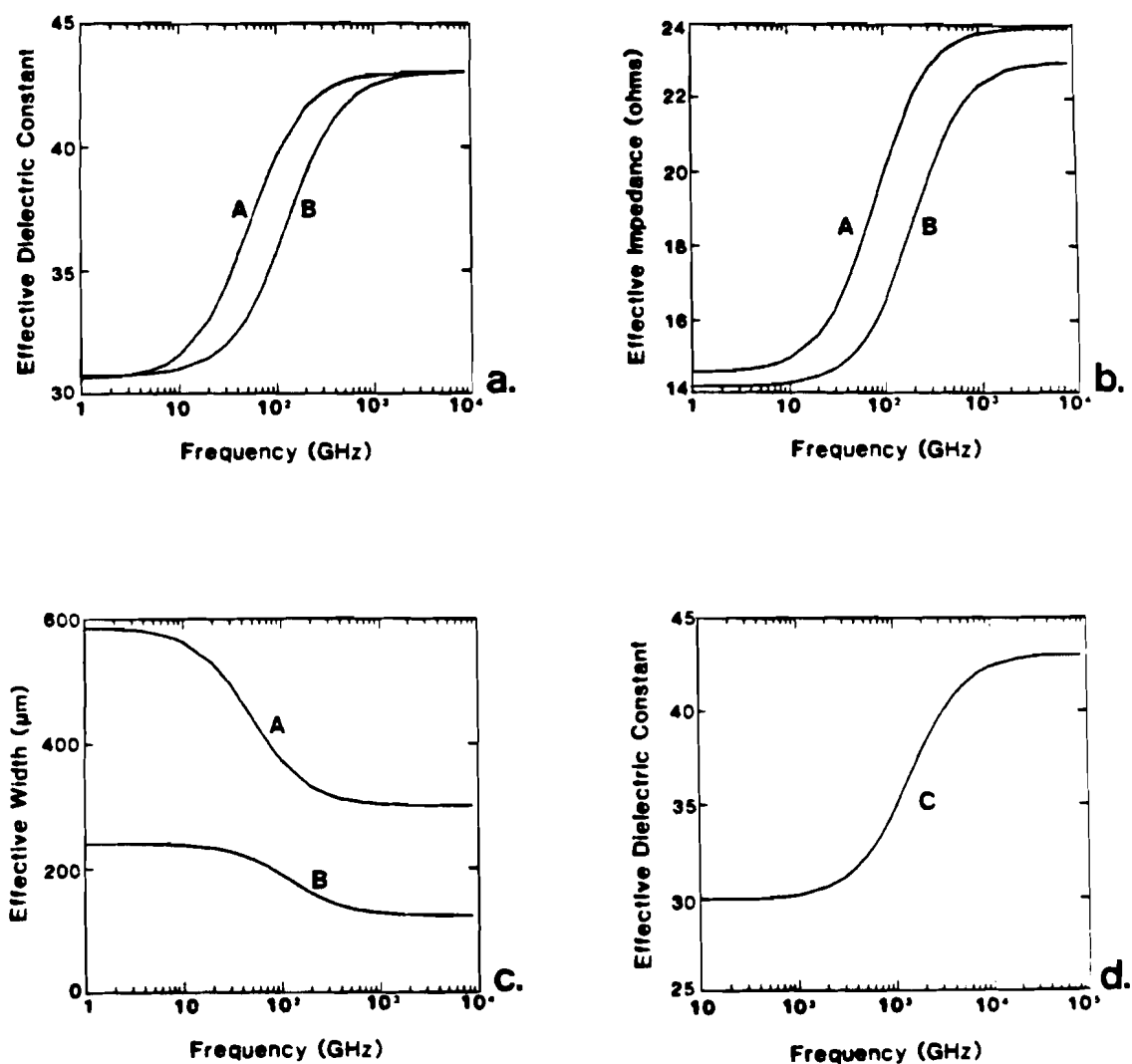


Figure II-16

Behaviour of modulator parameters as a function of frequency

a bandwidth up to almost 1 THz before encountering serious dispersive effects.

In order to develop a more complete understanding of how the electrode dimensions interact in producing the dispersion curves, we have plotted three families of curves in Figure II-17. We only wish to emphasize the general behavioural dependences that exist. The actual values of H and W do not necessarily represent practical configurations. Numerical values are listed for completeness.

Figure II-17a shows the behaviour of the ϵ_{eff} curves for several values of H with W held constant. As H decreases, we see that dispersion decreases while the critical frequency increases. Less dispersion and a higher critical frequency are both good properties for high frequency operation except that for low aspect ratios the TEM impedance is also very low, making coupling to conventional 50 ohm transmission lines difficult. To increase the impedance, the electrode width can be decreased. Figure II-17b shows several dispersion curves for various electrode widths that have a constant separation, H . In these cases, as the aspect ratio increases (decreasing W), we find that f_c increases again, but at the expense of increased dispersion as well.

Combining these two dependences on H and W by varying both quantities while holding their ratio constant, we gen-

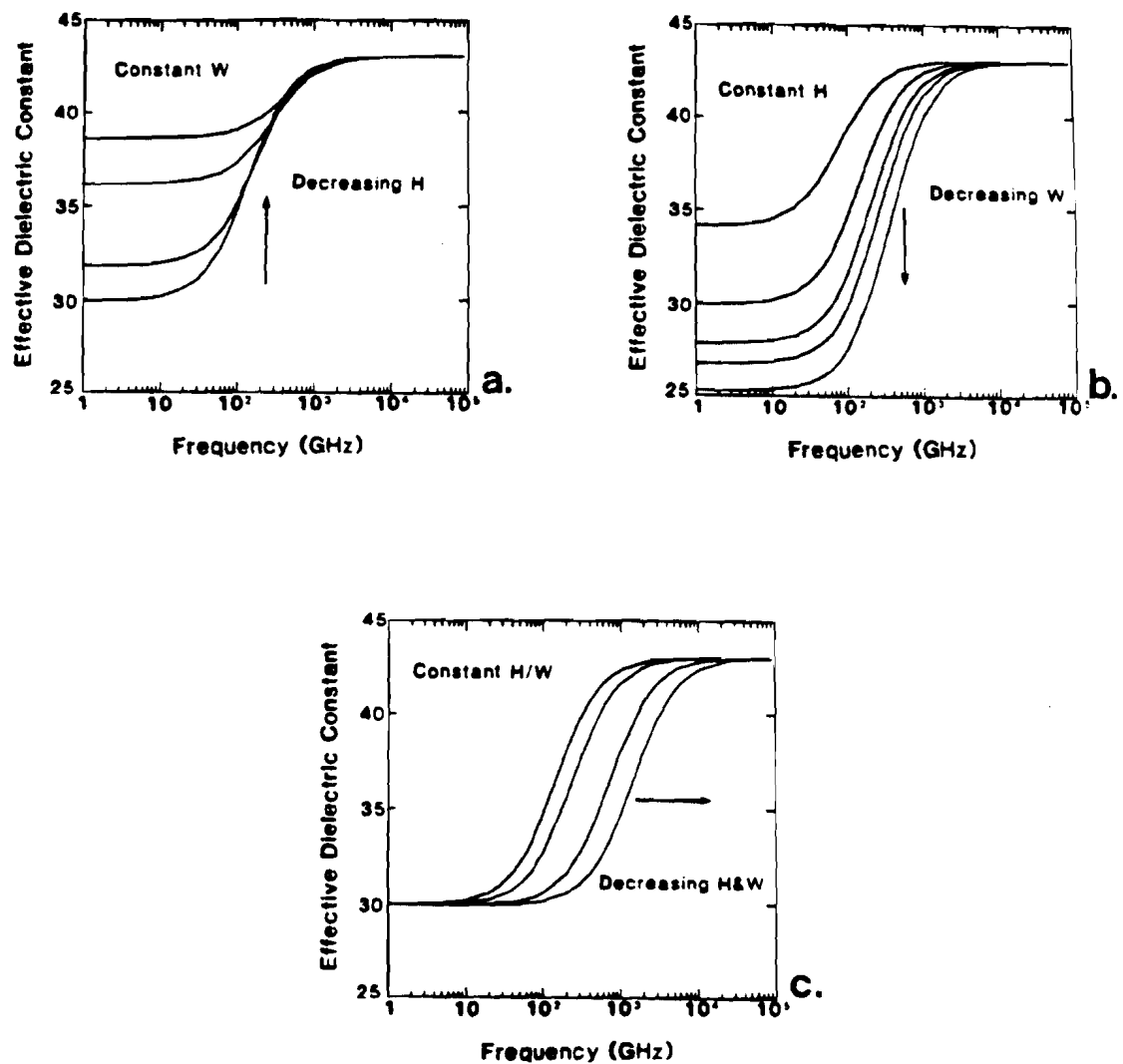


Figure II-17 Frequency dependence of the dielectric constant as a function of aspect ratio

erate the family of curves in Figure II-17c. Here, the above mentioned properties combine to yield some simple relationships that have been alluded to earlier. Both the TEM impedance and dispersion remain constant while the critical frequency is simply inversely proportional to H . It is for this reason that we have chosen to investigate a series of modulators that have a constant H/W .

From the above discussion we have learned that the electrical behaviour of the Pockels cell can change significantly near the critical frequency. A changing dielectric constant implies that if the unknown signal propagates any distance along the cell before it is sampled, dispersive effects may distort the signal's true shape. Dispersion occurs because higher frequency components experience a higher ϵ_{eff} , thereby decreasing their phase velocity with respect to lower frequency components that are below f_c . The dispersive impedance implies that not all frequencies will be coupled into the stripline with the same efficiency, hence distorting the electrical input spectrum. An effective electrode width that is frequency dependent will distort the measured signal because of dispersive sensitivity. Thus, in order to ensure a linear sampling mechanism, the electrode geometry must be carefully designed keeping in mind that the frequencies present in the unknown signal should be below the critical frequency of the stripline.

II.C.2. The electro-optical interaction and resolution

This section will analyze the interaction of the unknown electrical signal and its optical sampling pulse. By employing a simple theoretical model for optical pulse propagation through the Pockels cell combined with the electrical results of the previous section, we can predict the best temporal resolution attainable in any specific geometry. Results are presented for the three electrode configurations introduced in the previous section. The resultant graphs not only predict the ultimate temporal resolution but also identify the particular limiting parameters for a given situation.

In section II.B.4. we introduced the velocity matched geometry for a traveling-wave Pockels cell and arrived at equation II-33 that described the temporal resolution, τ , as a function of several parameters. The equation was derived for the ideal case of a delta-function optical pulse making a single traversal of the crystal. Experimentally, of course, the optical pulse has a finite pulse length and waist size.

A focussed gaussian laser beam can be characterized by two related quantities, the waist size, 2ω , and the Rayleigh range, $2Z_R$. The waist size refers to the diameter of the focussed beam at its narrowest point. The Rayleigh range is the distance about the focal point for which the beam

diameter is less than $\sqrt{2}$ times the waist size. In the Rayleigh range, the wavefronts can be considered to be plane, ie. of infinite radius. The waist size and Rayleigh range are defined as follows:

$$2w = 2(f/\#) \lambda \quad \text{II-46}$$

and

$$2z_R = \frac{1.5(2w)^2}{\lambda} \quad \text{II-47}$$

where $f/\#$ is the f-number of the focussed beam, and λ is the optical wavelength in air. Figure II-18 depicts the actual situation where the electro-optic crystal is placed in the focal region of a laser beam at normal incidence. It is assumed, for now, that the crystal width is less than the Rayleigh range of the focussed gaussian beam and therefore the waist size inside and outside the crystal are the same.

As discussed in section II.B.4., the temporal resolution is determined by how many points of the electrical signal influence a single optical pulse. Physically, the resolution is determined by the extent of the optical pulse in both time and space as it propagates between the electrodes. Figure II-19 shows, in detail, an optical pulse of finite size entering and propagating through the electro-optic crystal. The pulse, having a waist size in air of $2w_a$ and temporal duration, P , enters the crystal at an external angle of incidence, θ . Both the waist size and

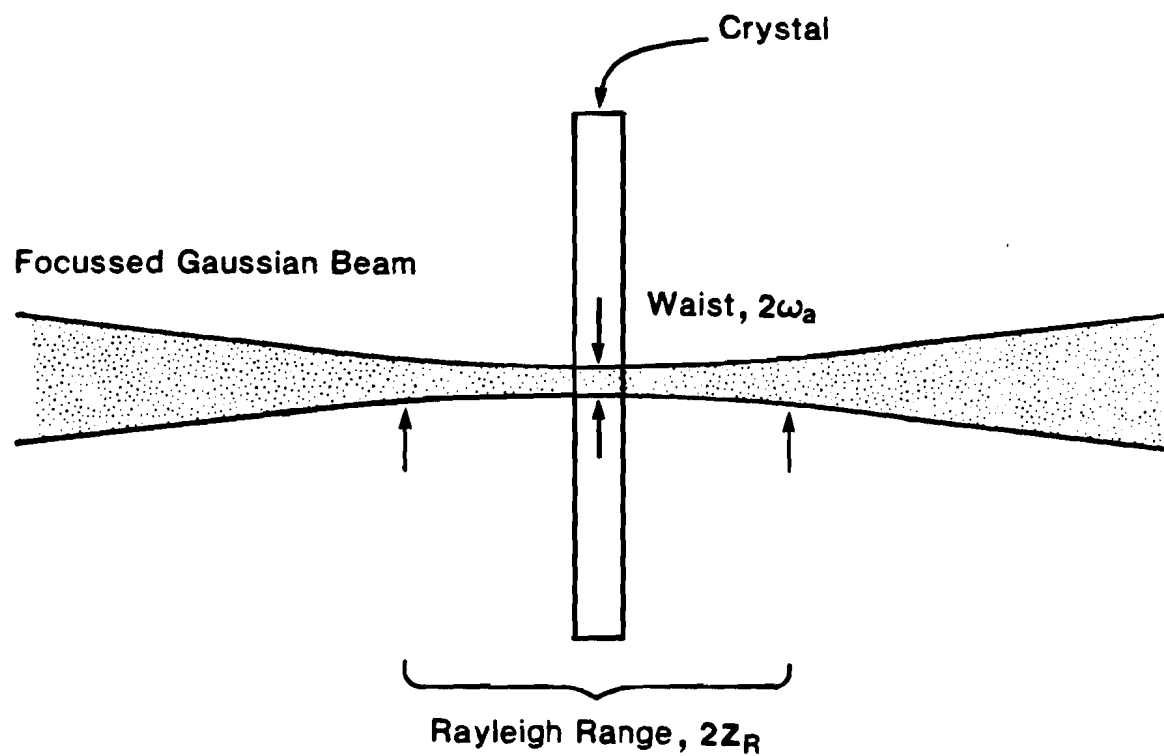


Figure II-18 Waist size and rayleigh range
for focussed gaussian beam

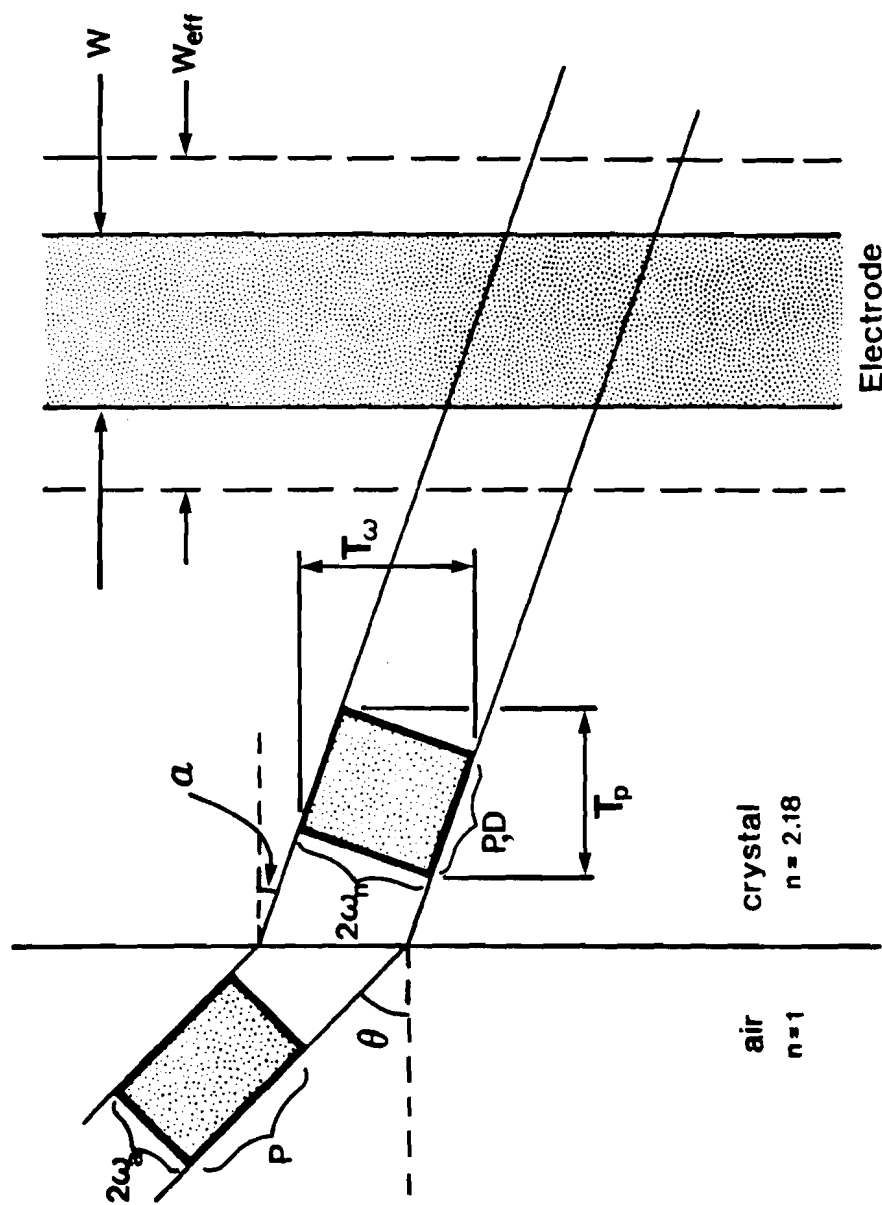


Figure II-19 Pulse propagation through the modulator crystal

temporal duration are assumed to be measured at the gaussian 1/e points.

Within the crystal, the angle of propagation is α . According to Snell's law:

$$\alpha = \arcsin\left(\frac{\sin \theta}{n}\right) \quad \text{II-48}$$

where n is the average index of the electro-optic crystal, $n=2.182$. The waist size inside the crystal, $2w_n$, increases with larger angles of incidence according to:

$$2w_n = 2w_a \left(\frac{\cos \alpha}{\cos \theta} \right). \quad \text{II-49}$$

The temporal duration, of course, remains the same, but its spatial extent, D , becomes:

$$D = P \left(\frac{c}{n} \right) \quad \text{II-50}$$

From the figure it can be seen that yet another effect arises due to the pulse having a finite extent. When propagated at an angle, the pulse length develops a component parallel to the interface, and the waist width develops a component normal to the interface. The additional components extend the waist width to an effective temporal width, T_w , and the pulse length to an effective temporal duration, T_p .

Given these quantities, T_w and T_p , we can now reexamine the velocity matching geometry in Figure II-20.

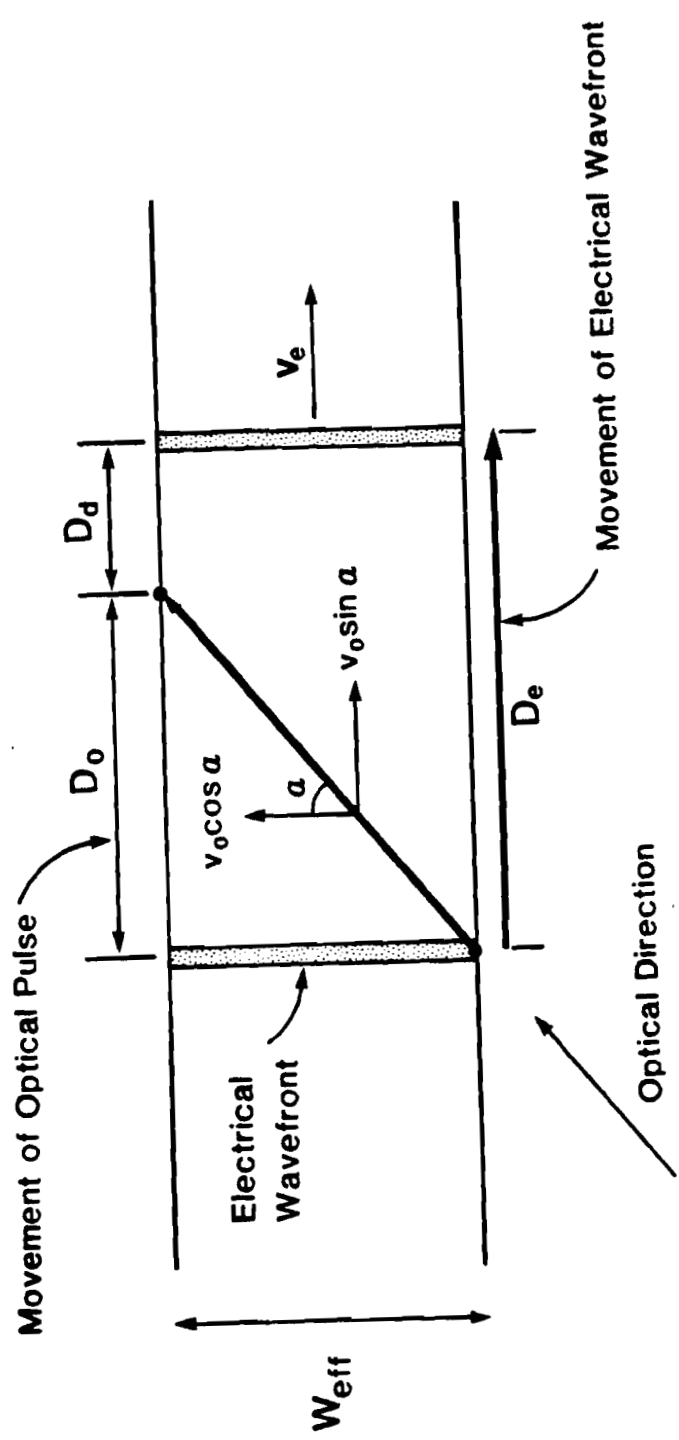


Figure II-20 Detail of the velocity matching geometry

There are two basic components that determine the temporal resolution for a particular geometry. The first component, τ_p , includes both the transit time for the optical pulse to cross the effective electrode width and also any additional effects due to the velocity matching geometry.

We derive the transit time for a pulse of finite length by first considering the transit time for a delta-function pulse. For the optical delta function, the time, t , spent under the effective electrode width is given by:

$$t = \frac{W_{eff}}{V_0 \cos \alpha} \quad II-51$$

For a finite pulse length, we must include the effects of τ_p . We define a new transit time, t' , by the convolved sum:

$$t' = (t^2 + \tau_p^2)^{1/2} \quad II-52$$

Therefore, the horizontal distances traveled by the optical pulse, D_o , and the electrical wavefront, D_e , are defined by:

$$D_o = (V_0 \sin \alpha) t' \quad II-53$$

and

$$D_e = V_e t' \quad II-54$$

The resulting spatial mismatch, D_d , gives rise to the temporal resolution figure, τ_p , given by:

$$\tau_p = \frac{(D_e - D_0)}{V_e} \quad \text{II-55}$$

which is:

$$\tau_p = \frac{1}{c} (n - \sqrt{\epsilon_{\text{eff}}} \sin \alpha) \left\{ \left(\frac{W_{\text{eff}}}{\cos \alpha} \right)^2 + (D \cos \alpha + 2W_n \sin \alpha)^2 \right\}^{\frac{1}{2}} \quad \text{II-56}$$

Equation II-56 reduces to equation II-34 for the delta function case where $D=W_n=0$. At the velocity matched angle, where $n = \sqrt{\epsilon_{\text{eff}}} \sin \alpha$, $\tau_p=0$. In other words, the component of the temporal resolution arising from propagation parallel to the electrical wavefront (actually zero at the velocity matched angle) is independent of the pulse length.

The second component contributing to the temporal resolution is denoted T_w . T_w is the time it would take for the electrical wavefront to cross the effective width of a stationary optical pulse and is given by:

$$T_w = \frac{2W_n \cos \alpha + D \sin \alpha}{V_e} \quad \text{II-57}$$

Combining τ_p and T_w as a gaussian convolution yields the final temporal resolution figure, τ :

$$\tau = (\tau_p^2 + T_w^2)^{\frac{1}{2}} \quad \text{II-58}$$

For the above analysis, we assumed that the width of the crystal was well within the Rayleigh range of the focussed beam. This is not necessarily the case. As will be seen, to achieve a high temporal resolution, a small

waist size is required. Subsequently, the Rayleigh range is also restricted. If the width of the crystal (with index n) is larger than the Rayleigh range, it can be shown that the waist size inside the crystal will be up to n times larger than the waist size in air. The geometry yielding an increased waist size is illustrated in Figure II-21.

All our modulators use focussing lenses with a focal length of 14 mm. A 2 mm diameter laser beam yields a waist size in air, $2w_a$, and Rayleigh range, $2Z_R$, given by:

$$2w_a = 2(7)(0.62\mu\text{m}) = 8.7\mu\text{m} \quad \text{II-59}$$

and

$$2Z_R = \frac{1.5(2w_a)^2}{\lambda} = 180\mu\text{m} \quad \text{II-60}$$

The crystal widths are $700\mu\text{m}$, much larger than the $2Z_R$ of $180\mu\text{m}$. Hence it is reasonable to assume that the actual waist size in the sampling crystals is close to n times $8.7\mu\text{m}$. In lithium tantalate, $n=2.182$ which implies a $2w_n \approx 19\mu\text{m}$. In the following graphs of temporal resolution we will consider a waist size of $15\mu\text{m}$ to $20\mu\text{m}$ to simulate the experimental conditions.

The results of the theoretical model just described are shown in Figures II-22 and II-23. All the graphs present temporal resolution as a function of the external angle of incidence, θ for various experimental conditions. For each

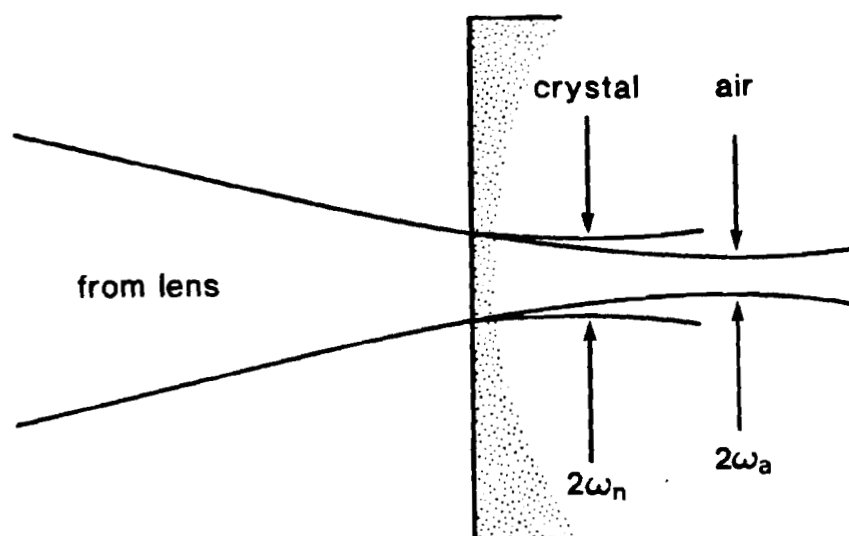


Figure II-21

Comparison of gaussian beam waist sizes
in air and in the crystal

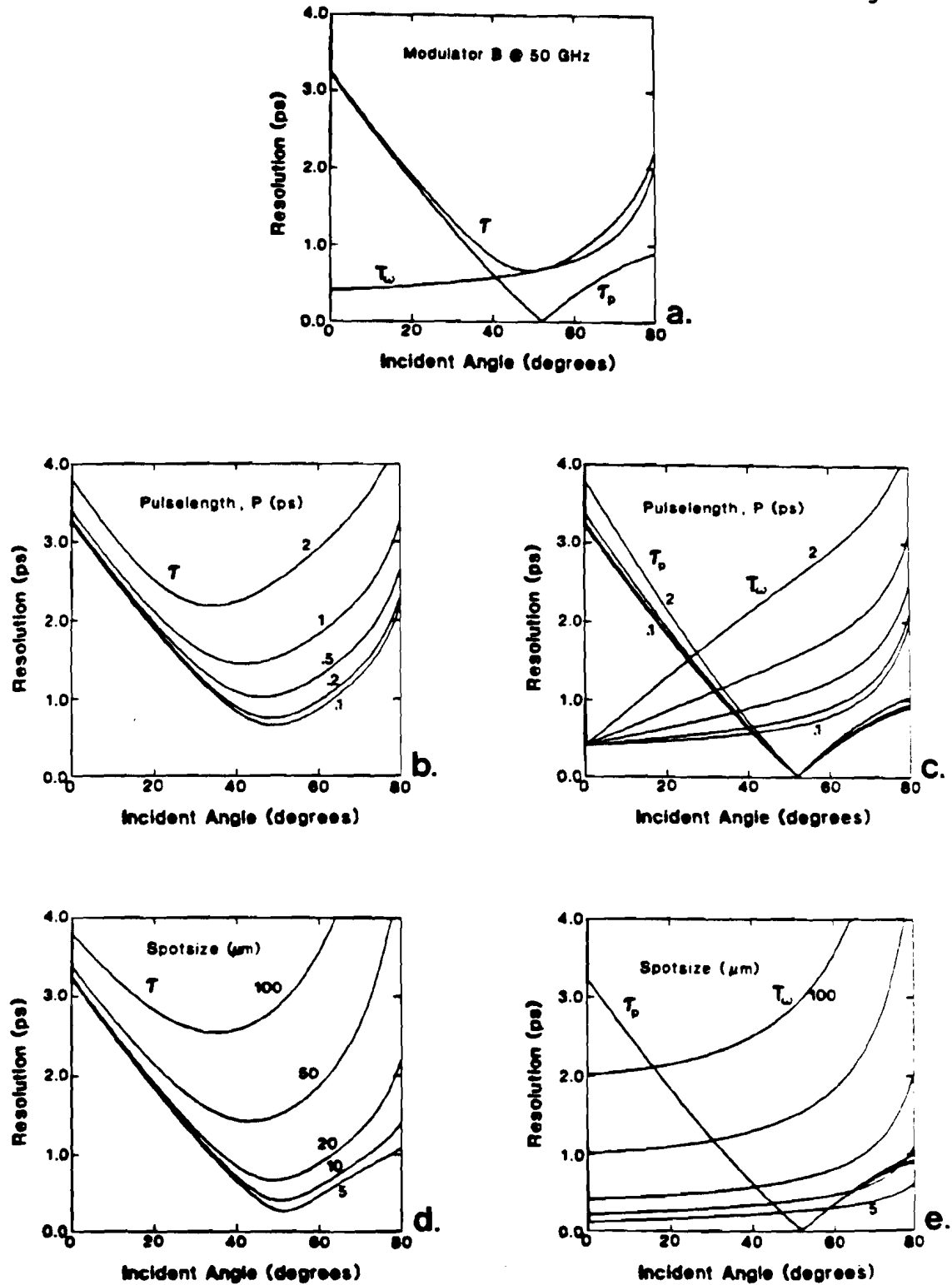


Figure II-22 Temporal resolution as a function of the incident angle (see text)

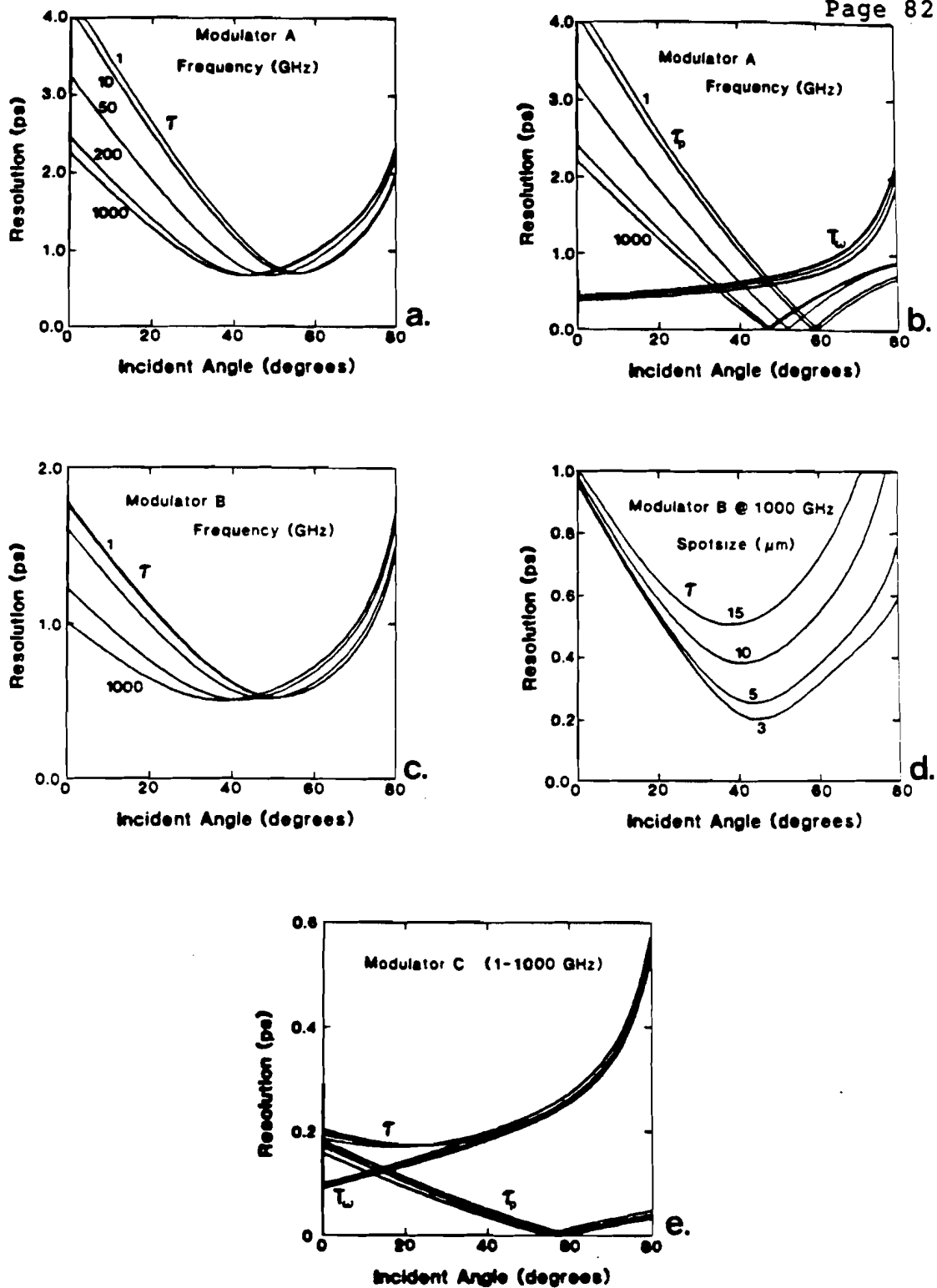


Figure II-23 Temporal resolution as a function of the incident angle (see text)

geometry, a specification of the pulse length P , waist size $2\omega_n$, index n , and effective width W_{eff} , will yield a unique angle where temporal resolution will be optimized. If the electrical frequencies are such that there is no dispersion, all frequencies will have the same optimum angle determined by \mathcal{E}_{tem} and W_{tem} . However, if dispersion does exist, only one frequency will be optimized as each frequency defines its own particular ϵ_{eff} and W_{eff} .

Figure II-22a shows a typical result for \mathcal{T} , together with its component parts, T_ω and \mathcal{T}_p . The curves were calculated for the $250\text{ }\mu\text{m}$ thick crystal operating at 50 GHz. These conditions define an ϵ_{eff} of 36.6 and a W_{eff} of $440\text{ }\mu\text{m}$. Pulse length and waist size were 120 fs and $20\text{ }\mu\text{m}$ respectively. We see that \mathcal{T}_p is a strong function of angle, defining the velocity matched angle (VMA) at 52 degrees. The minimum resolution angle (MRA) for \mathcal{T} occurs at 50 degrees and yields a corresponding minimum temporal resolution (MTR) of 690 fs. The shift of two degrees is due to the effect of a declining T at smaller angles. In general, \mathcal{T}_p dominates \mathcal{T} at small angles because of the gross mismatch in optical and electrical velocities. At large angles, T_ω dominates \mathcal{T} because of the increasing contribution of the pulse length to the effective width of the pulse.

Figure II-22b illustrates the effect of varying the pulse length, P , from 2 ps to 100 fs, keeping all other

variables constant at the values of Figure II-22a. Understandably, the MTR increases with P but the MRA decreases to smaller angles. The origin of this effect is clarified by observing the behaviour of T_ω and \mathcal{T}_p in Figure II-22c. The form of \mathcal{T}_p remains fairly constant, but T_ω is significantly affected by longer pulses propagating at an angle. The dominance of T_ω extends to smaller angles for longer pulses hence shifting the MRA to smaller angles also. At normal incidence, T_ω is limited only by the waist size of $20\text{ }\mu\text{m}$, regardless of P .

The effect of different waist sizes, now with P held constant at 120 fs, is depicted in Figure II-22d. As expected, larger waist sizes decrease resolution while also decreasing the MRA. In this case, the relationship between the MRA and waistsize is fairly linear, indicating that the waist size for this configuration is the most dominant effect. From Figure II-22e we see that the form of T_ω is basically the same from case to case. Changing the waist size merely shifts the curve on the vertical axis. Once again, the dominance of T_ω at large waist sizes dictates the shifting MRA.

From both of the above cases it can be seen that if P and $2\omega_n$ are allowed to go to zero, the MRA approaches the VMA as predicted earlier for the ideal case of a delta function. We will now investigate the frequency dependence of

the three modulators A, B, and C as introduced in section II.C.1. In all cases, everything is held constant except the frequency, which in turn determines the effective values of the electrode width and the dielectric constant.

Figure II-23a illustrates the frequency dependence for modulator A, having an electrode spacing of $250\text{ }\mu\text{m}$. It is seen that the MTR does not change appreciably with frequency, only shifting to smaller angles at higher frequencies. Figure II-23b shows that this behaviour arises from the shifting VMA of τ_p , which in turn is simply due to the increased values of ϵ_{eff} at higher frequencies.

From Figure II-23a we deduce that the optimum operating angle for all frequencies is the MRA for the highest frequency. In this case the MRA is approximately 43 degrees for the 1 THz component, yielding a MTR of 670 fs. At this angle the resolution for the 1 GHz component is reduced to 1.2 ps, but this resolution is much more than adequate, because the maximum risetime in a 1 GHz signal is only 350 ps. With a MTR of 670 fs, the maximum frequency that this geometry can resolve is approximately 520 GHz.

The $100\text{ }\mu\text{m}$ thick crystal of modulator B is modelled for the same parameters as modulator A except that the waist size has been reduced to $15\text{ }\mu\text{m}$ to agree more closely with the experimental situation that has been investigated. The results are presented in Figure II-23c. This plot shows

that the best performance occurs at a MRA of 38 degrees resulting in a resolution of 510 fs which corresponds to a resolvable bandwidth of 690 GHz. One can also see that the vertical separation of the curves for modulator B has been reduced by about a factor of two with respect to those of modulator A. The closer spacing is due to the increased critical frequency of modulator B reducing the dispersion over this frequency range. The effects of waist size in this geometry are still dominant as can be seen from Figure II-23d. By reducing the waist size from $15\text{ }\mu\text{m}$ to $3\text{ }\mu\text{m}$ one could still significantly enhance the minimum resolution from 510 fs to 200 fs.

Figure II-23e depicts the superb frequency response of the hypothetical modulator C. Because of its greatly reduced size, modulator C has a critical frequency of 1.3 THz. Such a high critical frequency markedly decreases the dispersion for frequencies below 1 THz. In addition, by employing optical pulses of 100 fs duration focussed to a waist size of $5\text{ }\mu\text{m}$ this modulator could achieve a temporal resolution of 180 fs at an angle of 16 degrees. The resolution and extremely high critical frequency imply that a modulator of these dimensions could be used to sample electrical pulses containing frequencies up to 1 THz without incurring significant dispersive effects. With the availability of modern fabrication facilities, it seems reasonable that such a device could be developed.

In summary, we have modelled two components of the temporal resolution, T_w and T_p , that dictate the overall temporal resolution, T , attainable for any particular geometry. T_w and T_p depend on the values of the optical pulse length, waist size and frequency of the applied electrical field. These quantities, in turn, determine one optimum angle for which the best temporal resolution is achieved. The experimental modulators A and B are expected to attain temporal resolutions of 670 fs and 510 fs respectively when operated near a 40 degree external angle of incidence with a sampling beam focussed to 15 μm . The theory also predicts that a temporal resolution of near 200 fs should be achievable with the existing modulator B by reducing the optical waist size to about 3 μm .

II.D. Noise, sensitivity and signal processing

This section will discuss the effects of noise on the sensitivity of the modulator and detection system. We will describe the major sources of noise and their characteristics, together with electronic methods of processing the acquired signal so as to enhance sensitivity.

The ultimate limit in the detectability of signals is set by noise. Noise can be considered to be any additional signal that obscures the desired signal. There are three main sources of noise in a typical detection system. The

first, and most fundamental, is a real fluctuation in the actual signal being measured, typically shot noise, thermal noise or $1/f$ noise. These forms of noise are unavoidable and represent the true limit in detection sensitivity. The second form of noise is that introduced by interference. Interference usually arises from adjacent optical and electronic equipment and can usually be eliminated by careful design. The third noise contribution is due to the amplification process. This noise can also be minimized so that it is not a significant element by the choice of an appropriate low-noise amplifier. For the following discussion we will assume that we have a "clean" experiment where interference and amplifier noise are negligible.

Figure II-24 depicts the simplified detection scheme used in our sampling system. A reverse biased photodiode receives the DC optical intensity, I_s , from the modulator and converts it into a proportional current, i_s , that flows in the detection circuit. The current flows through the load resistor R_L , and generates a voltage, V_s . The photodiode also generates a dark current, i_d , that produces a voltage, V_d , at the load resistor. The total output voltage, V_L , is given by:

$$V_L = V_D + V_S \quad \text{II-61}$$

We first consider shot noise that accompanies the

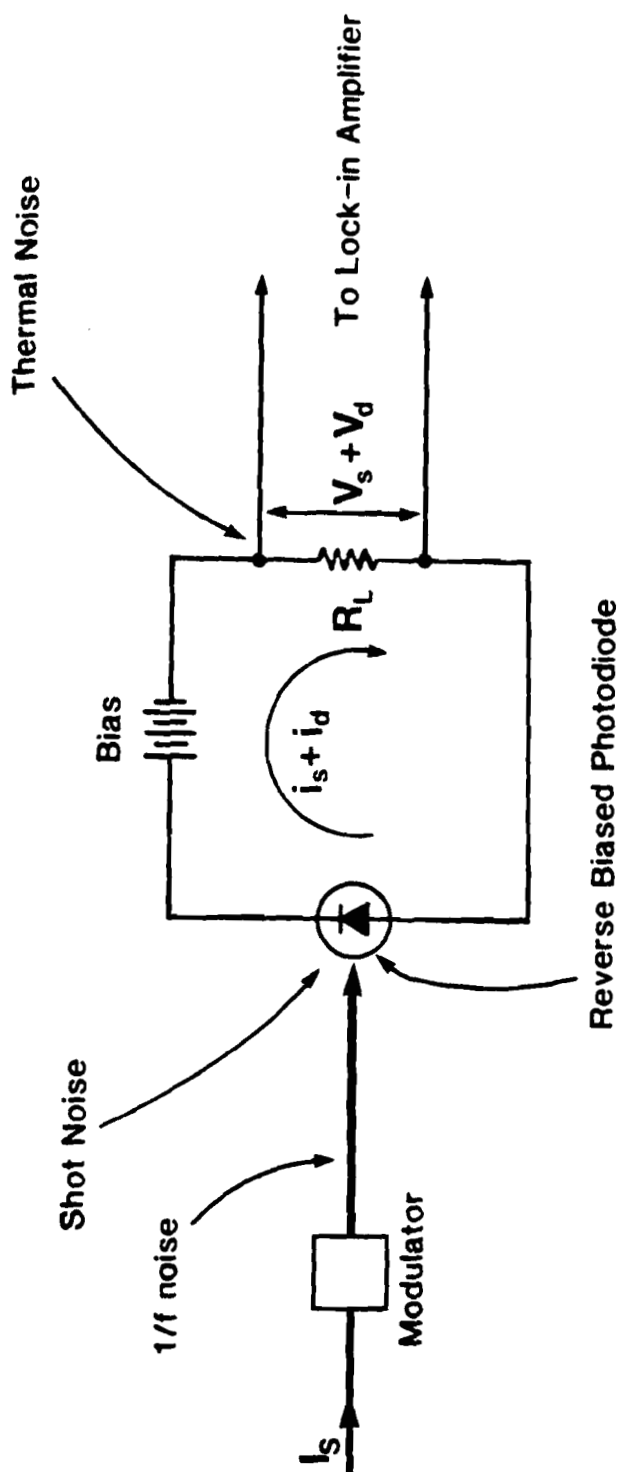


Figure II-24 Sources of noise in the detection circuitry

signal. Shot noise is due to the probalistic nature of the generation of the electrical charge within the detector.⁵⁰ The origin of this type of noise can be considered due to either the quantized nature of the optical field (photons), or the quantized nature of the electrical charge (electrons). The spectrum of shot noise is flat (white noise), meaning that there is the same noise power in each hertz of frequency.⁵¹ Shot noise manifests itself as fluctuations in the circuit current given by:

$$i_{noise}(rms) = (2q i_{dc} B)^{1/2} \quad II-62$$

where q is the electron charge (1.6×10^{-19} coulombs) and B is the bandwidth of the measurement system. In our system, there are two components to shot noise, one arising from the signal current, i_s , and the other from the constant dark current, i_d . Therefore, the shot noise for our scheme is given by:

$$i_{noise}(rms) = (2q B (i_s + i_d))^{1/2} \quad II-63$$

The dark current is an intrinsic characteristic of the reverse biased photodiode, while the signal current depends on the optical intensity and the responsivity of the detector. The current noise can be converted to a voltage fluctuation by applying Ohms law as follows:

$$V_{SHOT}(rms) = R_L i_{noise}(rms) \quad II-64$$

Another source of unavoidable noise in the signal is the load resistor. Thermal fluctuations of the charge carriers within the resistor generate Johnson, or thermal noise. Thermal noise appears as a fluctuating voltage across the terminals of the resistor. The thermal noise voltage can be calculated from:

$$V_{\text{THERMAL}}(\text{rms}) = (4kTR_e B)^{1/2} \quad \text{II-65}$$

where k is Boltzmann's constant and T is the absolute temperature in degrees Kelvin. Thermal noise is also white (flat spectrum).

A third, and usually dominant source of signal noise, is known as one over f ($1/f$), or flicker noise. It has a spectrum whose amplitude increases towards DC in such a way that there is equal noise power per decade of frequency. Noise with this spectral dependence is commonly referred to as pink noise. Pink noise arises from many sources and is usually noticeable, and disturbing, at frequencies below 1 kHz. Typical sources of this type of noise in the measured signal are temperature fluctuations, air currents, powerline voltage fluctuations, and variations in laser intensity. In the electro-optic sampling system, the dominant source of flicker noise is the laser intensity, I_s (DC-100 MHz). Although the amplitude of this type of noise cannot be mathematically predicted, it is a real experimental obstacle.

The noise amplitude one measures depends on bandwidth and hence can be characterized by a noise voltage density, v_n . v_n is the noise voltage per unit bandwidth and can be written:

$$v_n = \frac{V_{noise}}{B^{1/2}} \cdot \left(\frac{\text{volts}}{\sqrt{\text{Hz}}} \right) \quad \text{II-66}$$

For white noise, v_n is constant with frequency whereas pink noise has a v_n that drops off at 3 dB/octave for increasing frequency. Noise power per unit bandwidth is also commonly specified and is defined by:

$$v_n^2 = \frac{V_{noise}^2}{B} \cdot \left(\frac{\text{volts}^2}{\text{Hz}} \right) \quad \text{II-67}$$

The usual method for specifying how much noise is present in a certain signal is the signal to noise ratio (S/N). It is the ratio, in decibels, of the rms voltage of the desired signal to the rms voltage of the noise that is also present. Mathematically, the S/N is defined as:

$$\frac{S}{N} = 20 \log \left(\frac{V_s(\text{rms})}{V_n(\text{rms})} \right) \text{ dB.} \quad \text{II-68}$$

Since all the above noise sources are unavoidable, we must call upon an electronic system to limit their effects. As we have discovered, the amplitude of the measured noise voltage depends upon the bandwidth of the detection system. The simplest means by which to reduce the effects of noise,

then, is to reduce the detection bandwidth. For white noise, this technique works equally well for any frequency, but for pink noise the noise power per unit bandwidth increases towards DC. Thus, we not only wish to narrow the bandwidth but also move the central frequency of the passband away from DC. For $1/f$ noise, as described before, a center frequency near 1 kHz should avoid the largest effects. An instrument specifically designed for this purpose is the lock-in amplifier.⁵²

The lock-in amplifier is an extremely low noise, high gain, AC amplifier that can be tuned to virtually any frequency with a bandwidth of less than 10^{-3} hertz. Its output is a DC signal proportional to the rms AC input amplitude. In order to apply this extremely powerful instrument, the signal of interest must be made periodic. For our sampling system, periodicity can be introduced in a couple of ways. Since the signal source is optically triggered, a mechanical or optical chopper can be introduced in the trigger beam. If the electrical source requires a bias voltage to generate its signal, then the bias can simply be oscillated. Both modulation methods must provide a synchronous AC signal that the lock-in amplifier can "lock" to. Synchronism is important not only to prevent frequency drifting, but to also allow the amplifier to measure the input signal with the proper phase relationship.

The bandwidth of a lock-in amplifier is controlled by its time constant (TC) setting which controls the bandwidth of the final filtering stage.⁵² TC is simply related to the bandwidth by:

$$B = \frac{1}{8(\pi)} \quad \text{II-69}$$

for a filter with a 12 dB/octave rolloff. It can be shown that to increase V_s/V_n by n times for white noise, the detection bandwidth must be decreased by a factor of n squared. This relationship implies that for a 20 dB S/N improvement, the bandwidth must be decreased by a factor of 100. A typical operating TC is 300 ms which corresponds to a bandwidth of 0.42 Hz. For a photodiode circuit with an upper frequency limit of 2 kHz, for example, a TC of 300 ms reduces the bandwidth by $2000/0.42$ or 4760. V_s/V_n is enhanced by a factor of $\sqrt{4760} = 69$, which implies a S/N enhancement of 37 dB. If the entire 350 MHz bandwidth of a fast photodiode is used as the input to the lock-in amplifier, a bandwidth of 0.42 Hz will yield a S/N enhancement of almost 90 dB.

The S/N can be further increased by repetitive signal averaging. A signal averager⁵³ is basically a storage oscilloscope that averages together successive traces. If the desired signal is synchronized with the sweep of the averager, the signal will add coherently for integrated sweeps while random noise fluctuations will add

incoherently. It can be shown⁵¹ that this process is equivalent to bandwidth narrowing. Thus, analogous to the lock-in amplifier, V_s/V_n increases with the square root of the number of sweeps.

The signal recovery technique of bandwidth narrowing, however, is not for free. Restricting the bandwidth produces a trade off between S/N and the time taken to attain that particular S/N. To achieve a specific noise level, one must either set a long TC (narrow bandwidth) and take a few sweeps very slowly, or repeat many scans with the signal averager using a shorter time constant. The time taken to acquire the signal is often referred to as the integration time, and will be spoken of in the experimental section. Either technique will achieve the same degree of bandwidth narrowing in comparable integration times.

Although 1/f noise from the laser is significantly reduced by the above techniques, in our system, an additional noise reduction technique using differential detection is possible. Figure II-25 illustrates the configuration of the modulator's second polarizer and detectors. The intensity of the laser beam before the analyzer can be represented by:

$$I = I_{dc} + N(t) \quad \text{II-20}$$

where the bandwidth is such that the individual pulses are not resolved and $N(t)$ represents the 1/f noise component of

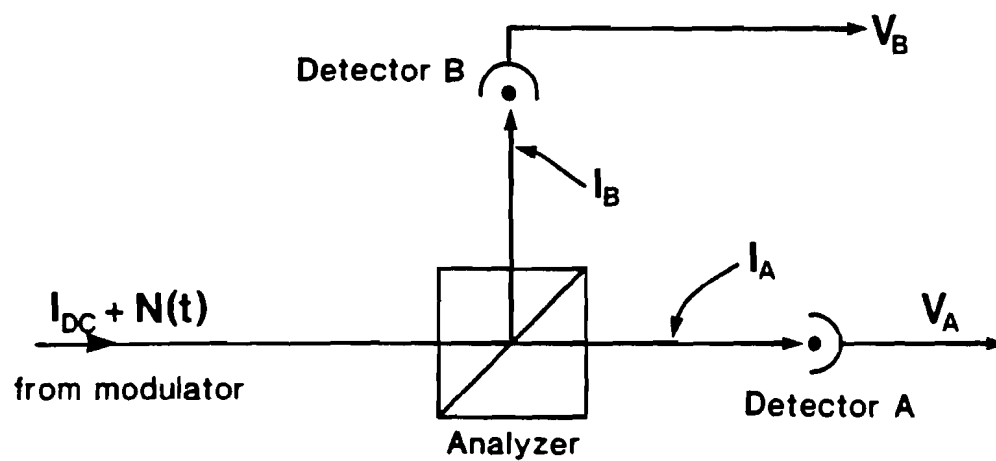


Figure II-25

Differential detection arrangement for noise subtraction

the beam. If we place a modulating voltage, V , on the Pockels cell (biased at quarter wave) of the form:

$$V = V \sin \omega t \quad \text{II-71}$$

we will get a resulting intensity modulation for the transmitted beam given by:

$$I_A = \frac{1}{2} (I_{DC} + N(t)) + A \sin \omega t \quad \text{II-72}$$

where A is the amplitude of the intensity modulation due to the applied voltage V . Because the rejected beam has the complementary modulation, its intensity is given by:

$$I_B = \frac{1}{2} (I_{DC} + N(t)) - A \sin \omega t . \quad \text{II-73}$$

$N(t)$ is not complementary because it is a fluctuation of intensity, not polarization.

The voltages, V_a and V_b , generated by the detectors are linearly proportional to the incident intensities, I_a and I_b , respectively. By subtracting the voltages, we get a difference voltage, ΔV , of the form:

$$\Delta V = k (I_A - I_B) = 2kA \sin \omega t \quad \text{II-74}$$

where k is the proportionality constant. If k is identical for both channels, then both the DC intensity and its noise component $N(t)$ vanish. An added benefit from this differential scheme is that the signal voltage is enhanced by a factor of two. The effectiveness of differential detection

will be elaborated upon in the experimental chapter.

We have described three powerful signal processing techniques, lock-in amplification, signal averaging, and differential detection, each with its own attributes. The effectiveness of each and the overall performance depend on the experimental devices and conditions. Instead of analyzing hypothetical situations in this section, we will postpone numerical calculations until the experimental system has been described. There, we will be able to enlist actual experimental quantities in the calculation of sensitivity and the noise limit.

II.E. Transient sampling theory

This section will mathematically describe the sampling operation and illustrate how it maps the unknown waveform from its original picosecond time domain into an equivalent time regime more readily processed by conventional electronic systems.

Figures II-26a and b depict the signals present at the electro-optic crystal. The train of optical sampling pulses is given by $S(t)$ which represents pulses of width \mathcal{T} separated by a time R . The sampling pulsewidth, \mathcal{T} , is defined to be the effective temporal resolution of the sampling head configuration as described earlier in section II.C.2. The pulse separation, R , is determined by the laser repetition

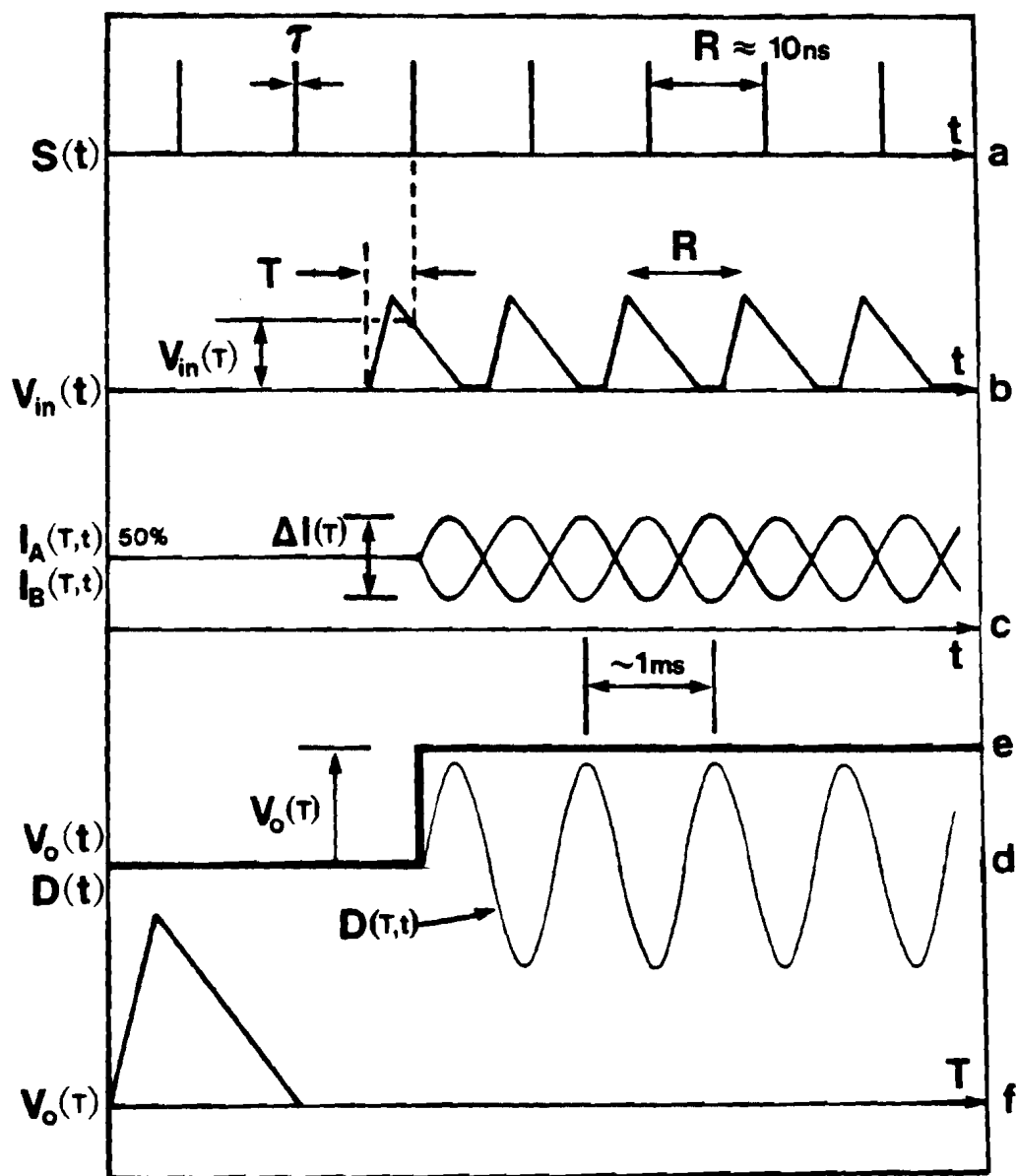


Figure II-26 Electrical signals at various points of the sampling system (see text)

rate which is typically about 100 MHz, corresponding to a separation of 10 ns. The unknown electrical transients are modelled by the repetitive triangular function, $V_{in}(t)$ which also has a pulse spacing of R . The two signals are precisely synchronized without jitter and meet in the electro-optic crystal with a variable relative delay of T .

From section II.B.2. we know that the change in the resultant intensity transmitted through the modulator is linearly proportional to the voltage sampled by the optical pulse. The sampling relation can be expressed as a cross correlation between the optical and electrical signals as follows:

$$\Delta I(\tau) = k \int_{-\infty}^{\infty} V_{in}(t) S(t-\tau) dt \quad \text{II-75}$$

where ΔI is the output intensity and k is a constant of proportionality. For simplicity we can assume that the sampling pulse width, (resolution), is much less than the temporal characteristics of the electrical transient. This assumption is realistic since we expect to characterize electrical signals having durations of tens or hundreds of picoseconds with a technique that has subpicosecond resolution. Using the above approximation, we can consider $S(t)$ to be a train of delta functions. Thus, equation II-75 becomes:

$$\Delta I(\tau) = k \int_{-\infty}^{\infty} V_{in}(t) \delta(t-\tau) dt \quad \text{II-76}$$

From convolution theory, it is well known that the solution to this integral is:

$$\Delta I(\tau) = k V_{in}(\tau) \quad \text{II-77}$$

Thus, $V_{in}(t)$ has been mapped into a linearly proportional intensity, ΔI , as a function of the variable T .

T is a quantity that is readily measured by conventional means, and is linearly related to the actual temporal delay between $S(t)$ and $V_{in}(t)$. In optical systems, delay is usually introduced by a moving mirror, in which case T is a measure of the distance the mirror moves. Since the speed of light in air is well known, the conversion from distance to time is extremely accurate. We define $T=0$ as the delay position where the optical sampling pulse coincides with the beginning of the portion of the electrical signal of interest (see Figure II-26b).

How the sampling process manifests itself within the detection system is depicted in Figures II-26c-f. With the modulator biased at its quarter wave point, and no signal present on the crystal, the output intensities I_a and I_b are equal at 50% (Figure II-26c). With the signal on, and a relative delay of T , an intensity change of $I(T)$ is induced. If a lock-in amplifier is being used, then $V_{in}(t)$ oscillates and $\Delta I(T)$ becomes a function of t also, ie. $\Delta I(T, t)$. Since I_a and I_b are complementary, their oscilla-

tions are out of phase and of equal amplitude. The voltages proportional to $\Delta I(T,t)$ from the detectors are then subtracted to yield the differential voltage $D(T,t)$ as the input to the lock-in amplifier (Figure II-26d). The output from the lock-in, $V_o(T)$, is a DC level dependent only on T , as shown in Figure II-26e. Thus, by increasing T from $T=0$, $V_o(T)$ maps out a linear, calibrated, equivalent time representation of the unknown transient, $V_{in}(t)$ (Figure II-26f).

CHAPTER III

THE EXPERIMENT

The emphasis of this chapter is placed on the design, construction and testing of all components involved in the electro-optic sampling system. The chapter begins by describing the actual configuration used for the experimental system along with the details of its construction. Next, we will discuss the calibration process for the sampling heads and detail the operating procedures involved in performing actual measurements. The following section, presents experimental results that characterize the linearity, sensitivity, and bandwidth of the various sampling heads. Additional measurements demonstrating typical applications of this system are also reported. Finally, an evaluation of the experimental noise sources and signal to noise enhancement techniques is presented.

III.A. The experimental arrangement

The experimental configuration can be divided into three major portions. The first, and crux of the system, is the collection of various electro-optic sampling heads that have been constructed. Second is the laser system used as the source of optical pulses. Lastly, we consider the electronic components and their interaction with the optical

elements.

III.A.1. The sampling heads

The electro-optic sampling head is the element which provides for the interaction between the unknown electrical transients and the optical sampling pulses. It contains the electro-optic crystal, with electrodes, mounted between high speed electrical connectors that allow for signal conduction into and out of the device. We have built four main heads, each suited to a particular measurement application. The sampling head, or modulator, with the largest bandwidth has a critical frequency of 119 GHz. As described in the theory section, we chose to use lithium tantalate as the electro-optic medium. This uniaxial crystal is well suited for this application because of its relatively large electro-optic coefficient, high index, and low static birefringence. It also exhibits a broad optical transmission bandwidth as well as good environmental stability.

The proper orientation of the crystal with respect to the optical and electrical fields is essential and is illustrated in Figure III-1. In order to employ the r_{33} and r_{13} electro-optic coefficients, we must create an electric field parallel to the 3-axis. This necessitates application of the electrodes to the faces of the crystal normal to the optic axis. The orientation of the x and y axes is not important since the optical index indicatrix is rotationally

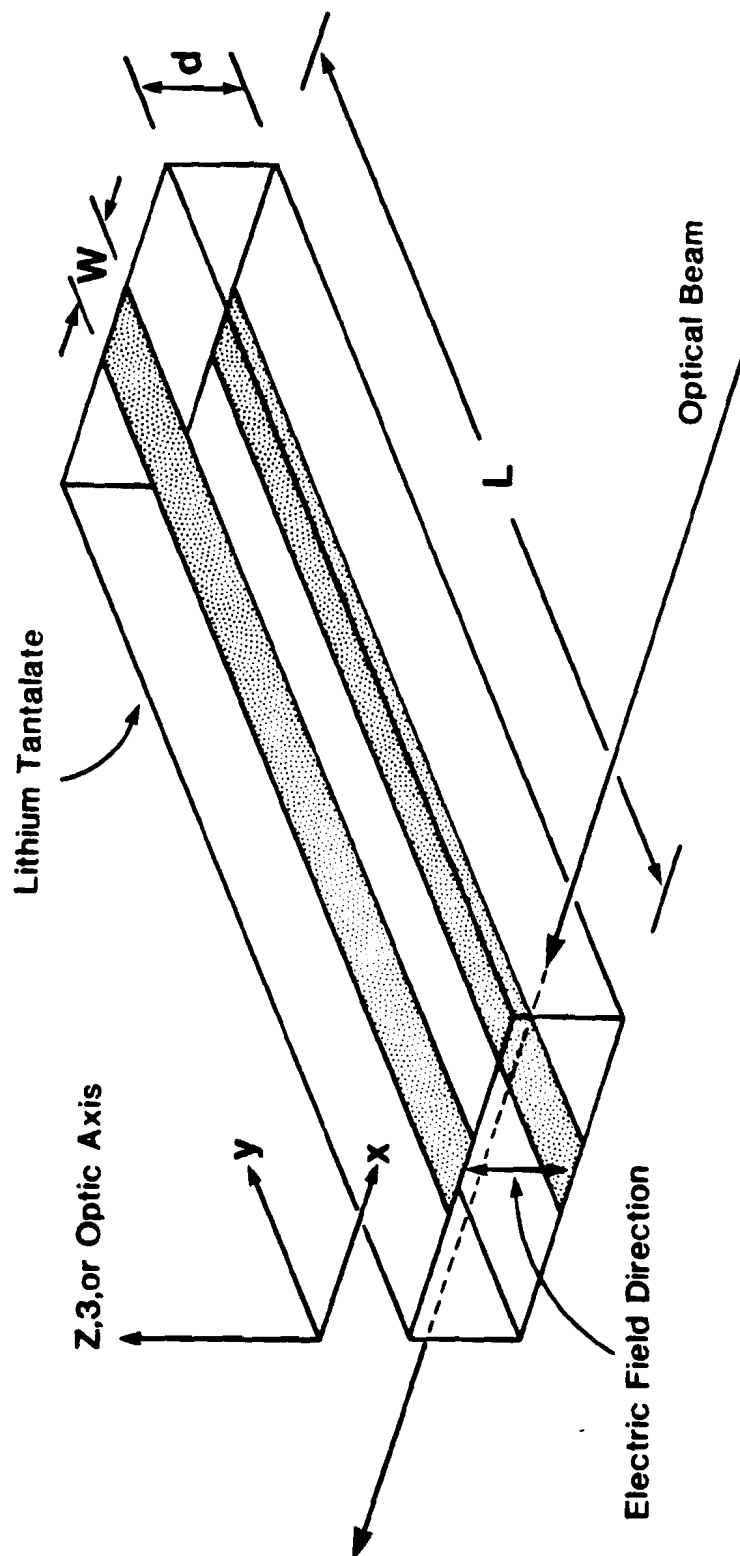


Figure III-1 Optical and electrical field orientation within the electro-optic crystal

symmetric about the optic axis. It is this very property that allows us the freedom to velocity match the sampling beam in any direction normal to the optic axis and still experience the same electro-optic effect.

All four sampling heads utilize the same crystal configuration, both in orientation and physical size, except for the thickness, d . The crystals are purchased commercially as custom orders of length $l=15$ mm, width $w=700\text{ }\mu\text{m}$, and thickness $d=500\text{ }\mu\text{m}$. The d dimension is along the optic axis. All four long faces ideally should be optically polished although the quality of the largest faces is not as critical since they have electrodes and are not used as optical surfaces. The ends of the crystal are merely cut square, and have a fine ground finish. The electrodes are of evaporated aluminum⁵⁴ approximately 3000 Angstroms thick produced by the shadow mask technique. They are placed down the center of the $0.7\text{ mm} \times 15\text{ mm}$ faces so that most of the fringing electric field will be contained within the electro-optic medium. For larger crystals used at relatively low frequencies ($<20\text{ GHz}$), it was found to be adequate to paint on thin electrodes using a high quality silver polymer laquer.⁵⁵

The supporting structure for the crystal and connectors is machined from a single piece of brass and is illustrated in Figure III-2. Since the electro-optic crystal transmis-

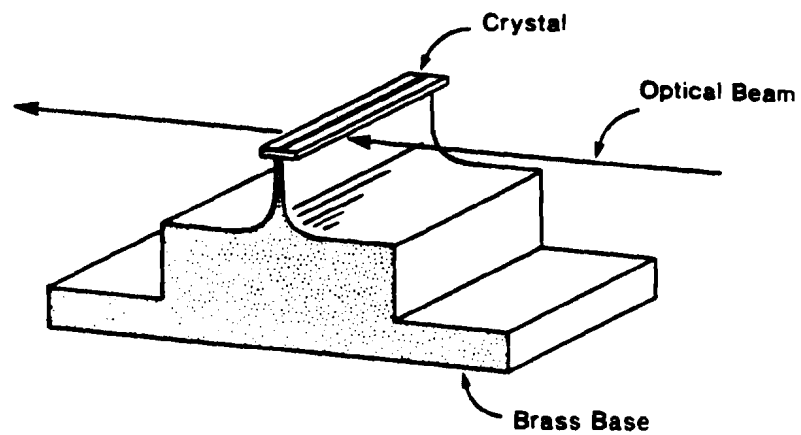


Figure III-2 The electro-optic crystal mount

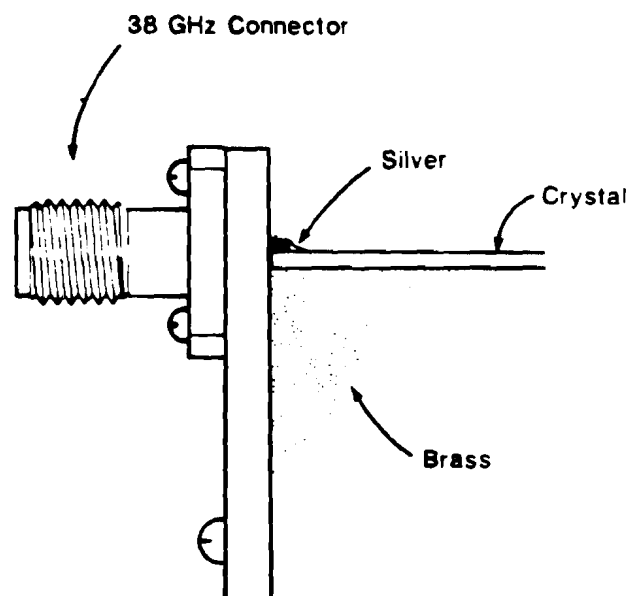


Figure III-3 Connector and crystal configuration

sion line is fabricated as a balanced stripline, it requires a matching geometry that will not alter those characteristics. This is achieved by forming the crystal mounting platform as a 15 mm long ridge that tapers up to match the width, W , of the crystal's bottom electrode. The crystal is bonded to this ridge using silver laquer. 38 GHz coaxial connectors⁵⁶ are fastened to the brass base with their center conductors attached to the crystal electrodes using the silver laquer once again (Figure III-3). This configuration provides a mechanically sturdy device that is readily connected to and that has open access for optical beams. The entire sampling head is mounted on a rotatable platform with its rotation axis parallel with the crystal optic axis to facilitate velocity matching at various angles.

Our simplest device was designed to be a sampling head that could be connected by high speed cable to an external signal source. It is depicted in Figure III-4, and consists simply of a 500 μm thick crystal between coaxial connectors. One connector supplies the signal while the other removes it to a terminated line. The maximum quasi-TEM frequency this crystal can support is 20 GHz, but dispersion effects up to the 38 GHz limit of the connectors are small. Thus, this device is useful for temporal resolutions down to approximately 10 ps. Since the optical transit time at normal incidence is only 5 ps, velocity matching is usually not employed.

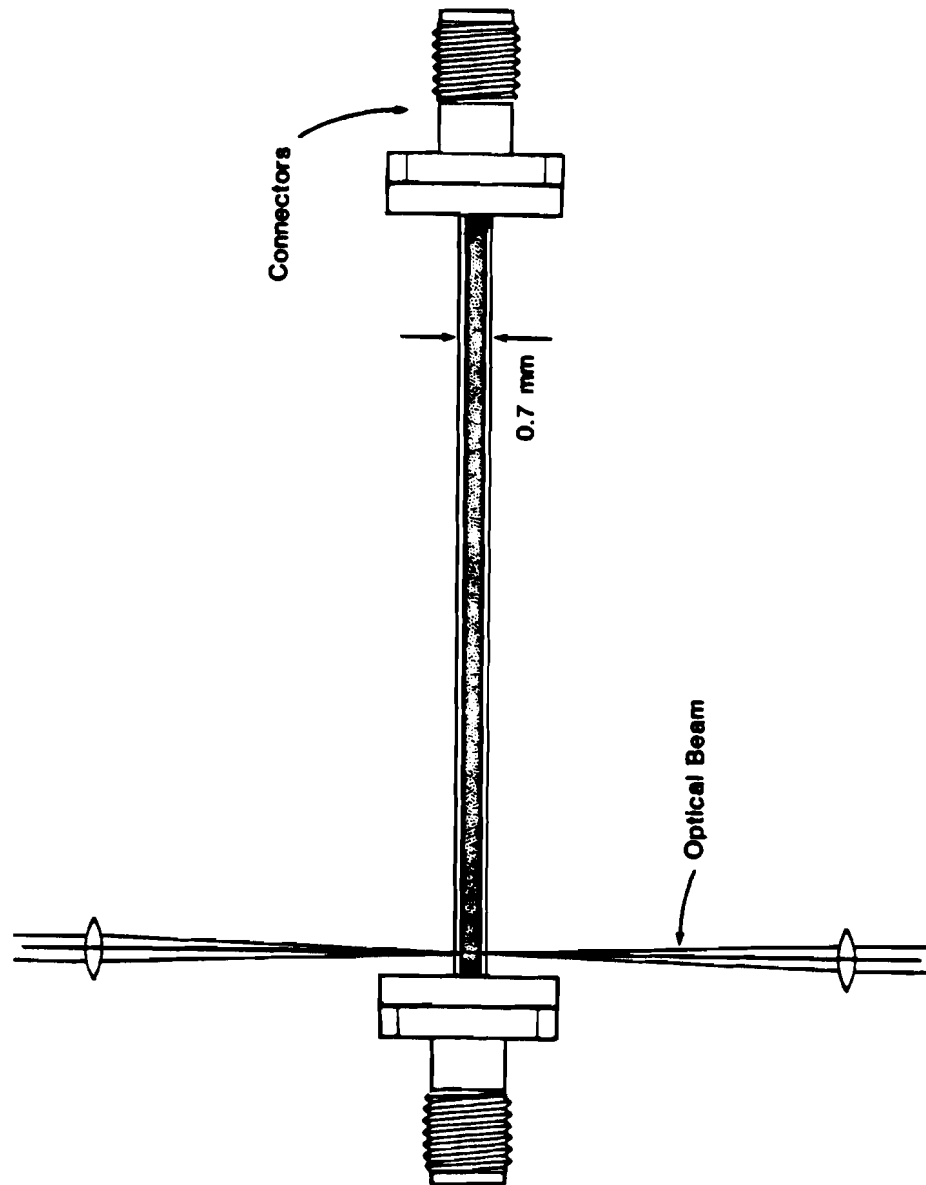


Figure III-4 Sampling head configuration for an external signal source

To achieve higher frequency response and correspondingly better temporal resolution, the connectors must be eliminated between the signal source and the electro-optic crystal. This is accomplished by fabricating a mount that enables the signal source to be placed immediately adjacent to the electro-optic crystal as depicted in Figure III-5. In this way, the source side connector can be used to provide a low frequency or DC bias, if necessary, while the remaining connector on the crystal is used as before, to extend the transmission line to the terminator. Without the intervening connectors, the frequency response of the sampler is limited only by the dispersion of the connecting striplines. We have constructed three such integrated devices with crystal thicknesses of $500\text{ }\mu\text{m}$, $250\text{ }\mu\text{m}$, and $100\text{ }\mu\text{m}$, having electrode widths of $700\text{ }\mu\text{m}$, $300\text{ }\mu\text{m}$, and $125\text{ }\mu\text{m}$ and corresponding critical frequencies of 20 GHz, 48 GHz, and 119 GHz respectively. All the crystals have relatively low impedances of about 20 ohms for TEM operation, due to a wide electrode design used to enhance the sensitivity.

III.A.2. The CPM dye laser system

The fundamental limiting element of any optical sampling process is the optical pulse itself. Since it is the gating function of the sampler, it should be well defined both in time and space. The pulse width must be less than

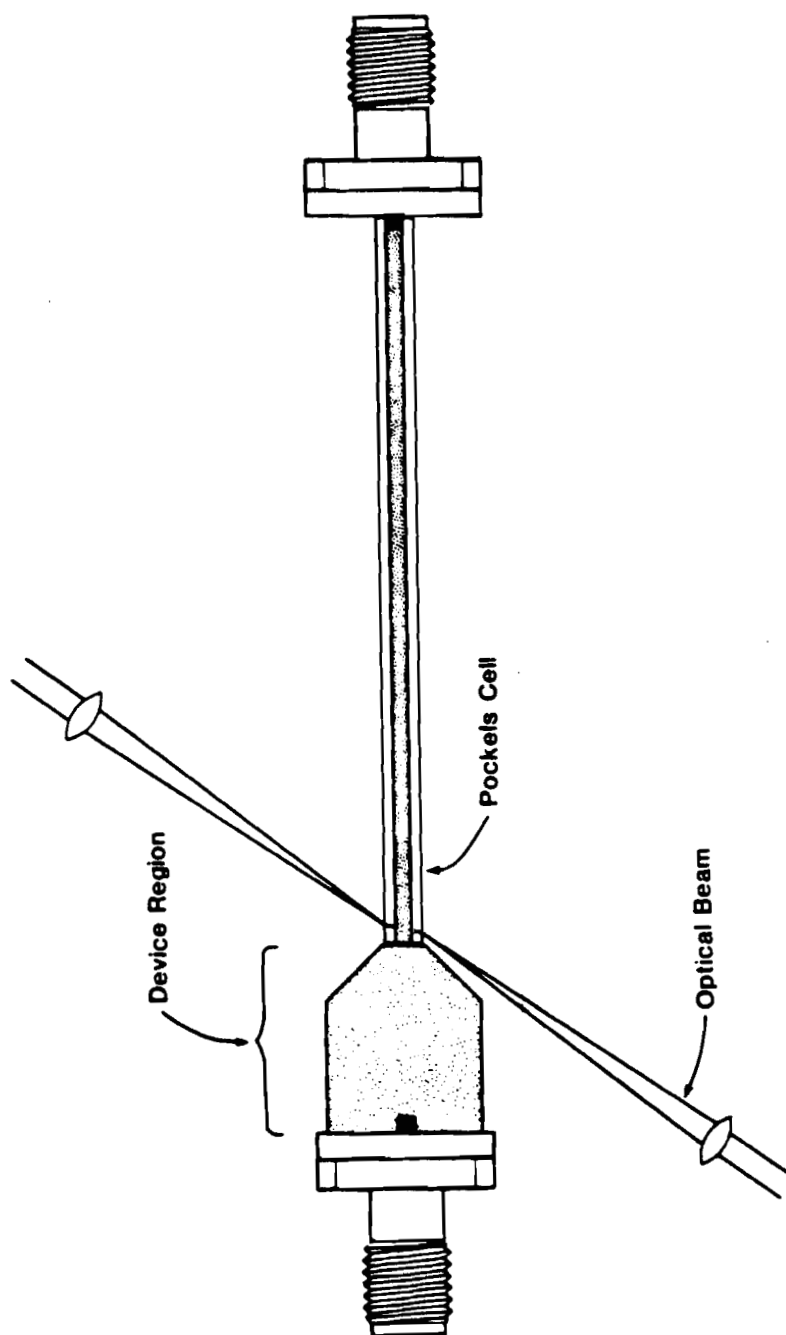


Figure III-5 Sampling head configuration for an integrated signal source

or equal to the desired resolution of the sampling system as well as being stable and reliable in both short (μ sec) and long (days) time scales. Fortunately, concurrent with the beginning of this experiment was the discovery of the colliding pulse mode-locked (CPM) dye laser system.⁵⁷⁻⁶⁰ The laser system is illustrated in Figure III-6.

The CPM laser can produce pulses of less than 100 femtoseconds with amplitude stability determined only by fluctuations in the argon pump laser (typically a few percent). It is a passively mode-locked laser similar to many others that use Rhodamine 6G (Rhodamine 590) as the gain medium and DODCI (Diethyloxa-dicarbocyanine Iodide) as the saturable absorber.⁶¹ However, where such lasers in the past used linear cavities, the CPM system utilizes a ring geometry to achieve operating characteristics far superior to any other dye laser as far as pulsewidth and stability are concerned. Crucial to this operation is the ring cavity and the use of a specially formed nozzle for the saturable absorber jet that produces a dye stream only 30 μ m thick.

The Rhodamine jet is pumped by a CW Argon laser operating on its 5145 Angstrom line with approximately 4 watts of power. The evolution of pulses in a conventional passively mode-locked laser cavity is described in the literature.⁶² Since the CPM resonator is a ring, two pulses are created, traveling in opposite directions and synchronized at the

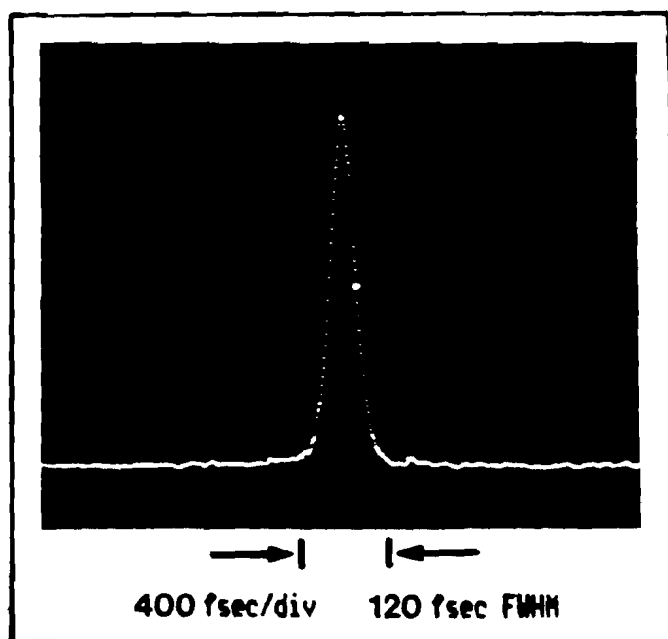
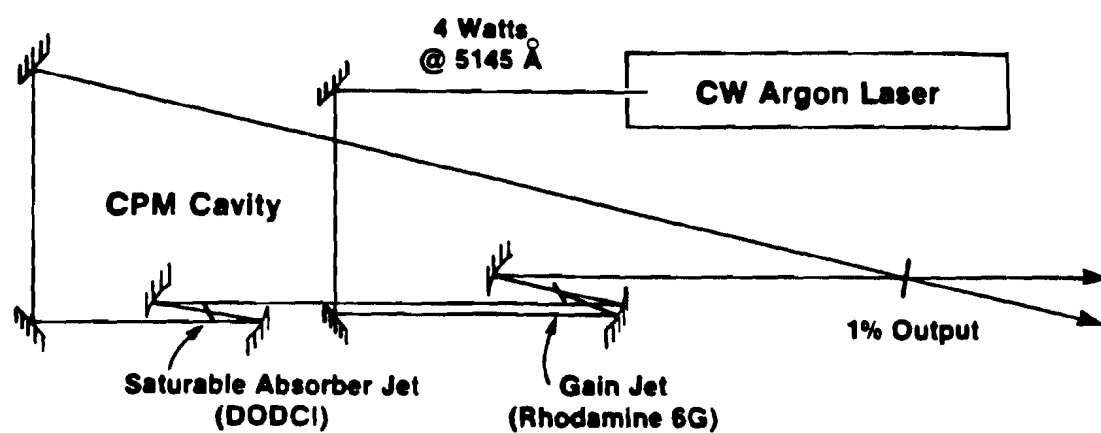


Figure III-6 Colliding pulse mode-locked laser schematic and typical auto-correlation trace

saturable absorber jet. This synchronization occurs because the minimum energy is lost to the saturable absorber when the two pulses meet at the jet. It is this self-synchronizing property coupled with the ultra-thin jet that separates this laser from the rest. Several theories have recently evolved, but it is generally believed that when the two pulses arrive at the DODCI jet they form a standing-wave absorption grating. This transient grating provides a means for the two pulses to exchange and balance their energies. The pulses also experience shortening effects due to the enhanced absorption of the jet stream at the edges of the optical pulses where the grating contrast falls off. Thus, the jet thickness is intimately related to the obtainable pulsewidth.

As with most passively mode-locked lasers, the CPM laser operates best at a single wavelength, in our case, 6200 Angstroms. Pulses of 120 fs duration are produced at a repetition rate of 91 MHz in two beams, each with an average power of 10 mW. The above output values correspond to an individual pulse energy of 0.1 nJ. Figure III-6 also shows the autocorrelation trace. More details about the autocorrelator are given in appendix B.

III.A.3. The system configuration

The entire system incorporates the CPM laser, sampling heads, optical components associated with the modulator and

delay lines, and the electronic signal processing components. A schematic of the system is illustrated in Figure III-7. Conveniently, the CPM ring laser produces two precisely synchronized output pulse trains. One beam is used to sample the induced birefringence of the modulator while the other is dedicated to the triggering of the electrical source. The sampling head is placed between two Glan-Thompson polarizers so as to convert phase modulation to intensity modulation. The polarizer axes are crossed at 90 degrees and oriented at 45 degrees to the optical axes of the lithium tantalate crystal. The extinction ratio is better than 1000:1. Both transmitted and rejected beams at the analyzer are available for measurement. Simple, plano-convex lenses are employed symmetrically about the sampling crystal in order to focus the sampling beam through the crystal and then recollimate it through the analyzer and into the detectors.

Since the electro-optic crystals are not fabricated to produce precisely one quarter wave retardation, a Soleil-Babinet variable compensator is introduced between the polarizers to optically bias the modulator at its quarter wave point. This bias point allows for linear operation with the highest sensitivity and a theoretical 50%/50% intensity split at the analyzer. Since this split is rarely perfectly realized, a variable attenuator is placed before one of the detectors to facilitate intensity matching at the

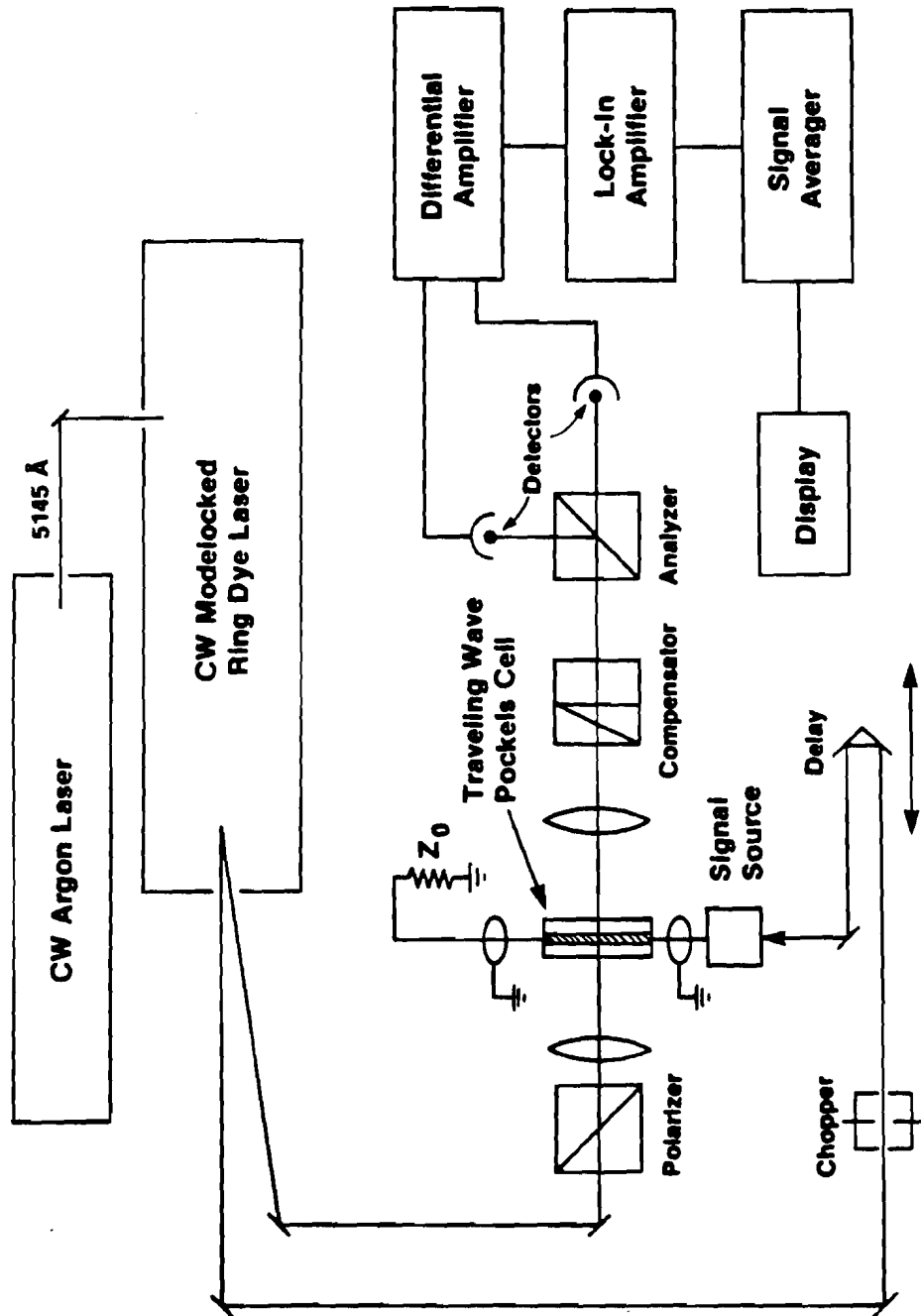


Figure III-7 The complete electro-optic sampling system

detectors.

The second beam of the laser is routed through a mechanical chopper operating at 808 Hz and a motor driven optical delay line before it is directed to trigger the electrical source. The unknown electrical signal is guided across the electro-optic cell and then terminated. The terminator can be connected to a 1 Megohm oscilloscope input to monitor the pulse train generated by the source.

The optical paths for each laser beam must be accurately measured to ensure synchronization of the electrical and optical signals at the sampling crystal. This measurement must include the delay that exists between the two pulse trains exiting the laser, because the absorber jet is not located exactly one half cavity length from the output mirror. If an external signal source is used, one must also account for the cable delay time between the source and the crystal.

The detectors are a pair of E.G.G. FND-100 PIN diodes, reverse biased with a common 90 V battery. Their biasing circuitry is shown in Figure III-8. The values for the load resistor, R_L , and the capacitor, are chosen so as to attenuate all frequencies except the chopper frequency. Since the AC component due to modulation is small, high impedance digital voltmeters are used to measure the DC intensity levels.

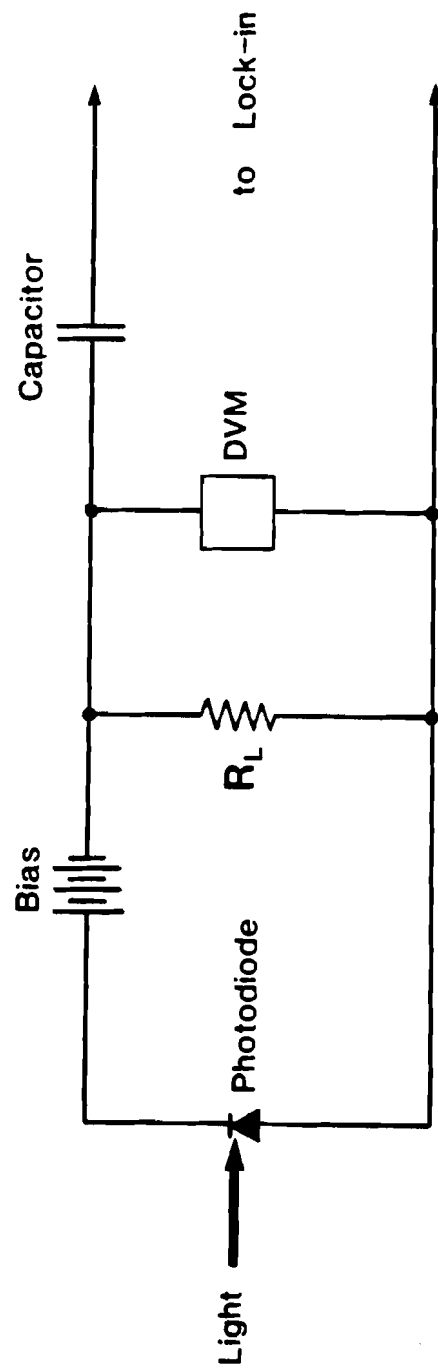


Figure III-8 Detector bias and conditioning circuitry

For a fixed relative delay between the optical and electrical signals, each of the optical sampling pulses experiences the same portion of the electrical signal and hence experiences the same degree of modulation. This process yields a DC level at the detectors with an additional modulation at the chopper frequency. Since one detector experiences a small increase from 50% while the other detector experiences an equal decrease below 50%, the differential amplifier measures twice the change of a single detector. To further enhance sensitivity, significantly, a lock-in amplifier tuned to both the chopper frequency and its phase is used to convert the AC signal at 808 Hz to an amplified DC level suitable for driving the signal averager and display screen. The signal averager is employed as a slow speed oscilloscope with the ability to digitally average successive traces.

In order to sample a portion of the unknown electrical transient, one of the laser pulse trains must be either advanced or delayed with respect to the other pulse train. This delay is accomplished by inserting a stepper motor driven optical delay line in one of the beams. The delay line consists of either a roof prism or cube corner reflector placed on a moving stage that is swept linearly in time and space. For convenience reasons we chose to insert the delay line in the electrical trigger beam. Movement of the delay line triggers the sweep of the signal averager and

display unit. With the output from the lock-in amplifier fed to the signal averager y-axis, the unknown electrical profile is mapped out on the display. Subsequent sweeps can be averaged to further increase the signal to noise ratio of the electrical signal.

III.B. Experimental operation

This section will discuss the preparation of the electro-optic sampling system before measurements can be made. Optical and electrical calibration of sensitivity, time resolution and linearity is described as based on the theory presented in section II-B. The measurement procedure is also outlined and commented upon with some cautionary notes.

III.B.1. Calibration

For a measurement system to provide accurate information, it must be calibrated. Proper calibration of both the voltage sensitivity and the temporal accuracy are important, as well as determination of the extent of the linear operating regime. Every modulator is used in a different configuration, therefore, each sampling head is individually calibrated for the particular geometry employed.

Since we use lock-in detection, the calibration signal we apply to the crystal is a sine wave of known amplitude, ΔV , at the lock-in frequency. ΔV yields an optical intensi-

ty modulation, ΔT , at the detectors. The detectors convert ΔT into an AC voltage modulation whose amplitude is measured by the differential lock-in amplifier. ΔT is a measure of the modulation depth and can be determined by dividing the peak to peak AC voltage at the detectors by the DC level. The DC photodiode voltage (PDV) is read from the digital voltmeters in the PIN diode bias circuitry. The AC component is determined by the lock-in amplifier.

The lock-in has many sensitivity scales, from 500 mV to 100 nV full scale. The scales refer to the RMS amplitude of a sinusoidal input signal at the lock-in frequency. An input signal of RMS amplitude equal to the full scale sensitivity (FSS) will yield 10 V DC at the output, V_o . Since we are interested in the actual peak voltage that appears on the crystal, we must multiply the RMS V_o by $2\sqrt{2}$. However, because we use two differential detectors, V_o is proportional to twice the actual modulation, and therefore must be halved. We obtain the following equation describing ΔT as a function of V_o :

$$\Delta T = \left(\frac{2\sqrt{2}}{2}\right) V_o \left(\frac{FSS}{10V}\right)_{PDV} = 0.141 \left(\frac{V_o}{PDV}\right) FSS. \quad \text{III-1}$$

From section II.B.2. we get the slope of the modulation function as:

$$\frac{\Delta T}{\Delta V} = \frac{1.57}{V_p}. \quad \text{III-2}$$

Combining these two equations we arrive at an equation that

determines V_{π} given ΔV :

$$V_{\pi} = 11.1 \left(\frac{\Delta V}{FSS} \right) \left(\frac{PDV}{V_0} \right) \quad \text{III-3}$$

Once V_{π} is determined, an unknown ΔV can be calculated with experimentally measured values by using the following equation:

$$\Delta V = 0.09 \left(V_{\pi} \cdot FSS \right) \frac{V_0}{PDV} \quad \text{III-4}$$

Given this method of determining V_{π} for a particular Pockels cell geometry of known electrode width, W , and separation, d , one can determine V_{π}^* (for the material alone) using the following relation:

$$V_{\pi}^* = V_{\pi} \frac{W}{d} \quad \text{III-5}$$

The values of V_{π} measured by the above technique at 1 kHz, are those of a "free" crystal below the acoustic resonances of lithium tantalate. As described in the theory section, the electro-optic coefficients for a free crystal are denoted by the letter T . Consequently we write the experimentally determined halfwave voltage as V_{π}^T . Above acoustic resonances the crystal is referred to as clamped and is characterized by the S electro-optic coefficients. We have determined V_{π}^{*T} for two crystals in similar geometries. Each was 500 μm thick with silver electrodes the full width of the crystal, 700 μm . We measured halfwave voltages, V_{π} , of 2015 V and 2050 V. This corresponds to an average V_{π}^* value of 2840 V. This is about 6% higher than

the calculated V_{π}^* using published values of r_{33} and r_{13} (sect II.B.3.). It should be noted that the published values are typically accurate to only $\pm 15\%$.

Picosecond electrical signals are in the radio frequency (RF) regime and hence the S coefficients apply. Published S electro-optic coefficients give rise to a halfwave voltage that is approximately 5% lower than for the T coefficients. We calculate our experimental halfwave voltages in the RF regime by decreasing the measured T values for our crystals by 5%. The appropriately adjusted RF halfwave voltages for our sampling heads are listed in Table III-1.

Sampling Head	V (T)	V (S)
500 μm ext.	2015 V	1915 V
500 μm int.	2050	1950
250 μm int. (A)	1600	1520
100 μm int. (B)	1570	1490

ext. = external source
int. = integrated source

TABLE III-1 Sampling head halfwave voltages.

One must also be aware that the signal measured by the lock-in amplifier is only the amplitude of the sinusoidal component at the fundamental frequency. The use, for instance, of square-wave modulation of the signal source as encountered when chopping the trigger beam broadens the frequency spectrum of the modulated beam. From the Fourier

series expansion of a square wave, it is found that the amplitude of the fundamental frequency is 27% higher than the square wave amplitude. Thus, the lock-in output is higher by the same amount and hence must be compensated for in the calculation of V . In the interest of utmost accuracy, the output should be calibrated with the same waveform that will be used in the actual measurement situation.

As discussed in the theory section (II.B.2.), the linearity of response is determined by the linearity of the \sin^2 modulation function. When biased at the quarter-wave point, the response is linear to within 1% for ± 0.25 radians of phase retardance, or $V/V = \pm 0.08$. For an average V of 2000 V this corresponds to a regime of ± 160 V. It is doubtful whether this range capability will ever be necessary. Just in case, 5% error occurs at ± 360 V.

Temporal calibration is achieved by accurately gauging the speed of the stepper motor driving the optical delay line. The motor control electronics generate a stable square wave whose transitions trigger the motor to rotate through a precise angular step. The pitch of the lead screw then determines the translation distance per step. By monitoring the frequency of the drive signal with a frequency counter, the translation speed is ascertained. The speed of the translation stage, S_t ($\mu\text{m}/\text{sec}$), is precisely related to the changing optical delay, S_o (ps/sec), by the speed of

light, c . Since the delay line is optically double passed, the optical delay is actually twice the stage movement. The speeds are related by the following equation:

$$S_0 = \frac{2S_t}{c} \quad \text{III-6}$$

where $c = (300 \mu\text{m/ps})$. The speed accuracy of the translation stage is controlled by motor driver electronics which are typically accurate to $\pm 1\%$. The signal averager sweeps at a constant time per division, typically an integer number of s/div. Multiplying this by S_0 yields a final time scale of picoseconds per division.

III.B.2. Measurement procedure

A fairly straight-forward procedure for making measurements with the electro-optic system can be described. This section will outline the basic procedure for characterizing unknown signals in a step by step process. It is assumed that the appropriate sampling head for the bandwidth of interest and configuration has been chosen and the delay times for both trigger and sampling arms have been suitably adjusted for synchronization.

The measurement procedure is as follows:

1. Place the crystal in the focal region of the sampling beam and adjust it for proper angle and spatial position. The sampling beam should pass

undistorted. Fix the crystal in place.

2. Connect and adjust the electrical source for an appropriate signal by monitoring the signal at the terminator.
3. Direct the modulator beams into the detectors and monitor the DC voltage levels.
4. Adjust the compensator to find adjacent minimum intensity positions for each detector. Set the compensator at the midpoint. This is the quarter-wave point.
5. Adjust the intensities at the detectors to be equal using fixed filters and the variable attenuator.
6. With the bias modulation on at the lock-in frequency, and the time constant set at 10 ms, minimize noise fluctuations in the lock-in output by further balancing the detector intensities.
7. Return the time constant to 100-300 ms and scan the delay line to find the signal. Adjust the lock-in sensitivity suitably. Stop and zero the delay line at a position that enables sampling before onset of the signal.
8. Adjust the signal averager sensitivity and enable

the signal averager for external triggering by the delay line driver.

9. Begin the delay sweep (signal averager should be triggered). As the sweep advances, the sampling point should move to later times in the electrical profile. Thus, the display trace should have time advancing properly from left to right.
10. At the end of the sweep, return the delay line to the zero position. Repeat sweeps with averaging if necessary.

The above procedure, admittedly superficial, describes the basic elements of the sampling process. Clearly, not all special situations can be documented and therefore common sense reigns above all. Some common problems have been encountered and should be noted.

One should be careful to monitor the amplitude of the electrical pulse train while scanning. If the delay line is not accurately aligned, the signal level will vary with delay position thus distorting the acquired trace. It is also important to note that there is a trade off involved between the signal to noise ratio (S/N) of the acquired signal and the bandwidth of the lock-in response. The trade-off is controlled mostly by the time constant (TC) setting. Increasing TC increases the S/N by narrowing the

lock-in bandwidth. The narrow bandwidth, in turn, limits the response time of the output signal, V_o . Thus, one must be cautious not to scan so fast that the TC limits the observed risetime and other temporal characteristics. Given an electrical step function faster than TC, V_o will reach 95% of its final value in approximately 5 TC's.⁵¹ Figure III-9 shows the fastest risetime observable for several combinations of typical TC's and scanning speeds. Thus, to scan faster one must be able to tolerate a lower S/N and employ repetitive scanning and averaging. Increasing TC will produce a single trace of better S/N, but one must scan slower to avoid distortion. Regardless of the approach taken, the total signal acquisition time to attain a given S/N will be comparable.

III.C. Experimental results

This section presents experimental results that can be divided into three main parts. The first part will describe measurements that pertain only to the operation of the sampling system. The system's basic characteristics (excluding bandwidth) as an instrument for signal analysis will be demonstrated. The second part explicitly describes bandwidth considerations, and will elaborate on the evolution of the unprecedented bandwidth that enables subpicosecond resolution. The last part presents a representative collection of applications that demonstrates

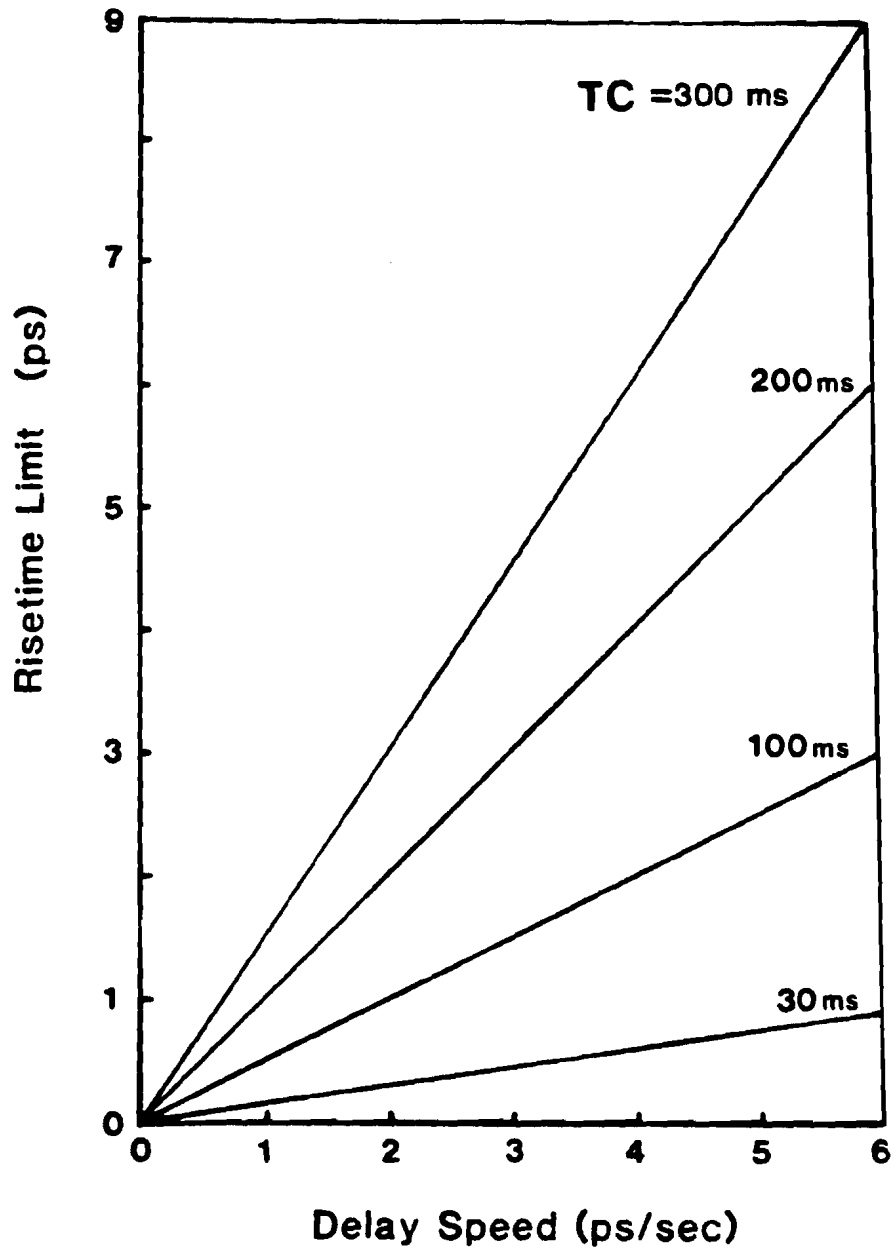


Figure III-9

Risetime limit as a function of delay line speed
and lock-in amplifier time constant

the system's capabilities.

III.C.1. Basic system characteristics

III.C.1.a. Linearity

By operating the modulator at its quarter-wave point, the output signal, V_o , is a sine function of the voltage applied to the electro-optic crystal. As stated before, for a Pockels cell with halfwave voltage of 2000 V the response should be linear within 1% for ± 160 V. We never encounter signals larger than 10 V (rms) and hence demonstrate linearity in this regime only. Figure III-10 shows the response curve for the $500\text{ }\mu\text{m}$ multipurpose sampling head given a 808 Hz sine wave signal of various amplitudes. The response is demonstrated to be linear within an experimental error of $\pm 1\%$.

III.C.1.b. Sensitivity

We measured the voltage sensitivity using two methods. The first method employed characterization of an actual picosecond transient signal while the second method measured the noise level using a pure sine wave at the lock-in frequency. Both techniques produced comparable noise level amplitudes for a given integration time. Noise levels were typically about one millivolt per root Hertz ($1\text{ mV}/\sqrt{\text{Hz}}$).

Figure III-11 shows a typical trace obtained from the

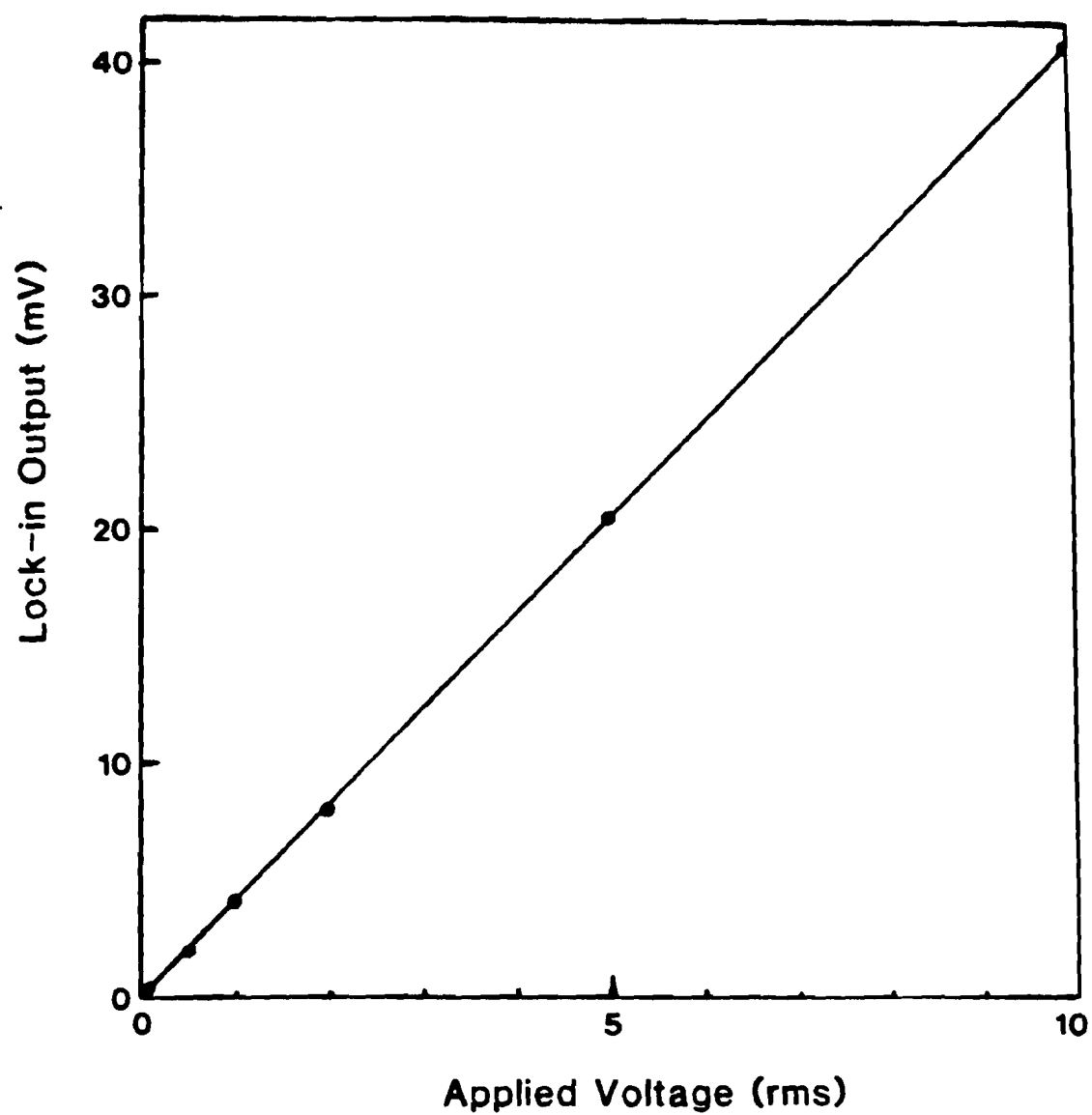


Figure III-10
Demonstration of modulator response linearity

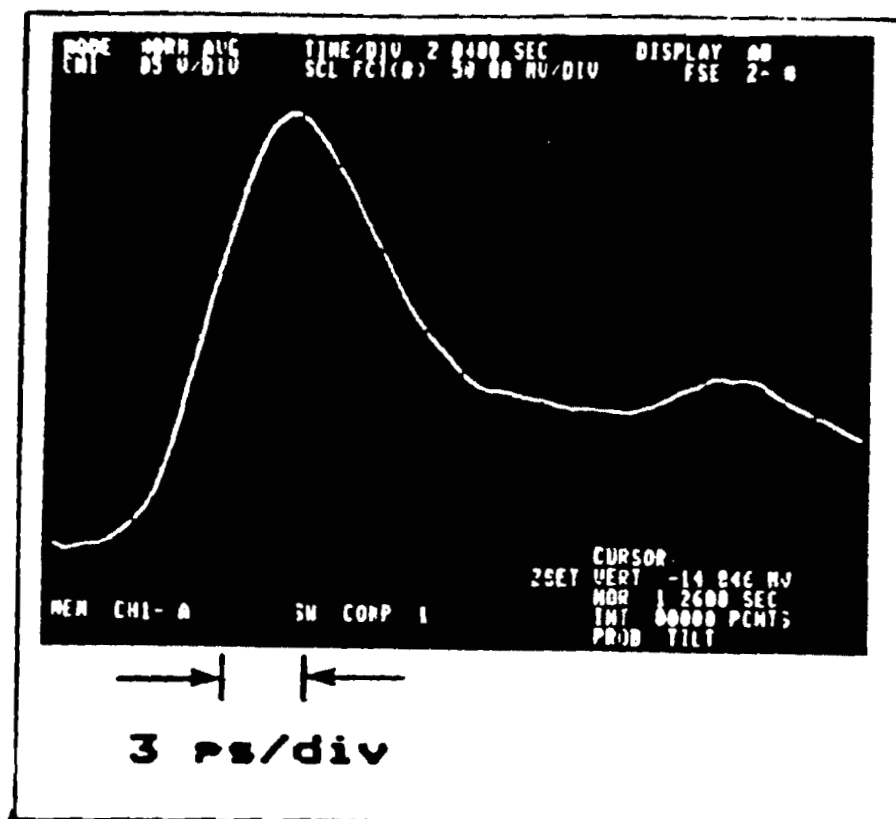


Figure III-11

Typical system output trace
 (sampled response of a Cr:doped GaAs photoconductive
 detector triggered by a 120 fs optical pulse)

electro-optic sampling system. It depicts the photoconductive signal obtained from a Cr:GaAs detector with a $20\text{ }\mu\text{m}$ gap when integrated with the $250\text{ }\mu\text{m}$ crystal sampling head. The risetime, τ , is 4.0 ps and the amplitude is 60 mV as calculated from equation III-4. The second bump arises from a stripline impedance discontinuity. The lock-in amplifier time constant (TC) was 300 ms (bandwidth of 0.42 Hz) and the total acquisition time was 20 s for the single sweep trace. It can be seen that the noise level is less than one half trace width for this curve which corresponds to a signal to noise ratio (S/N) of about 80:1 and hence a voltage sensitivity of less than $1\text{ mV}/\sqrt{0.42\text{ Hz}} = 1\text{ mV}/0.65\sqrt{\text{Hz}}$. Subsequent sweeps with the signal averager can reduce the noise level to near $100\text{ }\mu\text{V}$.

The sensitivity can also be measured by applying a sine wave of known amplitude to the same crystal while observing the real time S/N. In this case, the integration time is determined by the TC. For TC=300 ms, a one millivolt peak-to-peak signal produced a S/N of between one and two, and hence a noise level of approximately $1\text{ mV}/\sqrt{\text{Hz}}$, in good agreement with the transient measurement.

Since the sensitivity is fundamentally limited by the presence of laser noise at the lock-in frequency, the S/N is a strong function of the amount of signal averaging that is performed. The integration time necessary to achieve a

given S/N depends on scanning speed, scan length, time constant (ie. lock-in amplifier bandwidth), and the resolution required. Typical times range from 5 seconds to several minutes. For our applications we found that a sensitivity level of less than one millivolt was usually adequate. The noise level could be further reduced by operating with an RF lock-in frequency near 10 MHz. In this regime, additional noise peculiar to the argon laser system falls off significantly⁷⁷ and one can achieve sensitivities of less than $50 \mu\text{V}/\sqrt{\text{Hz}}$.⁶³ A voltage of $100 \mu\text{V}$ is less than 10^{-8} of the halfwave voltage and induces birefringence changes of less than 10^{-10} in the electro-optic crystal.

III.C.1.c. Stability and time constant effects

For signal averaging to be effectively employed, the reproducibility of any trace from sweep to sweep must be exact, except for random noise. The reproducibility implies that the electrical and optical signal synchronization must be jitter-free. Figure III-12 shows two successive traces overlapped for comparison. It is seen that the two curves are reproduced exactly, except for noise, to within a tracewidth. Such accuracy corresponds to a timing precision of better than 100 fs, and is proof of the system's stability. Reproducibility can also be visualized by introducing a small delay in one arm of the sampling system. Figure III-13 shows the delay incurred by translating the crystal

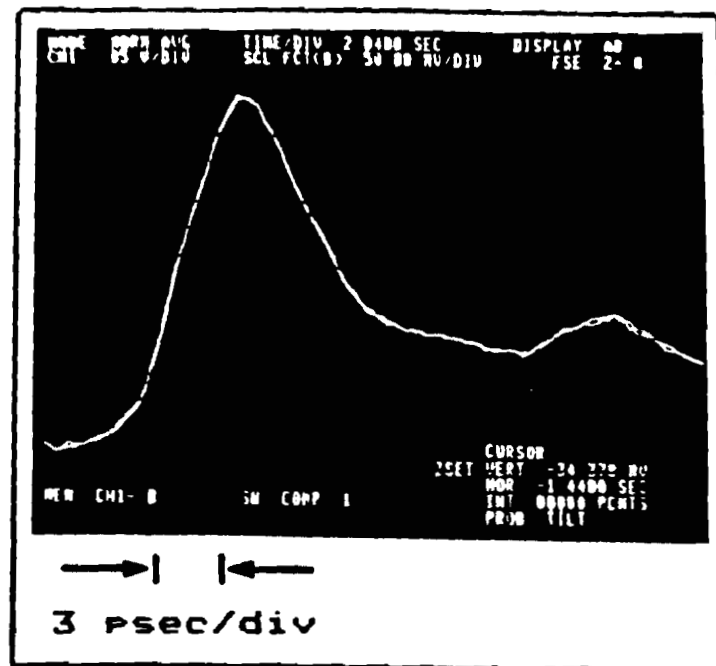


Figure III-12 Demonstration of system stability
(Two consecutively scanned traces, overlayed)

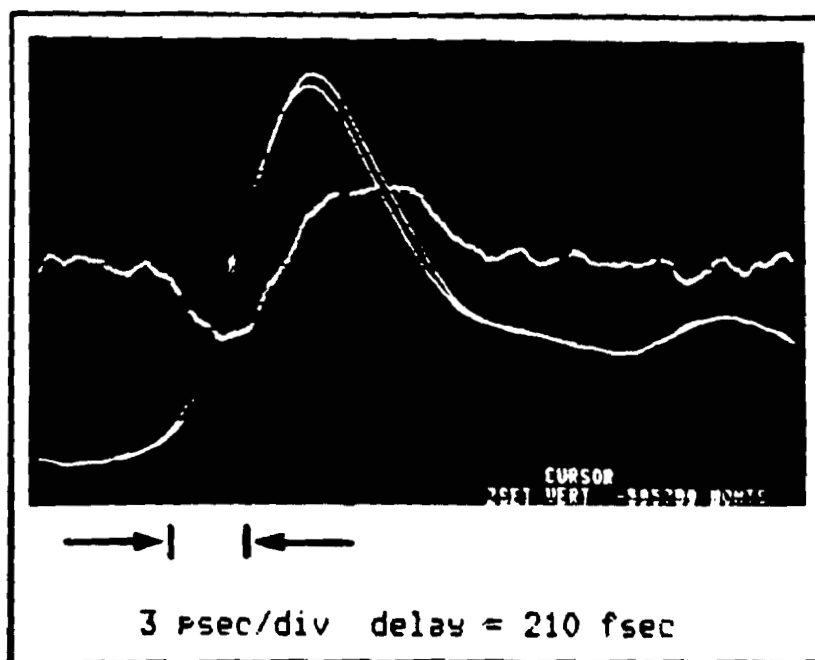


Figure III-13 Measurement of a 210 fs delay

in a direction parallel to its electrodes by $10\text{ }\mu\text{m}$ between measurements. The temporal shift is measured to be 210 fs. Movement of the crystal allows the direct visualization of a delay without upsetting the triggering of the optical delay line.

As mentioned in section III.B.2., one must be careful not to exceed the bandwidth of the lock-in while scanning a signal. The lock-in bandwidth is predominantly controlled by the TC setting. Figure III-14 shows the signal obtained as a function of TC. It is seen that for larger TC's the bandwidth is not adequate to fully resolve the risetime of the transient at that particular scanning speed. To use larger TC's, thereby increasing S/N, one must scan slower, and vice versa.

III.C.2. Bandwidth

As mentioned before, the main thrust behind employing optical methods for electrical signal measurement is the attainment of temporal resolution heretofore unachievable by other means. Subpicosecond temporal resolution measurement capability represents the foremost contribution of this thesis work. Several factors play significant roles in the determination of the overall sampling bandwidth. The factors are: sampling beam location within the crystal aperture, incident angle, waist size, and the crystal thickness. Each of these factors has been experimentally

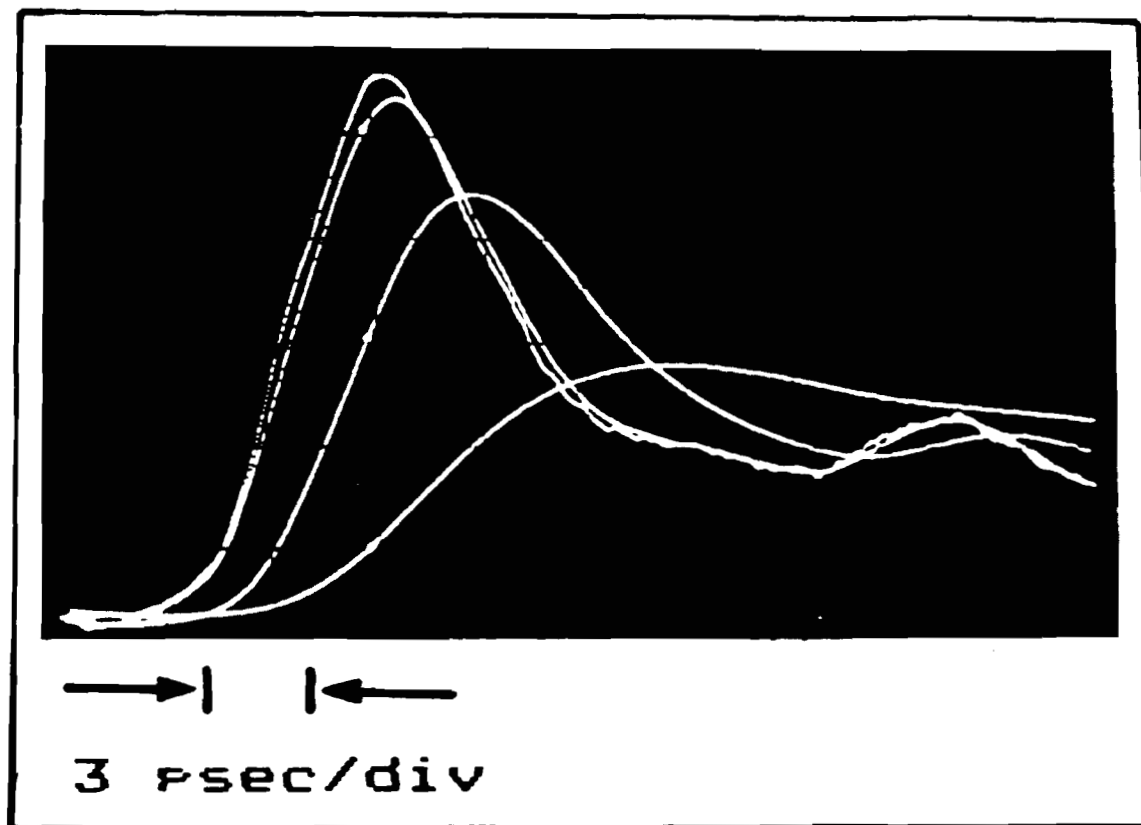


Figure III-14 Demonstration of risetime as a function
of time constant, TC

TC = 100 ms, 300 ms, 1 s, 3 s

analyzed and optimized. The culmination of the optimization has been the attainment of a temporal resolution of less than one picosecond, corresponding to a bandwidth of nearly one terahertz.

In order to test the temporal response of a measurement system, one usually generates an input signal that is known to be faster than the anticipated system response. The input signal is subsequently compared to the output signal. Changes incurred are interpreted as the system response. We have a situation that is not so conventional. We are attempting to test the ultimate temporal resolution of a measurement system that is currently the fastest available. Thus, it is impossible to verify the existence of a test signal that is faster than the resolution of our current measurement scheme. Bearing this complication in mind we have developed a test configuration that enables us to determine the "worst case" resolution limit.

Previous work (see Appendix B) has shown that photoconductive switches and detectors can respond as quickly as the applied optical excitation pulse. This response implies that electrical risetimes on the order of the optical pulsewidth can be generated. Based on this fact, such a detector should be able to generate a subpicosecond electrical risetime when operated in a suitable electrode geometry and triggered by a 100 fs optical pulse. The rise-

time we observe by sampling the transient generated in this manner is a convolution of the photoconductive signal and the gating time of the sampling system. Hence, the resolution of the optical sampling process must be at least as short as the observed risetime. It is upon the above argument that our resolution figures are based.

The microstrip electrode geometry employed in the sampling head plays a significant role in affecting the electrical signal generated by the photoconductive detector. The largest effects arise as a function of substrate thickness (electrode separation). This dimension determines the maximum frequency at which electrical signals will propagate exclusively in the quasi-TEM mode. Frequencies above this cut-off point can travel as higher order modes. Higher order modes can experience enhanced velocity dispersion and can also propagate as TE or TM waves.

Since the detector is capable of generating extremely large bandwidth signals when triggered by 120 fs optical pulses, high order mode effects are actually realized. Figure III-15 depicts the geometry used in most of these experiments. In this geometry, it is possible for TM waves to propagate at an angle such that a portion of the electrical signal reflects off the ground plane and arrives at the sampling point delayed with respect to the arrival of the "direct" TEM wave. The combination of these two waves can

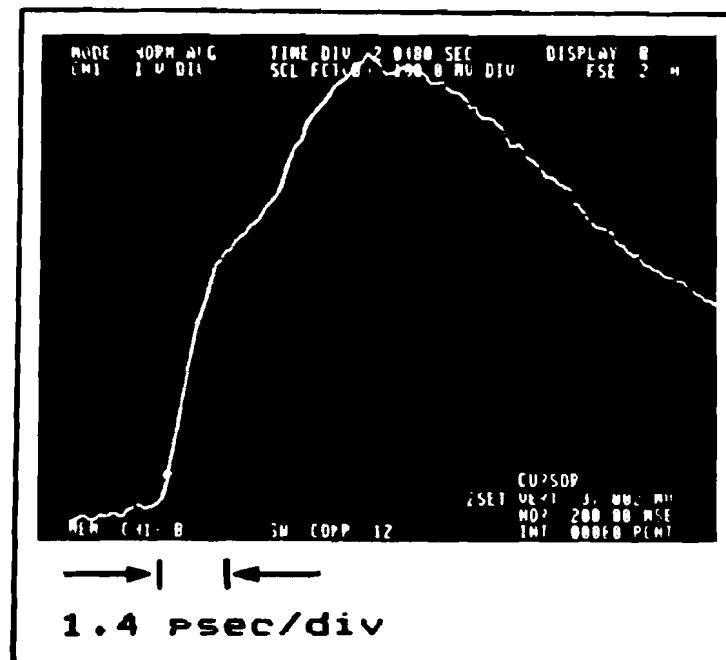
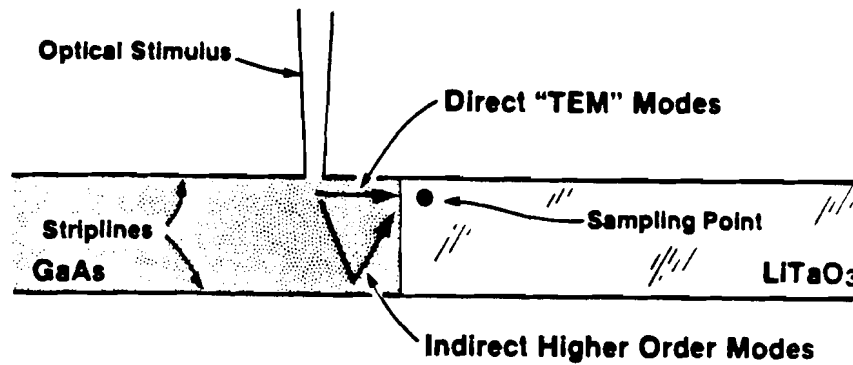


Figure III-15

Demonstration of the ability to time-resolve direct and indirect (reflected) modes

result in the generation of a segmented risetime. Such a signal, however, can still provide information indicative of the sampling resolution.

For example, consider the trace in Figure III-15 generated by a GaAs detector and sampled with the $250\text{ }\mu\text{m}$ integrated electro-optic crystal. The initial risetime (10%-90%) is 850 fs while the overall risetime is 3.1 ps. The ability of the sampling system to resolve the initial steep rise with no slow leading edge, or foot, necessitates, from convolution theory, that the sampling gate function has a temporal duration at least as short as the risetime of the initial step. This conclusion is the basis for analyzing the following results. Before demonstrating the effects of crystal thickness and non-TEM propagation, we will present results that indicate the existence of an optimum location and orientation of the sampling beam within the crystal aperture.

Figure III-16 depicts the variety of possible sampling beam geometries. Using the aforementioned $250\text{ }\mu\text{m}$ detector and crystal configuration, we will show that the best performance is achieved by employing the beam in position #1. This results in the curve of Figure III-16-1, just described.

Theory predicts these striplines to be quite dispersive for the frequencies capable of being generated by the photo-

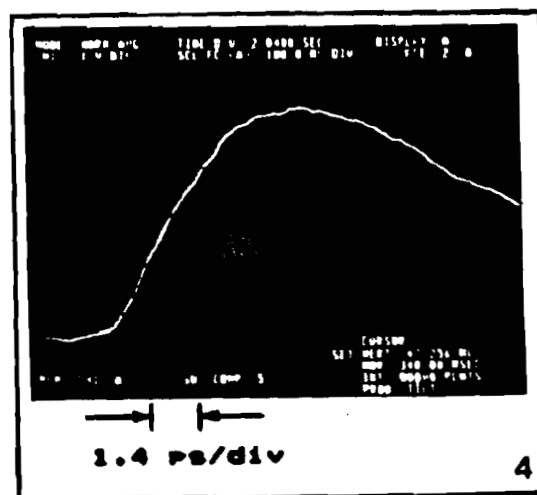
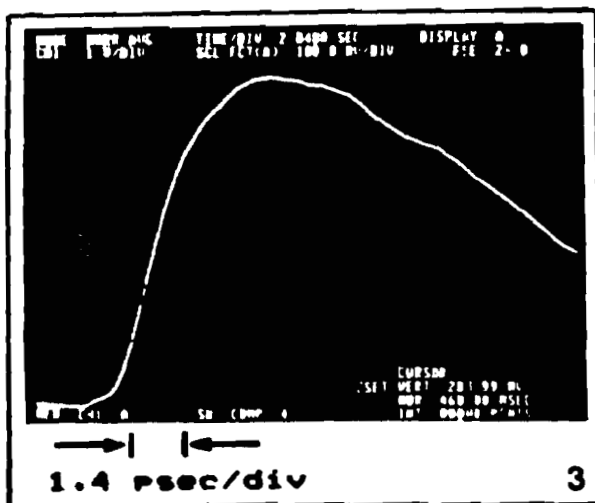
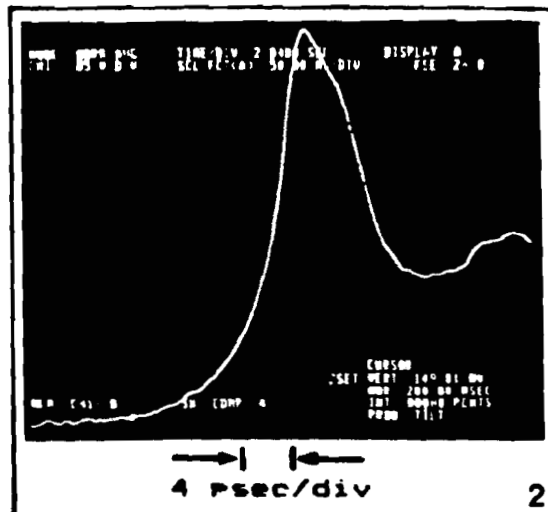
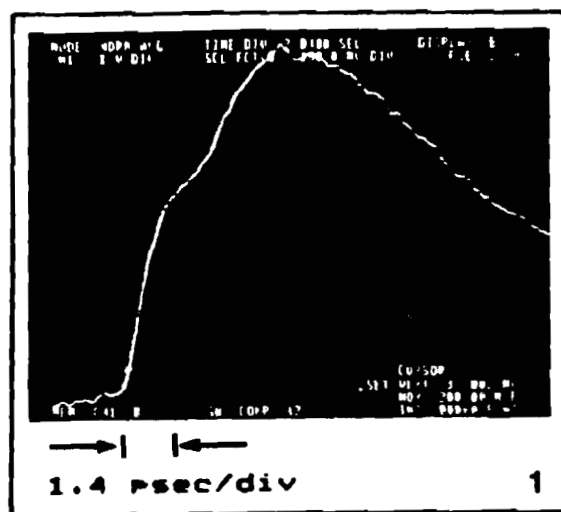
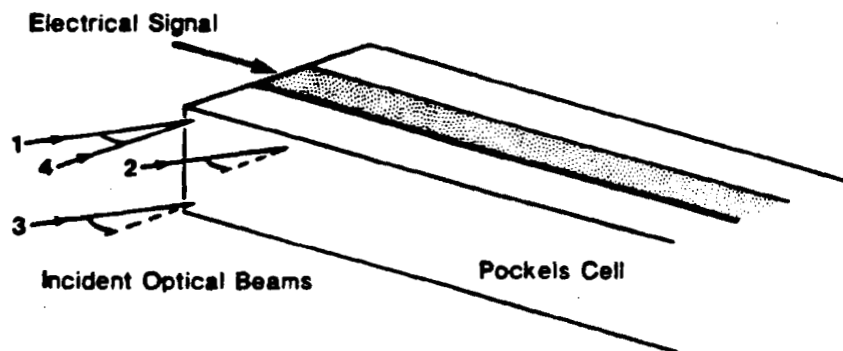


Figure III-16

Demonstration of the effects of optical beam position and orientation.

conductive detector. We can demonstrate the dispersion by sampling the same signal after it has propagated a small distance along the Pockels cell line (position #2 in Figure III-16). Figure III-16-2 shows the signal after only 1.2 mm of propagation away from position #1. The direct TEM wave is no longer resolved and the overall risetime has more than doubled to 7 ps. The dispersive property of the stripline will be elaborated upon in the next section. To avoid the effects of dispersion, it is crucial to have the sampling point as close to the source as possible.

Beam position in the vertical dimension must also be considered. Figure III-16-3 shows the trace resulting from sampling near the bottom electrode of the electro-optic crystal as depicted in position #3 of Figure III-16. Here again, the initial ultrafast TEM wave is unresolved and the risetime is lengthened to 2.4 ps. It is believed that the inferior temporal resolution in this position is also due to dispersion of the electrical wavefront. Performance at intermediate positions also leads to the conclusion that position #1 is optimum.

The third variable encountered is the angle of incidence of the optical beam. As predicted in the theory, we expect an angle of near 40 degrees (velocity matched) to provide the best temporal performance for this device. By measuring the risetimes for a variety of incident angles,

from normal incidence to 60 degrees, we found that the optimum was indeed near 40 degrees. As an example, Figure III-16-4 shows the trace resulting from sampling at normal incidence as illustrated in position #4 of Figure III-16. Once again, the direct TEM wave is unresolved and the trace has an overall risetime of 3.4 ps in close agreement with the theoretical prediction of 3.3 ps represented in Figure II-22b.

Thus, we observe the best temporal resolution by sampling at the velocity match angle as close as possible to the signal source, both vertically and horizontally. We will now present results demonstrating how waist size and crystal thickness further contribute to the ultimate resolution of the system. It will become clear that the resolution is determined mainly by the waist size while the presence of higher order modes (non-TEM) is controlled predominantly by the electrode separation (crystal thickness).

Figure III-17 presents a progression of traces resulting from using ever decreasing waist sizes and crystal thicknesses. In all cases the detector is the same GaAs photoconductive device integrated with the electro-optic crystal. Figure III-17a shows the trace resulting from the 500 μm crystal sampling head. The sampling beam waist size was about 110 μm . The initial risetime of 2.4 ps corresponds well with the theoretical limit of 2.5 ps for such

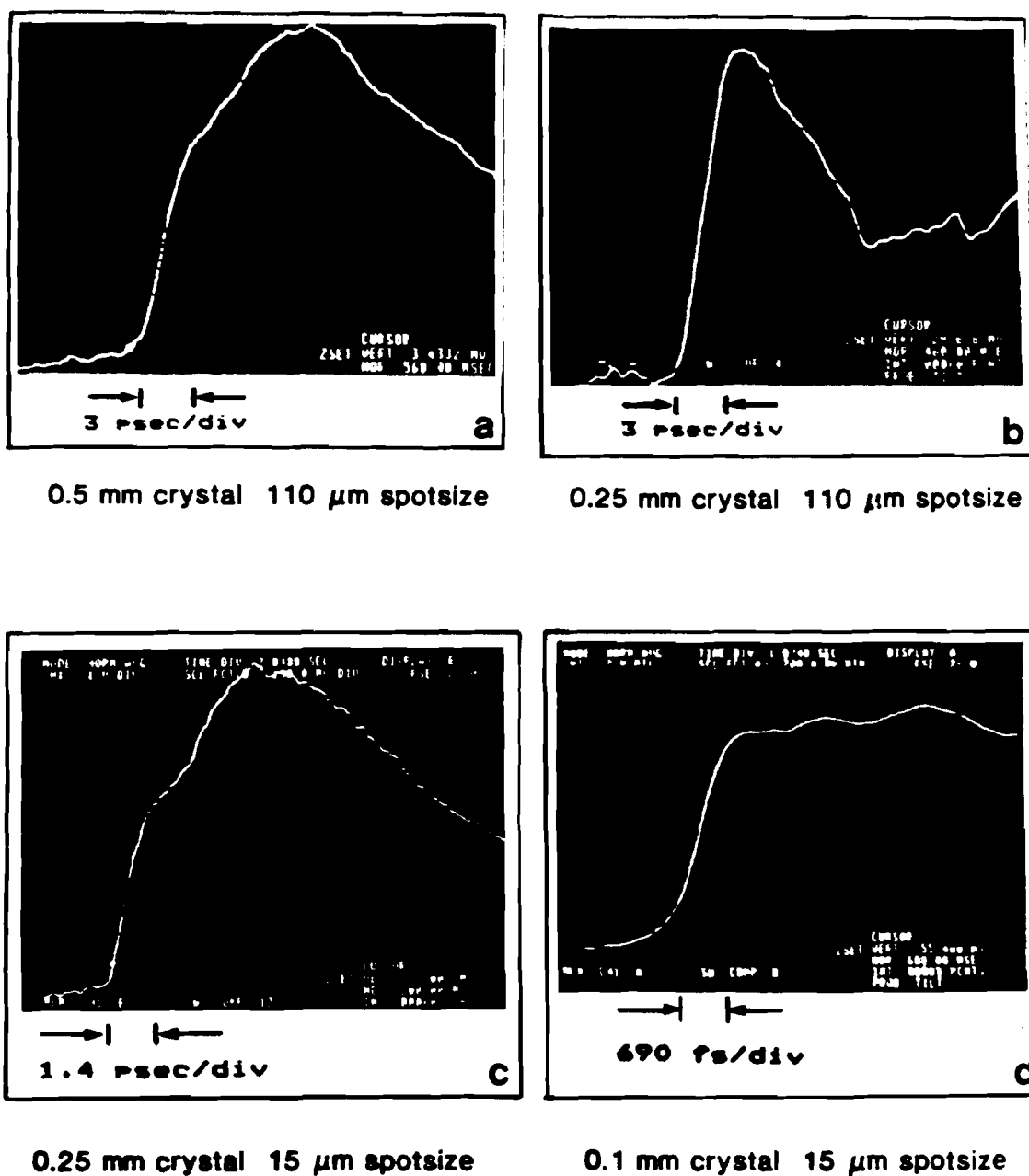


Figure III-17

Demonstration of the effects of crystal thickness and optical beam spot size

a waist size. The second peak, delayed from the first by 6 ps, agrees with that of a higher order wave reflected from the ground plane electrode.

By reducing the crystal thickness to 250 μm , with the same waist size, we achieve the result in Figure III-17b. As expected, the resolution, in this case 2.6 ps, has remained the same, while higher order modes are now unresolvable. The next step is to reduce the waist size. By employing 14 mm focal length lenses, we realize a waist size of 15 μm within the crystal, and a theoretical resolution limit of close to 500 fs. Figure III-17c depicts the transient generated in this situation. By having increased the resolution, we can again resolve the two components in the signal, while the overall risetime has remained near 3 ps due to the crystal thickness. Again the delay of 2.3 ps between first and second peaks agrees very well with that of the ground plane reflection. The initial risetime of 850 fs is somewhat above the theoretical limit, but this will be discussed in more detail later.

Clearly, the next step was to reduce the thickness again. Figure III-17d shows the trace arising from a detector and crystal with thickness of only 100 μm . The photoconductive gap was 25 μm from the end of the lithium tantalate crystal and the sampling point was 150 μm from the gap. As predicted, the initial risetime is still 850 fs due

to the same 15 μm waist size. However, the non-TEM modes have once again been considerably suppressed. The two secondary peaks correspond extremely well with small higher order components that are singly and doubly reflected by the guiding electrodes as depicted in Figure III-18. The presence of the peaks is not surprising as the frequencies present (exceeding 500 GHz) are well above the cutoff frequency for quasi-TEM propagation in this structure (~ 120 GHz).

By bringing the sampling beam even closer to the detector gap (125 μm), it was possible to generate and measure the signal shown in the trace of Figure III-19. In this geometry, the details of the rising edge become more apparent, although the risetime is still 850 fs. The base and peak of the step are not symmetrical as they would be if the measurement resolution were limited by the sampling gate width. As will be seen in section III.C.3. the slow "foot" of the risetime followed by a steeper slope to the peak is a clear indication of dispersion.

Figure III-19 also illustrates the centered electrode geometry of the 100 μm crystal. Due to the electrode placement, the optical beam's angle of incidence dictates that the electrical signal will have traveled approximately 100 μm before it intercepts the optical sampling beam. We believe that this extra 100 μm of travel is responsible for

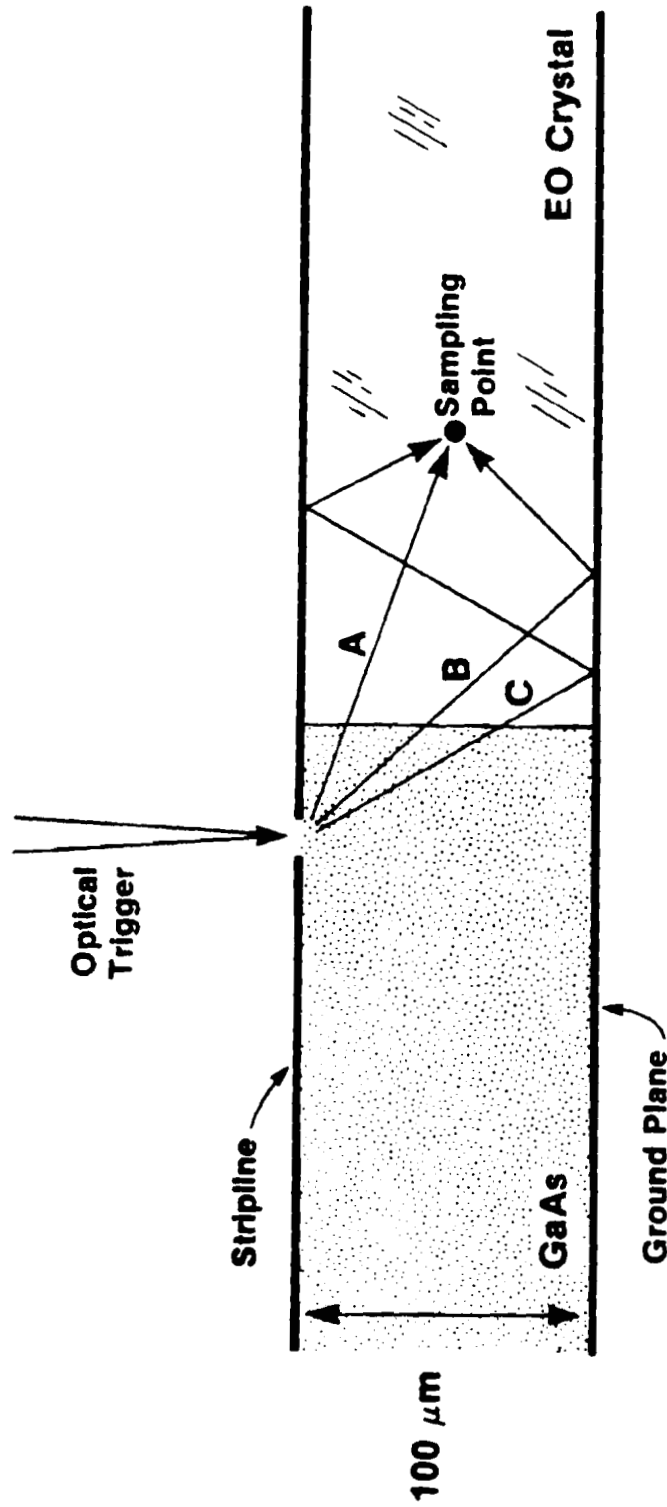


Figure III-18 Geometry for the observation of higher order modes
(A is singly reflected, B is doubly reflected)

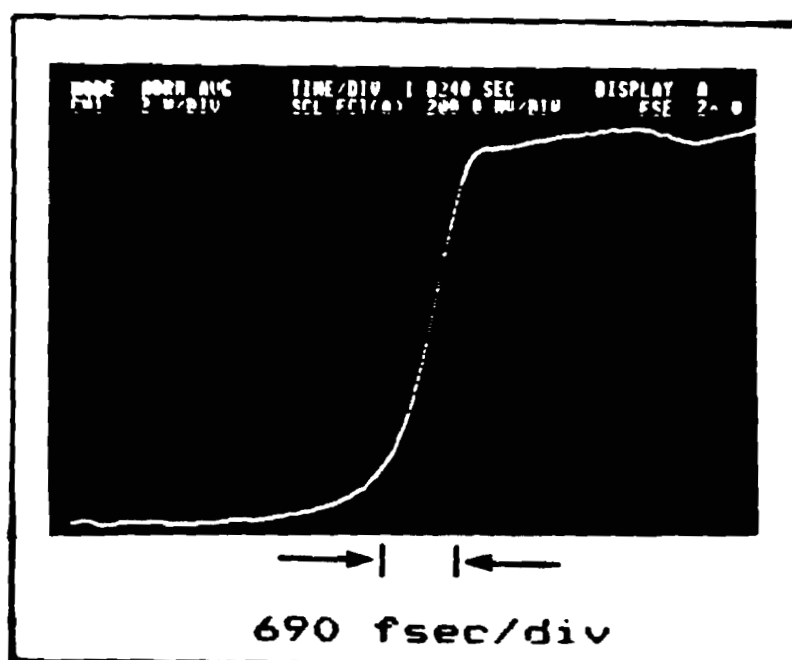
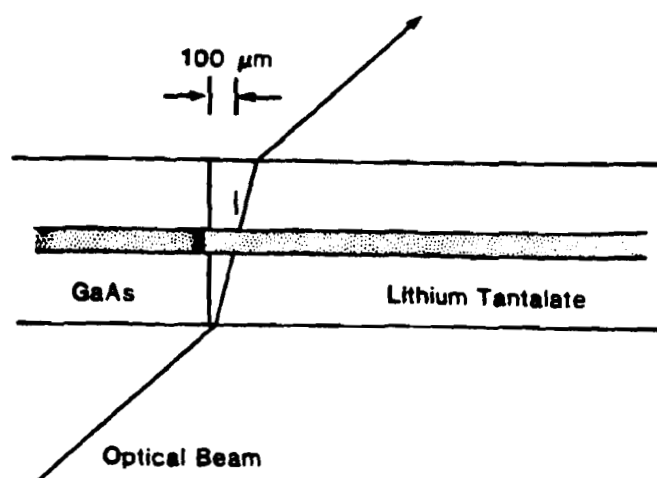


Figure III-19

Trace of a 550 fs effective risetime and the associated electrode geometry

the observed dispersive behaviour in the measured signal. In order to determine the sampling resolution in this case, it is common practice to measure the 10% to 90% time of the tangent to the curve at its point of maximum slope. This measurement results in a temporal resolution figure of 550 fs, in excellent agreement with the theoretical limit of 510 fs for this configuration (see Sect. II.C.2.). Figure III-20 shows the frequency spectrum of the trace in Figure III-19 obtained by calculating the step function's fast fourier transform. The transform serves to demonstrate that frequency components up to 1 THz are actually being generated and measured. The actual risetime of the signal at the very edge of the crystal can be estimated by characterizing the magnitude of the dispersion in this geometry. The extrapolation for this arrangement of the 100 μm crystal is considered in detail in section III.C.3.

We have described the many effects that contribute to the temporal resolution of the electro-optic sampling technique. While beam orientation plays an important role, it is the crystal thickness that determines the maximum frequency that will propagate without generating higher order modes that distort the signal. Given a suitable crystal geometry, we have demonstrated that the waist size of the sampling beam within the crystal is the final criterion determining the sampling gate width. The experimental results are in excellent agreement with the simple theoretic-

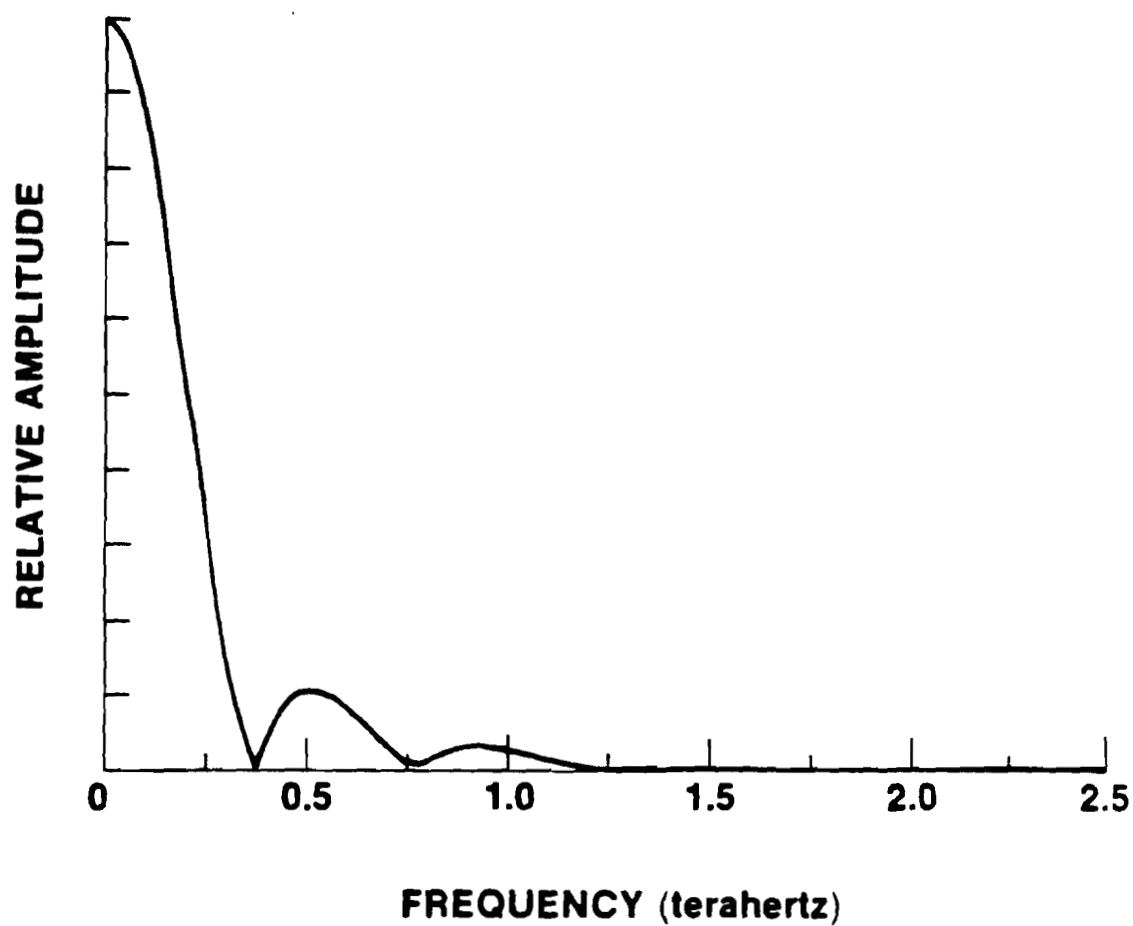


Figure III-20 Fourier transform of a 550 fs risetime signal
(Transform of trace in Figure III-19)

cal model presented earlier in this dissertation. Both demonstrate that subpicosecond resolution is possible and predict that resolution near 200 fs should be possible by employing smaller waist sizes within the crystal.

III.C.3. Electrical dispersion

As discussed in the theory section (II.C.1.), dispersive effects in the open stripline geometry can be considerable. For electro-optic sampling purposes, dispersion can be avoided to a large degree by sampling the electrical signal before it has propagated any appreciable distance along the electrodes. However, the fact that the electro-optic crystal has a long open aperture enables us to observe the transient at various points as it travels along the stripline. By sampling at ever increasing distances along the electrodes, we can analyze the dispersive nature of the particular electrode geometry and observe how it contributes to distortion of the original electrical pulse.

We have measured the effects of dispersion for three different crystal thicknesses. By horizontally translating the sampling crystal by a known amount with respect to the stationary sampling beam as shown in Figure III-21, we interrogate the crystal aperture at ever increasing distances away from the electrical source. Sampling at each successive point provides a progression of pulse shapes that displays the accumulating effects of the dispersive strip-

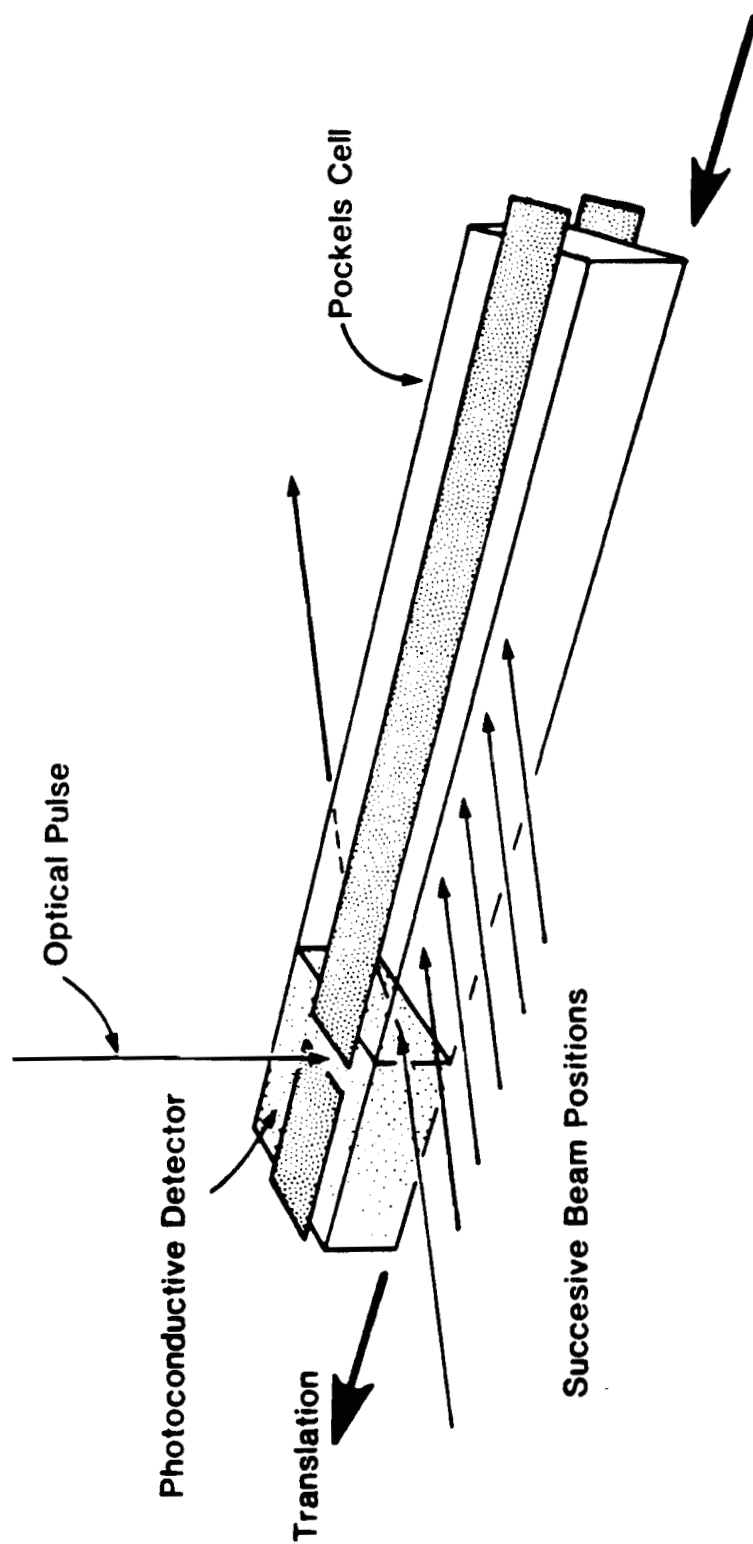


Figure III-21
Geometry for investigating stripline
dispersive effects

line. Figures III-22, 23, and 24 each show the progressive dispersion of an input signal for crystal thicknesses of 500 μm , 250 μm , and 100 μm respectively. In each case the integrated type sampling head was used with the same photo-conductive GaAs detector as the signal source.

In all cases it can be seen that the early effects of dispersion introduce a slowly rising signal, or foot, before the slope of the signal sharply increases. The appearance of the foot can be understood by remembering the simple functional form of the dispersion curve as presented in section (II.C.1.). When a signal contains frequencies in the regime of the critical frequency, f_c , for a particular geometry, the lower frequencies will experience a lower effective dielectric constant, ϵ_{eff} , and hence travel at a higher velocity along the stripline. Higher frequencies, in turn, travel more slowly due to an increased ϵ_{eff} . Thus, the foot that develops is due to the lower frequencies arriving at the sampling point earlier than the high frequencies.

Since the dispersion curve is basically two-valued, with a relatively narrow transition regime in-between, it conceptually divides the signal bandwidth into two "packets", one containing the lower frequencies and the other, higher frequencies. These "packets" propagate along the stripline at two different velocities as determined by the

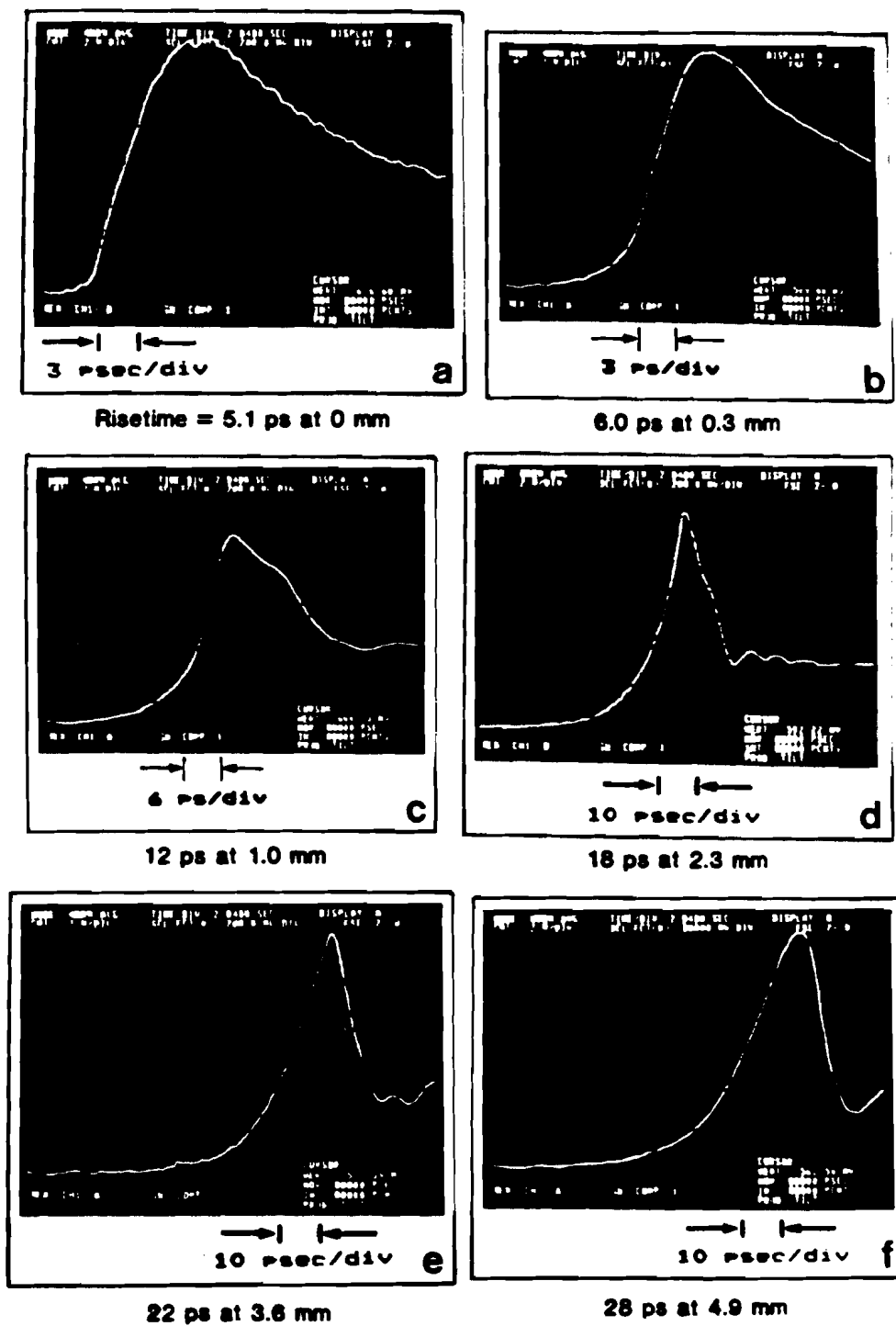


Figure III-22
Progressive dispersion in the 500 μm
thick modulator

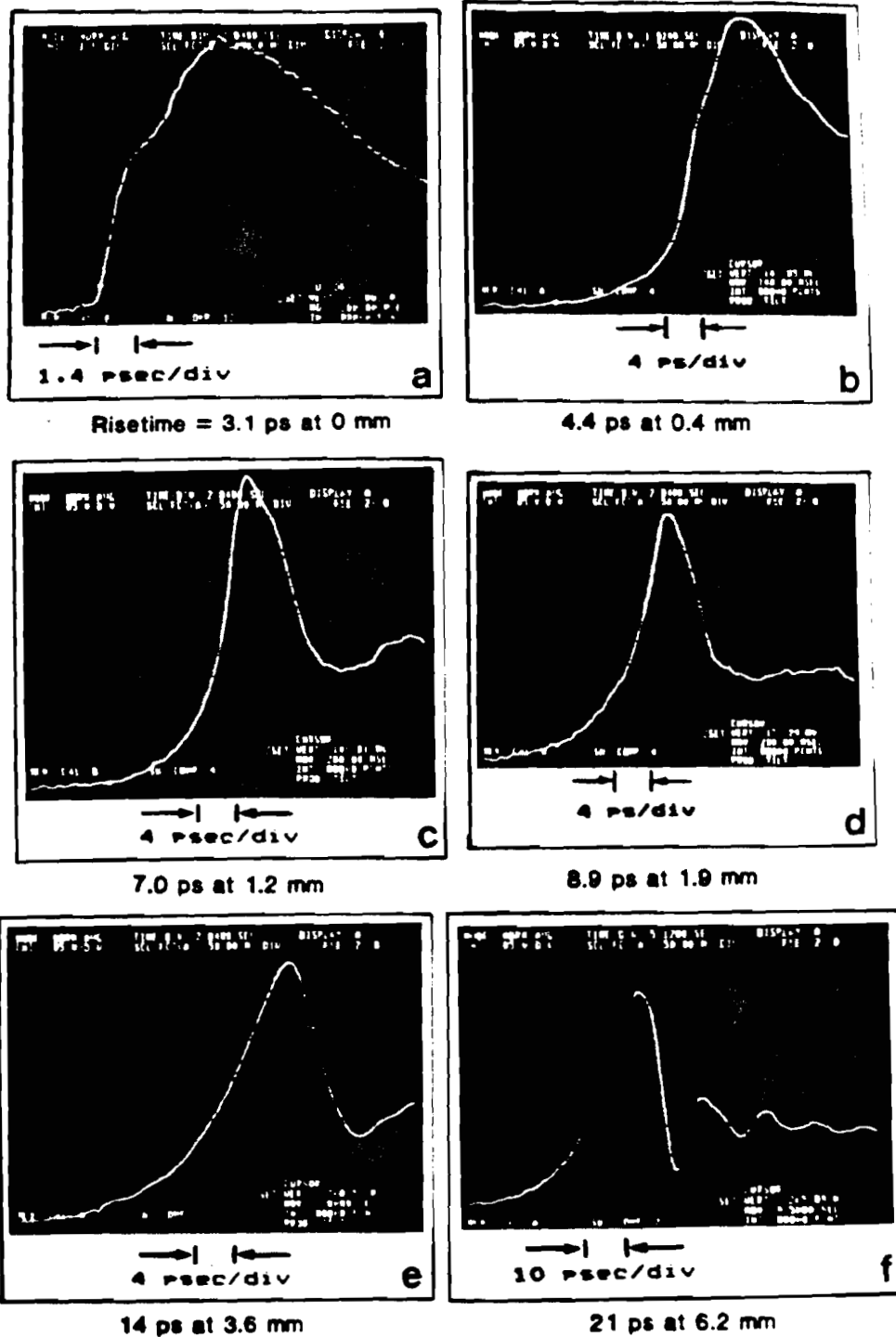


Figure III-23

Progressive dispersion in the 250 μm
thick modulator

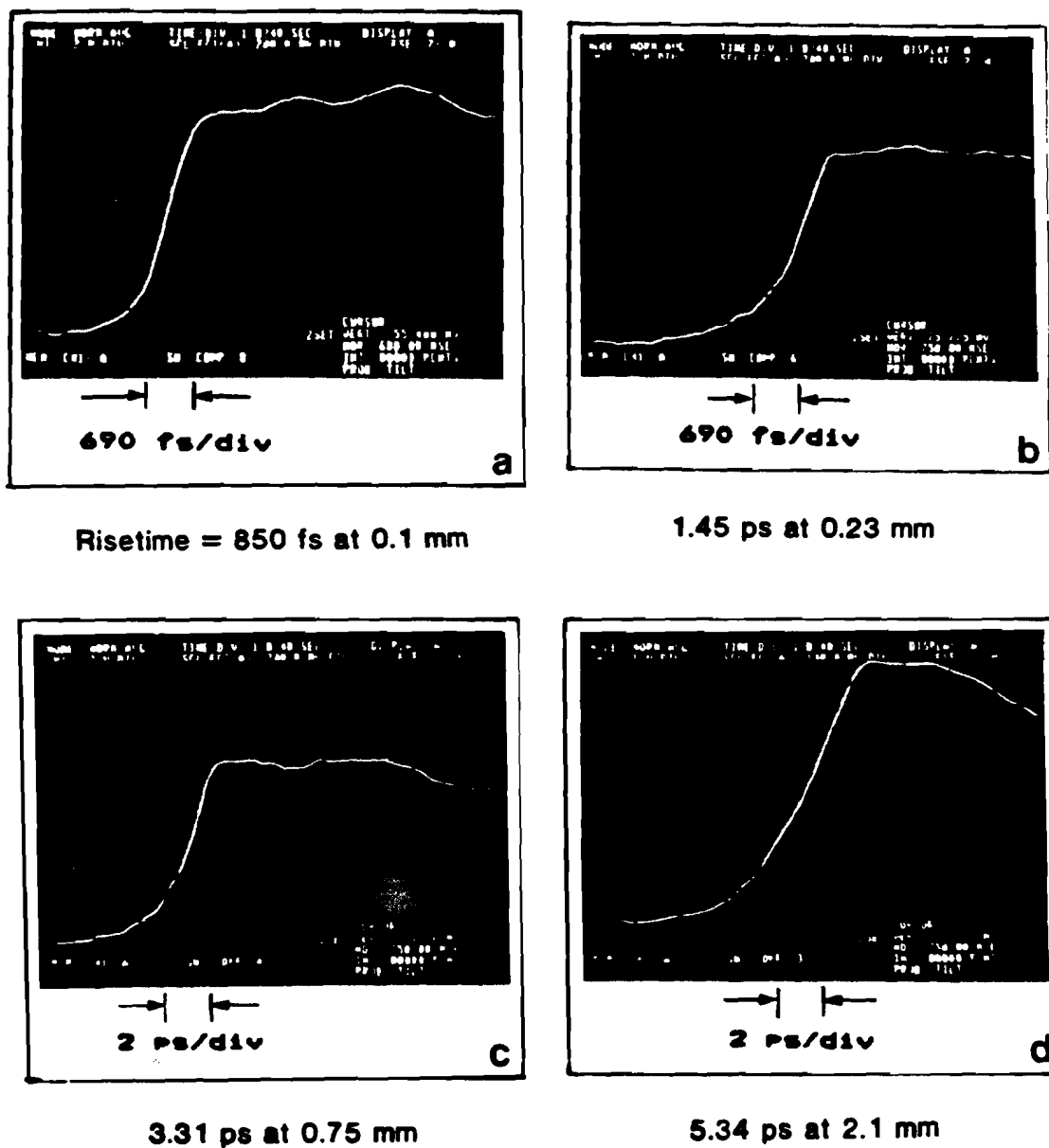


Figure III-24
Progressive dispersion in the 100 μm
thick modulator

extreme values of the dispersion curve. As discussed above, the high frequency "packet" travels slower than the low frequency "packet." At the beginning of the stripline, however, both "packets" are overlapped and generate the undispersed signal that is shown as the first trace of each series. As the signal travels down the Pockels cell transmission line, the high frequencies are delayed more and more. Wherever they appear with respect to the low frequencies, they generate higher frequency structure in the observed signal. The separation of high and low frequencies is especially evident in the progressions of Figures III-22 and III-23. Figure III-22 shows the progression of dispersion as the generated electrical pulse propagates along the 500 μm thick transmission line. Figure III-23 shows a similar progression for the 250 μm crystal transmission line. The sampling position is measured from the end of the crystal next to the detector, and is listed along with the corresponding risetime in each trace. The earlier traces show only a small amount of dispersion and hence the high frequency "packet" still appears on the leading side of the signal. In later stages of propagation, the high frequencies contribute their effects only to the trailing side of the pulse. After considerable accumulated dispersion, the trailing side falls off much faster than the low frequency dominated risetime. The presence of the delayed high frequencies is even more evident in Figure III-23f where they generate a ringing

effect after the initial portion of the electrical pulse.

It is valuable to graphically compare the magnitude of the dispersive effect as a function of crystal thicknesses. Figure III-25 plots the 10%-90% risetime of the observed signal as a function of distance along the electrodes for the 500 μm and 250 μm thick crystals as displayed in figures III-22 and III-23. Since the same detector is used in both cases, with the same optical illumination pulses, it is assumed that the frequency spectrum of the generated signal is also the same in both cases. The overall slope of the curves is an indication of the magnitude of the dispersive effect. A larger slope indicates a longer risetime for the same propagation distance. As seen from Figure III-25, the thinner crystal has a smaller slope which implies less dispersion. This relationship agrees well with the theoretical model of the dispersive effects elaborated in section (II.C.1.). In other words, a thinner crystal has a higher critical frequency and hence has more of the signal bandwidth propagating as a quasi-TEM mode below f_c . As a result, the signal experiences less dispersion.

Figure III-26 is a plot of the early dispersive effects encountered in the 100 μm crystal geometry. As mentioned in the previous section, it was not possible to sample the electrical signal closer than 100 μm from the end of the crystal (see Figure III-19). However, we wish to determine

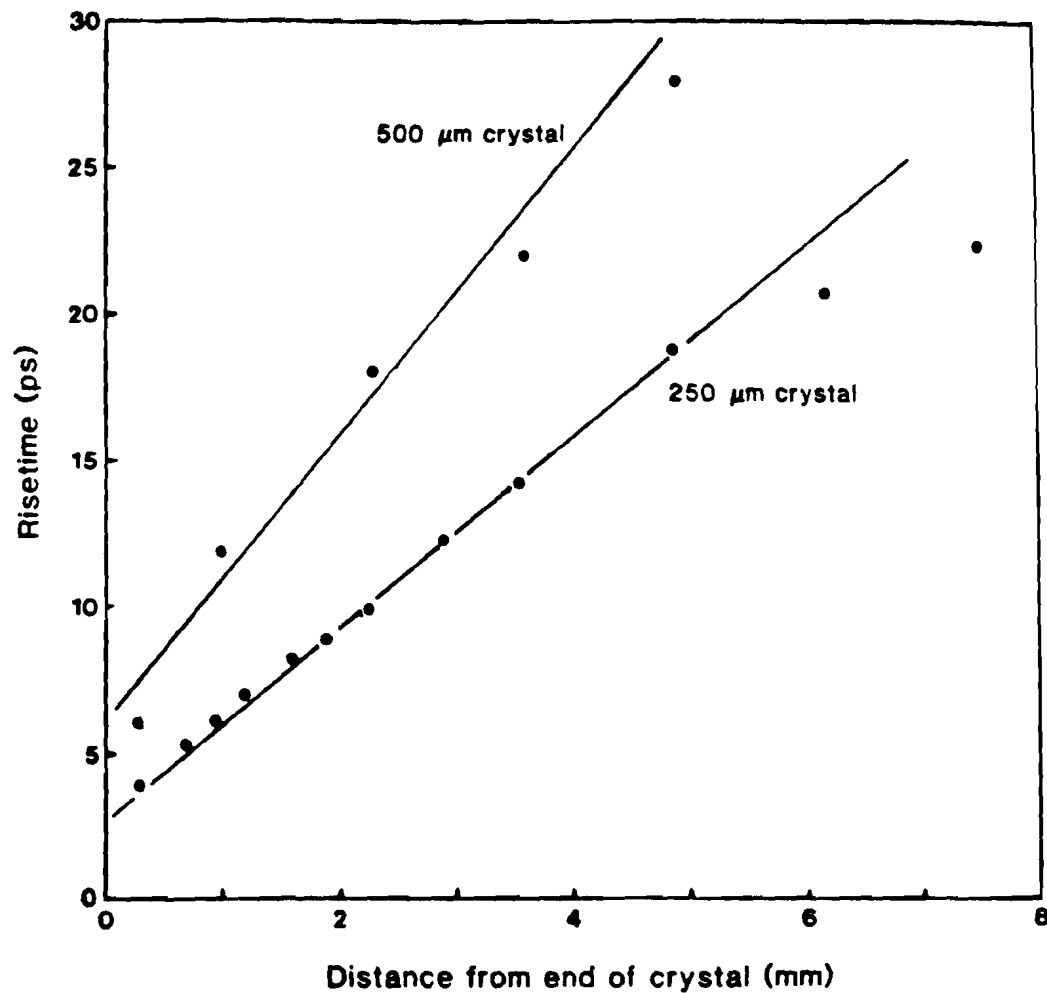


Figure III-25
Comparison of the dispersive effects for the
500 μm and 250 μm thick modulators

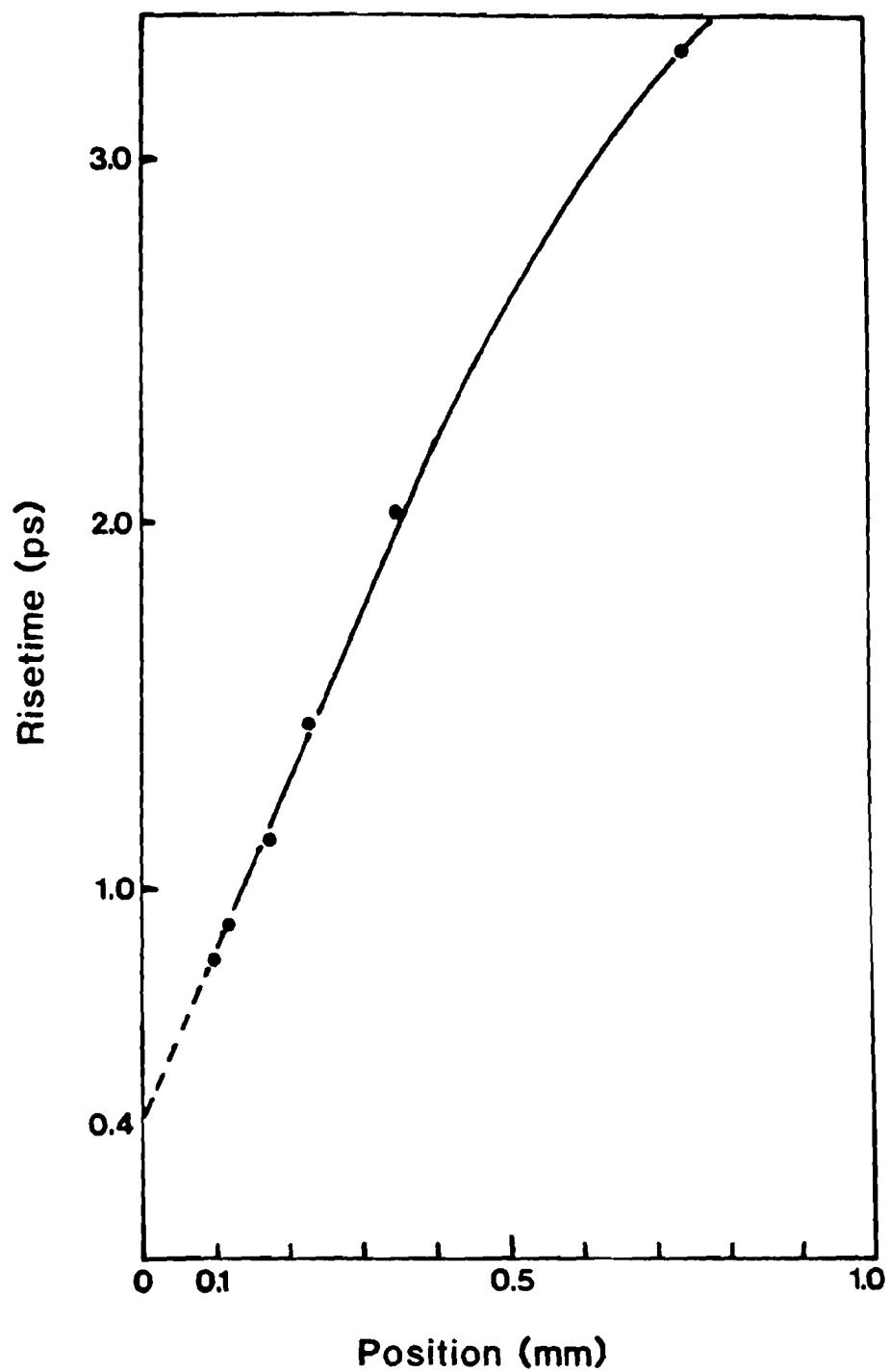


Figure III-26

Electrical dispersion in the 100 μm
thick modulator

the risetime that should be observed at the end of the crystal. The linearity of the dispersion curve implies that the measured risetimes are not limited by the resolution of the sampler. If resolution were the limit, shorter measured risetimes would asymptotically approach the resolution limit. The linear behaviour of the dispersion plot justifies its extrapolation. By extrapolating backwards towards the zero mm position, we can predict an actual risetime of approximately 400 fs that could be realized by sampling at the very edge of the crystal, before dispersion is encountered.

III.C.4. Applications

This section will demonstrate several different applications of the electro-optic sampling system as a tool for characterizing the electrical properties of picosecond devices and materials. We consider three measurement problems that are difficult, if not impossible, to do effectively by any other means: 1) measuring the effective dielectric constant in the regime of tens of GHz, 2) characterizing transmission cable properties and 3) evaluating the performance of newly developed indium phosphide photodetectors.

III.C.4.a. The effective dielectric constant

As detailed in the theory, the actual value for the

dielectric constant of a material in an open stripline geometry is not the commonly documented "relative" value. The effective value, \mathcal{E}_{eff} , depends upon the specific geometrical parameters and also upon the frequency of the electrical field. In the regime of many tens of gigahertz, the problem of experimentally determining \mathcal{E}_{eff} is all the more difficult.

The electro-optic sampling system offers a novel method for measuring the effective dielectric constant. We have approached the measurement of \mathcal{E}_{eff} in two somewhat different ways that both rely on determining the velocity of propagation for a particular electrical signal. We use the 250 μm integrated sampling head with a GaAs photoconductive detector. By knowing how far the signal travels in the electro-optic crystal and measuring how much time it takes, we can calculate its velocity, V_e . The ratio of the speed of light in vacuum, $c=3 \times 10^8$ m/s, to V_e yields the square root of \mathcal{E}_{eff} .

Figure III-27 shows two shifted curves generated by moving the sampling head by 0.1 mm with respect to the sampling beam between traces. The delay incurred (at the 50% points) is measured to be 2.1 ps which yields an electrical velocity, $V_e=c/6.1$ and an $\mathcal{E}_{\text{eff}}=37$. Since Figure III-27 displays a symmetrical risetime of 2.7 ps we can calculate the fundamental frequency to be 0.35/2.7 ps or 86 GHz. From the

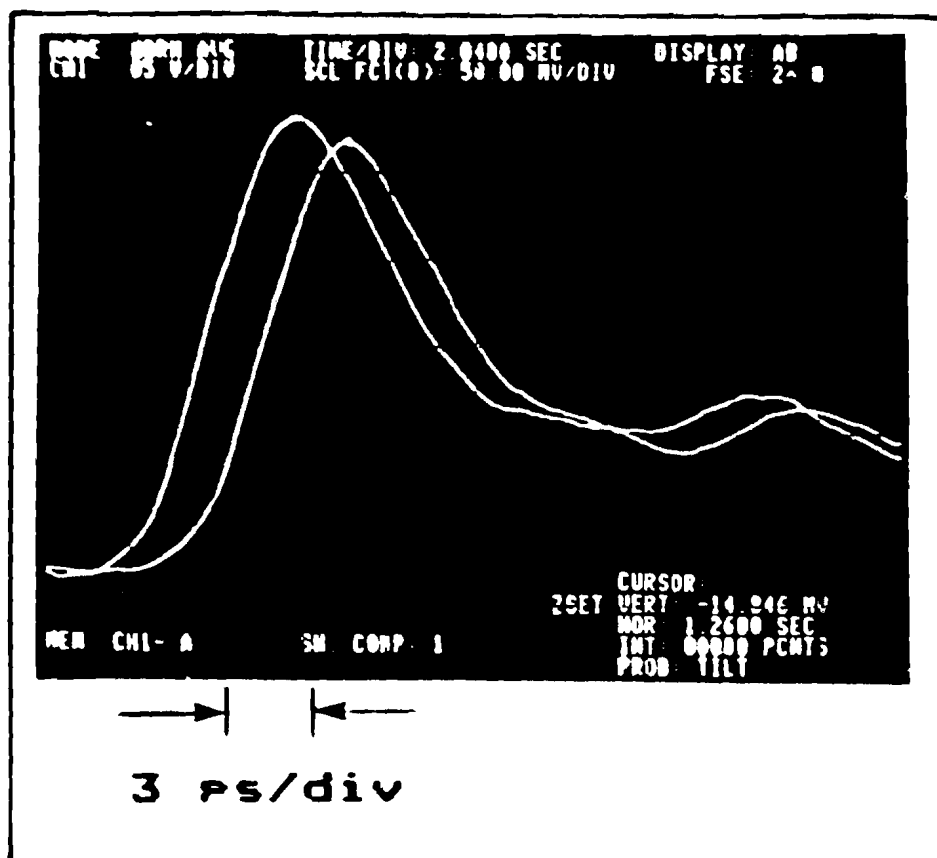


Figure III-27

Delayed traces for measurement of the effective dielectric constant

theory we find that an 86 GHz signal in this geometry should experience an ϵ_{eff} of 39. Thus, we see good agreement between the theory and this experiment.

An alternate method by which to determine ϵ_{eff} is to allow the generated signal to propagate to the end of the crystal and have a portion reflect back due to the impedance discontinuity there. Figure III-28 shows the sampling geometry employed and the resulting trace. By sampling 3.56 mm from the GaAs we see the signal as it passes the sampling point three times, multiply reflecting from both ends of the crystal. The signal takes 410 ps to travel the 22.88 mm round trip between the sampling point and the far end of the crystal. The delay time implies a velocity of $c/5.4$ and a corresponding ϵ_{eff} of 29. Since the signal travels relatively far, only the fundamental quasi-TEM mode dominates. Theory predicts that the value of ϵ_{eff} in this regime should be 30.6, again very close to our experimental value.

The experimental values of ϵ_{eff} we have determined are about 5% lower than those predicted by the theory. The discrepancy could be due to the actual electrode geometry employed. Since we use a balanced stripline that has the structural supporting ridge as its lower electrode, more field lines exist outside the dielectric than would be the case for a true balanced stripline. The distorted field

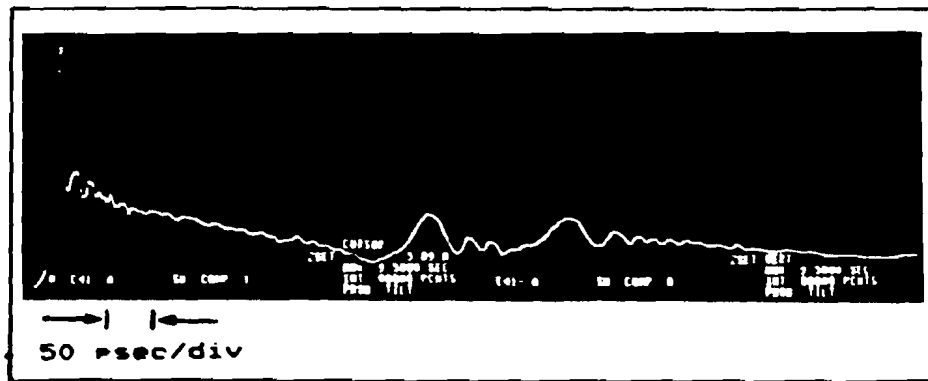
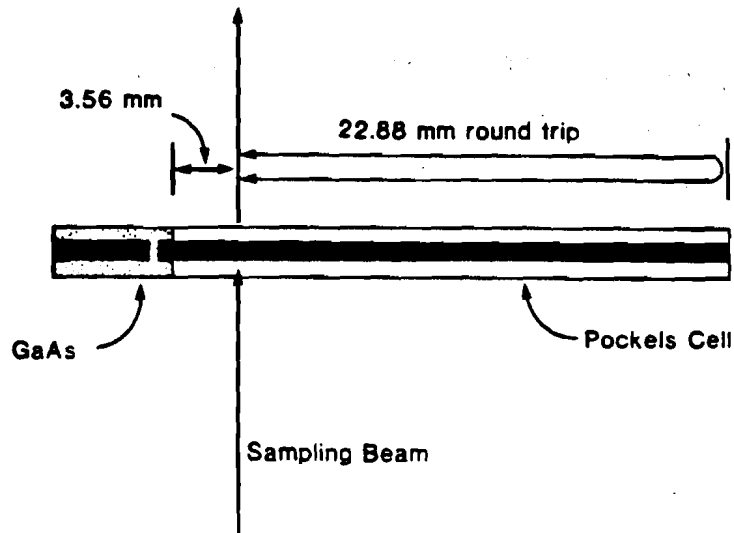


Figure III-28

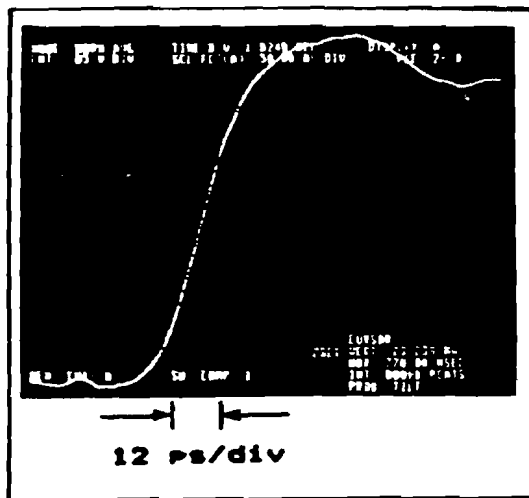
Sampling geometry and corresponding trace for the
characterization of the dielectric constant
(Calculated by measurement of round trip time for known distance)

structure has the effect of introducing a systematic error that increases the electrical velocity and thus effectively reduces ϵ_{eff} , as we observe.

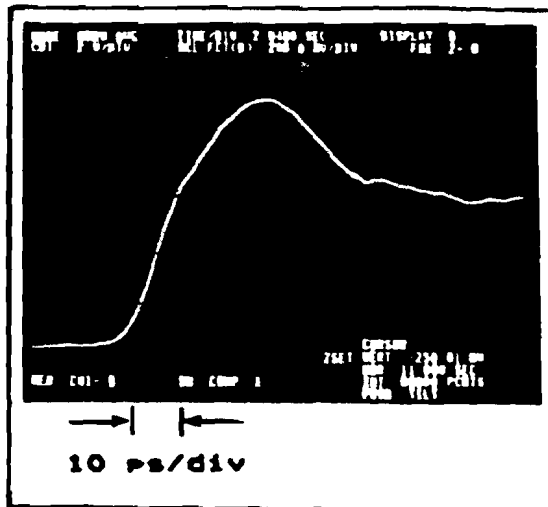
III.C.4.b. Cable and connector bandwidths

When employing high speed transmission cables, one usually wishes to know the highest frequency that can be propagated without deleterious effects. The highest frequency is usually determined by characterizing the spectral response of the cable in the frequency domain. The highest frequency also corresponds to the shortest risetime that can be propagated without dispersion. The electro-optic sampling system enables direct measurement of the risetime in the temporal domain. We have characterized three cable and connector geometries and find the published specifications to be in close agreement with our findings. We test both 17 GHz and 38 GHz cables and connectors as well as the conventional RG 58 coaxial cable.

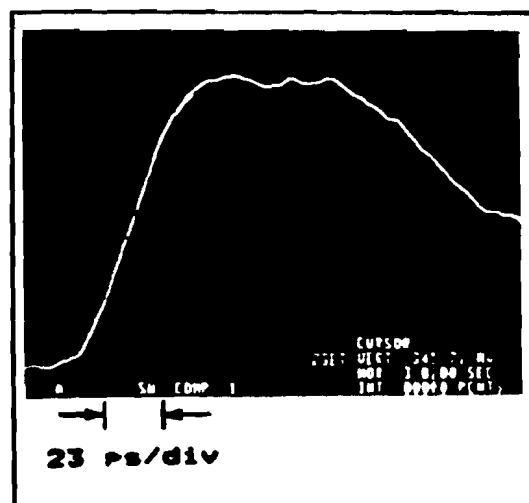
Figure III-29a depicts the resulting signal generated by a GaAs photoconductive detector built in a 17 GHz connector structure and connected to the 500 μm (38 GHz) sampling head by 2 cm of 60 GHz semi-rigid cable. In this situation we expect the observed signal to be limited by the detector connectors. The initial risetime is measured to be 19 ps corresponding to a maximum observed frequency of $0.35/19 \text{ ps} = 18 \text{ GHz}$ and within experimental error of the expected 17 GHz



a) 17 GHz connector



b) 38 GHz connector



c) RG 58 cable (10 GHz)

Figure III-29

Characterization of cable and connector bandwidths

limit. The signal continues to rise, with less slope, after the initial risetime due to delayed reflections associated with impedance discontinuities in the detector structure.

Figure III-29b results from the same situation as just described except that 38 GHz connectors are now also used for the detector structure. Again neglecting the signal due to detector reflections, we measure a risetime of 9.5 ps which corresponds to an observed maximum bandwidth of 37 GHz, once again verifying the published specification of 38 GHz within experimental error.

Figure III-29c results from employing the 17 GHz detector structure and propagating the signal through 30 cm of RG 58 flexible coaxial cable to the same sampling head as before. Detector reflections are no longer resolvable and the risetime is 36 ps implying a maximum bandwidth of approximately 10 GHz. Once again this is the typical limit for a short length of such cable.

III.C.4.c. Indium phosphide detectors

A demonstrative example of how the electro-optic sampling system can be employed in ultrafast device research is the characterization of picosecond photodetectors. Through collaboration with members of the Mass. Institute of Technology's Lincoln Laboratories, we were able to obtain several of their newly designed indium phosphide photodetec-

tors.⁶⁴ The investigators were not able to measure the risetime of the detectors because the resolution of their test equipment, approximately 50 ps, was not adequate. By using the 500 μm integrated sampling head we have subsequently found that their devices actually respond in approximately 5 ps.

The initial devices contained the active InP detector element implanted in a substrate of alumina between relatively long striplines as depicted in Figure III-30a. As shown, this structure was bonded to the end of the 500 μm electro-optic crystal for characterization. The trace in Figure III-30a shows the measured response of the device to 120 fs CPM laser pulses. The trace has a risetime of 17 ps, but clearly displays characteristics typical of dispersion. The slower leading edge followed by a steep rise to the peak indicates that the 7 mm of stripline between the detector and the crystal is introducing a fair amount of dispersion in the signal. Thus it would be advantageous to measure the signal without the presence of the connecting stripline so as to more clearly ascertain the true detector response.

Improved detector structures were fabricated and integrated with the sampling head as illustrated in Figure III-30b. It is seen that a further adaption was made to enable velocity matched sampling and thus achieve a measurement system resolution of approximately 1 ps. The resulting

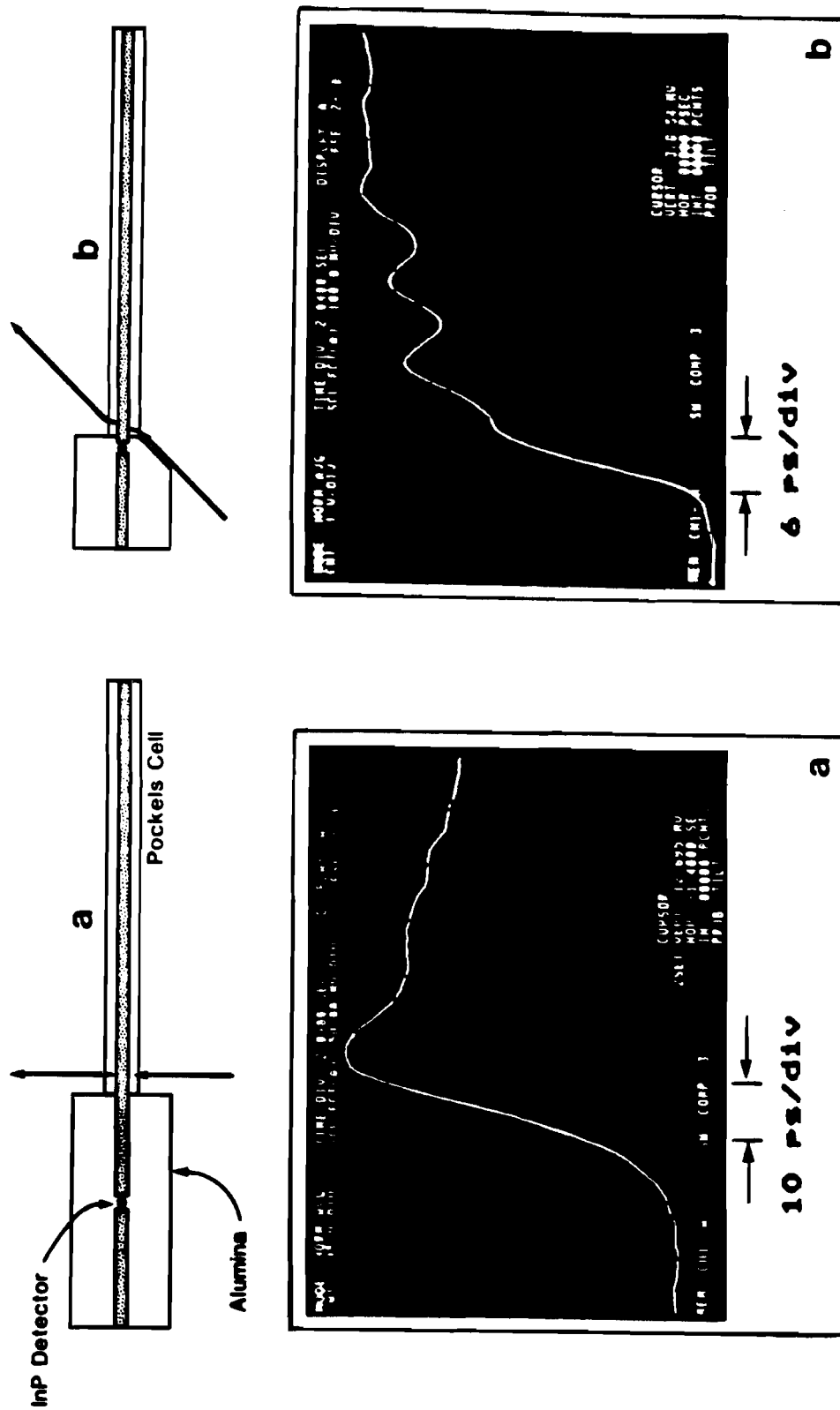


Figure III-30 Sampling geometries and the associated traces for two indium phosphide detectors
 a) original design
 b) new design without extra stripline (dispersion reduced)

signal for this geometry is shown in the trace of Figure III-30b. We see that the detector actually has an initial risetime of approximately 5 ps. The initial rise is followed by some ringing due to an impedance mismatch between the detector striplines and those of the electro-optic crystal. Thus, the electro-optic sampling system has provided valuable insight into the temporal performance of these photodetectors. With this new information, the investigators can develop a better understanding of the device characteristics and subsequently improve their designs.

III.D. Experimental noise limits to sensitivity

As discussed in the theory section II.D., the ultimate limits to signal detectability are the various sources of noise. Given our experimental parameters, we will calculate the expected fundamental limits and compare them to those actually observed.

The most basic types of noise are shot noise and thermal noise, arising from parameters within the detection system (see Figure III-24). Our detectors are E.G.G. FND-100 PIN photodiodes, reverse biased at 90 V, with a responsivity of 0.42 amps/watt at 6200 Angstroms. The detector voltages are developed across 100 kilohm load resistors before being applied to the differential amplifier. The load resistor value converts the responsivi-

ty of the detectors to 42 V/mW. In the following calculations we will presume that the lock-in amplifier has a time constant corresponding to a measurement bandwidth of 1 Hz, as this is the usual form for noise specifications.

With no optical signal on the detectors, there are two noise voltages already present. The first is the thermal noise of the load resistor itself. Its value is defined by equation II-65 as follows:

$$V_{\text{THERMAL}}(\text{rms}) = (4kTR_L B)^{1/2} = [(1.6 \times 10^{-19})(100k)]^{1/2} = 4.02 \times 10^{-8} \frac{\text{V}}{\sqrt{\text{Hz}}} \quad \text{II-7}$$

The second noise signal is the dark current present in the absence of signal. The DC dark current is approximately 100 nanoamperes in our case and hence has an associated shot noise of:

$$\begin{aligned} V_{\text{DARK}}(\text{rms}) &= i_{\text{noise}} R_L = (2q i_D B)^{1/2} R_L \\ &= (2(1.6 \times 10^{-19})(100 \times 10^{-9}))^{1/2} 100k = 1.8 \times 10^{-8} \frac{\text{V}}{\sqrt{\text{Hz}}} \quad \text{III-8} \end{aligned}$$

These two combined voltages represent the limit in detectability for extremely weak optical signals. The optical power necessary to generate a voltage equal to this rms noise level is called the noise equivalent power (NEP) and can be calculated by using the responsivity. The total dark noise voltage $V_{dt}(\text{rms})$ is given by:

$$V_{dt} = (V_{TH}^2 + V_{DK}^2)^{1/2} = 4.4 \times 10^{-8} \text{ V} / \sqrt{\text{Hz}} \quad \text{III-9}$$

Dividing V_{dt} by the voltage responsivity yields a NEP = 1.0×10^{-12} watts/Hz. Our situation is different in that although we are attempting to measure diminishingly small signals, they are on top of a relatively large DC level. We will see that, in this situation, shot noise due to the signal current becomes the dominant effect.

We typically realize about 2.4×10^{-4} watts of optical power at each detector which gives rise to a signal current, i_s , of about 1×10^{-4} amps and a DC voltage of 10 V. The signal shot noise, V_{shot} is then:

$$V_{SH}(rms) = i_{SH} R_L = (2 (1.6 \times 10^{-19}) (1 \times 10^{-4}))^{1/2} 100K = 5.6 \times 10^{-7} \text{ V} / \sqrt{\text{Hz}} \quad \text{III-10}$$

which is about an order of magnitude larger than V_{dt} . Since we employ two detectors, the total shot noise, V_{ts} , is:

$$V_{ts} = (2 V_{SH}^2)^{1/2} = 7.9 \times 10^{-7} \text{ V} / \sqrt{\text{Hz}} \quad \text{III-11}$$

If shot noise were the only source of noise, we could realize a S/N of:

$$\frac{S}{N} = 20 \log \left(\frac{10 \text{ V}}{7.9 \times 10^{-7} \text{ V}} \right) = 142 \text{ dB} / \sqrt{\text{Hz}} \quad \text{III-12}$$

The noise level can be converted into an equivalent

voltage level on the electro-optic crystal by using equation II-25. The equivalent voltage is the amplitude of the signal applied to the electro-optic crystal that would produce an intensity modulation (ΔT) and corresponding AC detector voltage equal to the noise voltage level. From the above calculations we find that $V_{ts}/10$ V DC would be the minimum detectable intensity modulation, $\Delta T = 7.97 \times 10^{-8} / \sqrt{\text{Hz}}$. For a typical halfwave voltage of 2000 V, we find that ΔT corresponds to a minimum signal voltage of ΔV , given by:

$$\Delta V_{\min} = \frac{\Delta T_{\min}}{1.57} V_{\pi} = \frac{7.97 \times 10^{-8}}{10(1.57)} (2000) = 1.02 \times 10^{-4} \frac{\text{V}}{\sqrt{\text{Hz}}} \quad \text{III-13}$$

Therefore, in the shot noise limit, with a bandwidth of 1 Hz, the smallest voltage we could expect to measure would be about 100 μV which is about a factor of 10 less than we experimentally observe. The difference is attributed to $1/f$ noise present in the laser beam.

Figure III-31 shows the noise spectrum of the CPM laser as measured by a single detector and audio frequency spectrum analyzer. The spectrum exhibits the $1/f$ like dependence near DC and the harmonics of the 60 Hz power line frequency. At our lock-in frequency of 808 Hz, the noise level was measured to be almost 90 dB below the DC level for a bandwidth of 15 Hz. For a DC level of 10 V, the corresponding noise level is $8.2 \times 10^{-5} \text{ V}/\sqrt{\text{Hz}}$, and minimum detectable intensity modulation is $\Delta T = 8.2 \times 10^{-6} / \sqrt{\text{Hz}}$ which

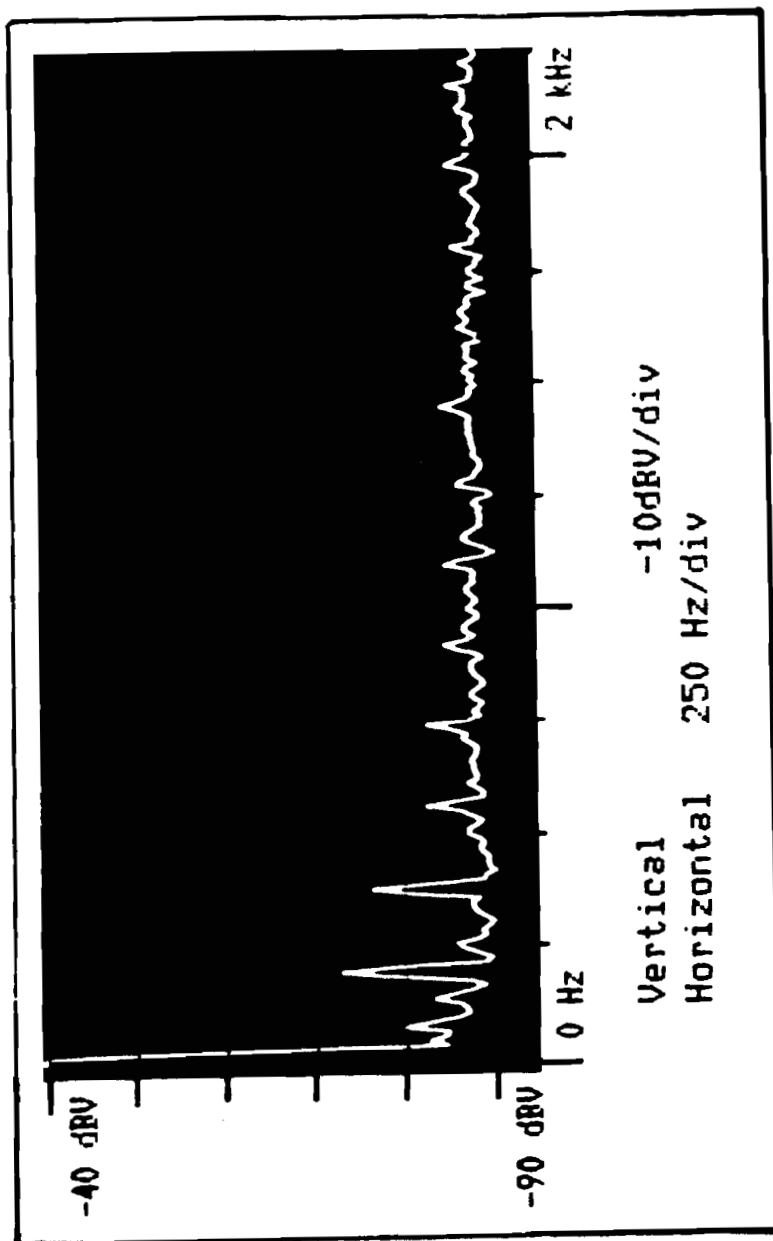


Figure III-31 CPM laser noise spectrum

is about 100 times the shot noise limit. The $1/f$ noise level implies that the minimum detectable signal on the crystal should be about $10 \text{ mV}/\sqrt{\text{Hz}}$ without using a differential amplifier. Thus, we obtain a feeling for the significant amount of $1/f$ noise that exists in this situation.

Experimentally we find that the differential amplifier can reduce amplitude fluctuations anywhere from a factor of 10 to a factor of 100 depending on the operation of the laser. If we conservatively assume a factor of 10, we see that the minimum detectable ΔT should approach $8 \times 10^{-7}/\sqrt{\text{Hz}}$ corresponding to a minimum ΔV at the crystal of about $1 \text{ mV}/\sqrt{\text{Hz}}$. Such a ΔV is in excellent agreement with the experimentally determined sensitivity of about 0.5 mV for a TC of 300 ms, which translates to a minimum ΔT of $9.5 \times 10^{-7}/\sqrt{\text{Hz}}$ and minimum ΔV of approximately $1.2 \text{ mV}/\sqrt{\text{Hz}}$.

Thus we have found that the $1/f$ noise from the CPM laser at 808 Hz is about 100 times the shot noise limit of the signal current. The use of a differential amplifier enhances the sensitivity by about a factor of 10. The overall sensitivity of the electro-optic crystal with a halfwave voltage of 2000 V is near $1 \text{ mV}/\sqrt{\text{Hz}}$, which corresponds to a modulation depth of 8×10^{-7} . Only by increasing the lock-in frequency is it possible to avoid most $1/f$ noise and operate closer to the shot noise limit of $100 \mu\text{V}/\sqrt{\text{Hz}}$.

CHAPTER IV

SUMMARY

In this dissertation, we have documented the development of electro-optic sampling as a novel, state of the art technique for the characterization and analysis of picosecond electrical waveforms. The technique incorporates subpicosecond optical pulses and the Pockels effect in order to achieve subpicosecond temporal resolution. We have also developed a theoretical model as an aid in understanding and predicting temporal performance in a variety of experimental embodiments. The theoretical calculations have been found to corroborate the experimental results rather well, in addition to providing considerable insight into the limiting parameters of our technique.

The Pockels effect lends itself to the characterization of picosecond electrical signals in many respects. First, and foremost, is that the mechanism responsible for the Pockels effect, ie. the polarizability to the electric field, has an effective temporal response extending to about 10 THz. Second, the ability to use optical pulses directly to sample voltage levels allows the technique to benefit simply from the availability of subpicosecond laser pulses. A third attribute arising from the use of the Pockels effect is that the optical pulses probe the induced electric field

without altering the circuit characteristics in any way. Other advantages of the electro-optic technique are the wide spectral response of the Pockels cell and the optical isolation of the detection electronics from the signal under investigation.

We have found the Pockels effect to be optimally implemented in a velocity matched traveling-wave electrode geometry with lithium tantalate as the electro-optic medium. In the traveling-wave configuration, velocity matching is easily accomplished, and hence, the temporal resolution is almost entirely dictated by the temporal and spatial extent of the optical pulse. We found that with 120 fs optical pulses, the waist size was still the dominant effect limiting the temporal resolution. With a waist size of $15\text{ }\mu\text{m}$, we have demonstrated a temporal resolution of at least 550 fs, in excellent agreement with the theoretically predicted response time of 510 fs. By further reducing the waist size to $3\text{ }\mu\text{m}$ we predict that a temporal resolution of close to 200 fs is possible. Resolution of a few hundred femtoseconds represents an improvement of about an order of magnitude over indirect photoconductive sampling schemes and an improvement of at least two orders of magnitude over conventional electronic sampling instruments.

One must also bear in mind the dispersive character of the open stripline electrode geometry. Below the critical

frequency, dispersive effects are minimal because the signal travels as a quasi-TEM mode. Therefore, the response is constant with frequency. Signals containing frequencies above the critical frequency experience several related dispersive effects that can contribute to a non-linear response characteristic. In addition, the presence of non-TEM higher order modes can also distort the applied signal.

The problem of coupling ultrahigh frequency electrical signals into the traveling-wave geometry and then having them propagate without distortion before they are sampled is non-trivial. However, one must realize that this problem is not one peculiar to the electro-optic sampling technique, but rather one that has to be considered by any high speed measurement scheme. The primary goal of this thesis work was to demonstrate the ultrahigh resolution capability of direct optical techniques. The study of high frequency wave propagation is now a field of study made more accessible by the development of the electro-optic sampling scheme.

The sensitivity of the electro-optic method is dictated by the presence of noise in the measured signal. We have found that the predominant source of noise is $1/f$, or pink, noise in the laser output. The laser noise level yields a typical usable sensitivity of about $1 \text{ mV}/\sqrt{\text{Hz}}$ at 1 kHz. As the detected noise level is a function of measurement system

bandwidth, electronic signal to noise enhancement is effectively accomplished only by bandwidth narrowing techniques such as lock-in amplification and signal averaging. By employing radio frequency lock-in amplification, sensitivities of less than $100 \mu\text{V}/\sqrt{\text{Hz}}$ can be attained. At this level, shot noise in the signal current becomes the inescapable limiting source of noise. Given a typical linearity regime extending from the shot noise limit of $100 \mu\text{V}$ to well over 100 V , we see that the dynamic range of the electro-optic sampling system is greater than 10^6 . This range represents an improvement of nearly three orders of magnitude over conventional electronic sampling techniques.

In conclusion, we have developed an electro-optic sampling system capable of characterizing electrical transients with subpicosecond resolution. Combining several conventional electronic instruments, we have been able to exploit the ultrafast response of the Pockels effect, while retaining a voltage sensitivity of less than 10^{-7} of the crystal halfwave voltage. It is important to emphasize that the temporal resolution is not limited by the electro-optic material, but rather by the finite extent of the optical pulse and the characteristics of the modulator striplines. Such a system now enables the possibility of analyzing many ultrafast electronic devices, materials, and processes with the goal of understanding and improving their operation.

APPENDIX A

LASER PULSEWIDTH MEASUREMENT

Proper operation of the electro-optic sampling system requires a knowledge of the optical pulse duration and form. Several methods exist for the measurement of picosecond and subpicosecond optical pulses,⁶⁵ but the technique of second harmonic correlation is most commonly used for CW mode-locked lasers.⁶⁶ Second harmonic generation is an extremely fast process (see section II.B.1.) and has been employed to measure pulses in the regime of several tens of femtoseconds.

The general experimental configuration is illustrated in Figure A-1. The optical pulse train is split and retroreflected into two parallel but separated beams. These beams are both focussed and overlapped through a non-linear crystal such as lithium iodate and each generate some frequency doubled light. When the delay is adjusted so that the optical pulses overlap in the crystal, a third beam of frequency doubled light is generated, in a direction bisecting the angle between the two original beams. Its amplitude is related to the degree of temporal overlap between incident pulses. The central beam is then spatially selected by an aperture and its intensity measured by a photomultiplier tube. The output of the photomultiplier is placed on the

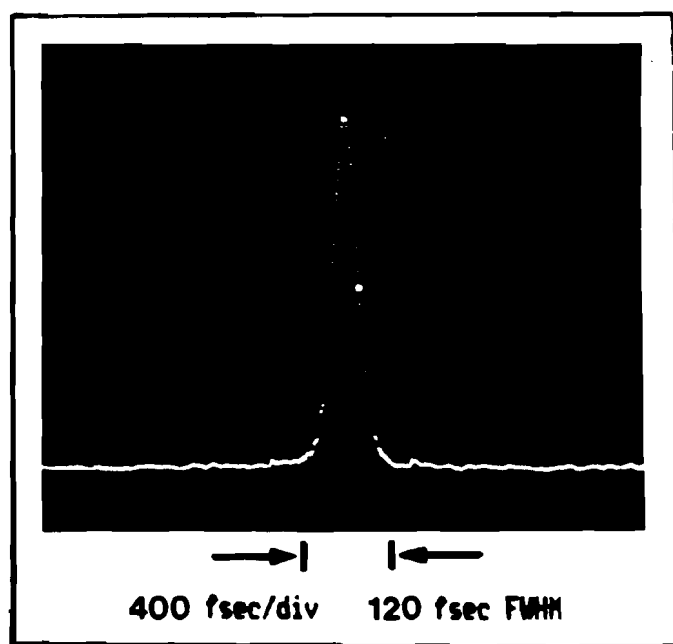
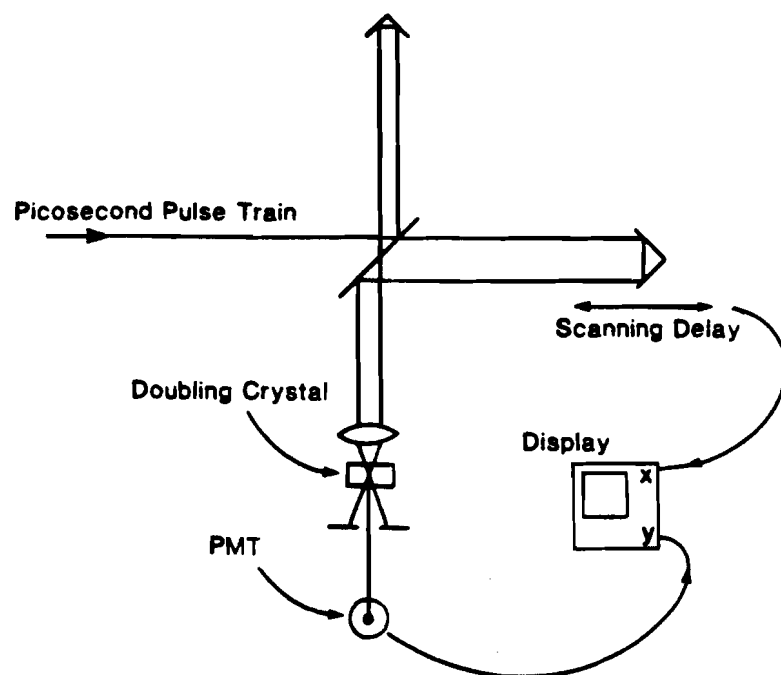


Figure A-1
Scanning auto-correlator configuration and a
typical trace from the CPM dye laser

vertical axis of an oscilloscope while a position transducer on the delay line drives the horizontal axis. By scanning the delay line through the range of pulse overlap, a correlation trace is generated on the oscilloscope. The peak signal occurs when both delay arms are of exactly the same length. The width of the correlation trace is proportional to the duration of the optical pulses and depends on an assumed pulse shape. If the shape is taken to be Gaussian, the full width of the correlation trace at half its peak value is a square root of two wider than the corresponding width of each component.

For proper operation, it is critical that the two beams remain precisely overlapped in the doubling crystal, with the proper angle between them. To maintain proper alignment, the scanning stage must be precisely aligned on axis and the retroreflectors must be of excellent angular accuracy (typically less than 1 milliradian).

Figure A-1 also shows a typical correlation trace generated by the CPM laser. The scale has been corrected for the root 2 proportionality factor and results in a pulsewidth of 120 femtoseconds. The delay line oscillates at approximately 1 Hz. When the CPM laser is operating properly, the correlation trace is very stable both in amplitude and width. There are no extraneous (satellite) pulses in the trace. Extra pulses are indicative of incom-

plete mode-locking, and usually mean that the saturable absorber is being overdriven, which can be corrected by increasing the dye concentration, or reducing the pump power to the gain jet.

APPENDIX B

THE PHOTOCONDUCTIVE EFFECT

In this dissertation, we allude to the high speed and jitter-free nature of the photoconductive effect. Because of these properties, photoconductive devices are employed in opto-electronic systems requiring ultra-precise generation and control of electrical pulses. Examples include "indirect" optical sampling systems (sect. I.B.5.), and also state of the art optical streak cameras.^{67,68} Many materials have been investigated in several different electrode geometries.^{14,69-74} We employ a Cr-doped GaAs photoconductive switch with a simple electrode gap as an ultrafast step function generator for the purpose of investigating the ultimate temporal resolution of the electro-optic sampling system. Therefore, our present interests lie mainly in the mechanisms involved in generating the rising edge of the signal. The only requirement for the fall time is that it be less than the sampling interval (approximately 11 ns).

The photoconductive switch can be electrically represented as a time varying resistance $R(t)$, or inversely, a time varying conductance $G(t)$. Figure B-1 depicts the switch electrode geometry and its simplified equivalent electrical circuit. The photoconductor is placed between two transmission lines of equal characteristic impedance,

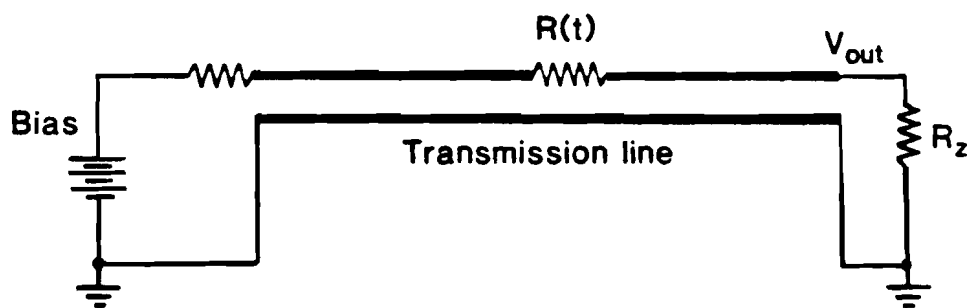
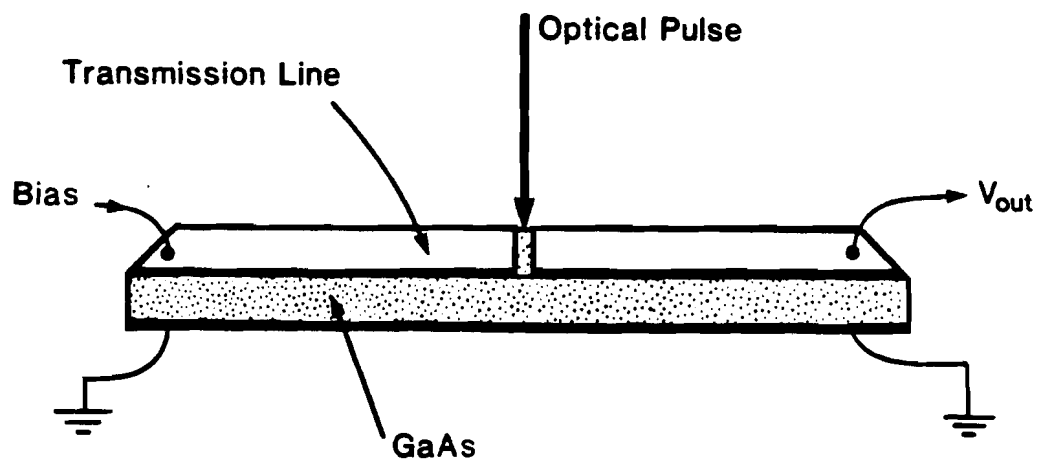


Figure B-1 Photoconductive detector geometry and the circuit equivalent

Z_0 . A bias voltage, V_b , is placed on one of the lines. When the photoconductor is optically triggered, it generates an output voltage, V_o , across the terminating resistor, R_z , of the form:

$$V_o(t) = \left\{ \frac{Z_0}{2Z_0 + R(t)} \right\} V_b \quad B-1$$

If the bias field across the photoconductive gap is greater than 10^4 V/cm (as is usually the case),⁶⁷ then the optically induced carriers travel at the saturation velocity and $R(t)$ can be represented by:

$$R(t) = \frac{h\nu l V_s}{2v_s e E(t)} \quad B-2$$

where $h\nu$ is the photon energy, l is the gap length, v_s is the carrier saturation velocity, e is the electronic charge, and $E(t)$ is the absorbed optical energy as a function of time. $E(t)$ is simply the integrated intensity which can be written as follows:

$$E(t) = \int_{-\infty}^t P(t') dt'$$

From these simple equations we see that the output voltage follows the integral of the optical excitation pulse intensity, and hence the photoconductive pulse generation process is inherently jitter-free. The fall time is dictated by the carrier recombination time which is several

hundred picoseconds for chromium doped GaAs.⁷¹ With the use of 120 fs excitation pulses from the CPM laser, the form of $V_O(t)$ approaches that of a step function in the picosecond regime.

It should be noted that there exist other effects which can alter the ideal behaviour of a photoconductive switch on a picosecond time scale. These effects must not be overlooked. The effects commonly considered are: the bandwidth of the electrode geometry, the RC time constant of the electrode gap, and the dielectric relaxation time.

As detailed in section II.C.1., the bandwidth of the electrode geometry limits the highest frequency that can propagate without experiencing dispersive effects. The generated electrical signal can be severely distorted and its risetime lengthened considerably by the dispersion encountered in a poorly designed stripline. However, we have shown that dispersive effects can be minimized by limiting propagation distances. Gap capacitances typically range between tens and hundreds of femtofarads and can produce time constants up to several picoseconds in specific geometries. The most difficult quantity to mathematically predict is the dielectric relaxation time. This is the time it takes for the applied bias field across the gap to relax, and generally depends highly on the illumination configuration, and the photoconductive gap geometry. In some cases,

the field relaxation process can also introduce an additional fast spurious signal that distorts the ideal photoconductive pulse. Nevertheless, it is believed that the dielectric relaxation time can be less than a picosecond in duration.

REFERENCES

1. L. E. HARGROVE, R. L. FORK, and M. A. POLLACK, "Locking of He-Ne laser modes induced by synchronous intracavity modulation," Appl. Phys. Lett., 5-1, pp. 4-5, 1964.
2. E. P. IPPEN, C. V. SHANK and A. DIENES, "Passive modelocking of the CW dye laser," Appl. Phys. Lett., 21-8, pp. 348-350, 1972.
3. C. V. SHANK and E. P. IPPEN, "Subpicosecond kilowatt pulses from a mode-locked CW dye laser," Appl. Phys. Lett., 24-8, pp. 373-375, 1974.
4. R. L. FORK, B. I. GREENE, and C. V. SHANK, "Generation of optical pulses shorter than 0.1 picoseconds by colliding pulse modelocking," Appl. Phys. Lett., 38, pp. 671-672, 1981.
5. J. A. VALDMANIS, G. MOUROU and C. W. GABEL, "Subpicosecond electrical sampling," IEEE J. Quan. Elec., QE-19, pp. 664-667, 1983.
6. J. A. VALDMANIS, G. MOUROU and C. W. GABEL, "Picosecond electro-optic sampling system," Appl. Phys. Lett., 41-3, pp. 211-212, 1982.
7. J. A. VALDMANIS and G. MOUROU, Patent Pending, University of Rochester, New York, 1981.
8. I. A. D. LEWIS and F. H. WELLS, "Millimicrosecond Pulse Techniques," second ed., Pergamon Press, New York 1959.
9. TEKTRONIX S-6 Sampling Head, Instruction Manual, Tektronix, Beaverton, Oregon 1971.
10. R. A. LAWTON and J. R. ANDREWS, "Optically strobed sampling oscilloscope," IEEE Tr. Instr. Meas., IM-25, pp. 56-60, 1976.
11. S. M. FARIS, "Generation and measurement of ultrashort current pulses with Josephson devices," Appl. Phys. Lett., 36-12, pp. 1005-1007, 1980.
12. D. B. TUCKERMAN, "A Josephson ultra-high resolution sampling system," Appl. Phys. Lett., 36-12, pp. 1008-1010, 1980.
13. D. H. AUSTON and P. R. SMITH, "Picosecond optical electronics for high-speed instrumentation," Laser Focus, pp. 89-93, April, 1982.

14. D. H. AUSTON, "Picosecond optoelectronic switching and gating in silicon," Appl. Phys. Lett., 26-3, pp. 101-103, 1975.
15. C. H. LEE, A. ANTONETTI and G. MOUROU, "Measurements on the photoconductive lifetime of carriers in GaAs by optoelectronic gating technique," Optics Commun., 21-1, pp. 158-161, 1977.
16. D. H. AUSTON, A. M. JOHNSON, P. R. SMITH and J. C. BEAN, "Picosecond optoelectronic detection, sampling, and correlation measurements in amorphous semiconductors," Appl. Phys. Lett., 37-4, pp. 371-373, 1980.
17. D. H. AUSTON, Private communication.
18. A. ANTONETTI, A. MIGUS, M. M. MALLEY and G. MOUROU, "Optoelectronic sampling in the picosecond range," Optics Commun., 21-2, pp. 211-214, 1977.
19. P. R. SMITH, D. H. AUSTON and W. M. AUGUSTYNIAK, "Measurement of GaAs field effect transistor electronic impulse response by picosecond optical electronics," Appl. Phys. Lett., 39, pp. 739-741, 1981.
20. D. H. AUSTON and P. R. SMITH, "Picosecond optical sampling characterization of high speed photodetectors," Appl. Phys. Lett., 41-7, pp. 599-601, 1982.
21. D. H. AUSTON and A. M. GLASS, "Optical generation of intense picosecond electrical pulses," Appl. Phys. Lett., 20-10, pp. 398-399, 1972.
22. P. LEFUR and D. H. AUSTON, "A kilovolt picosecond optoelectronic switch and Pockels cell," Appl. Phys. Lett., 28-1, pp. 21-23, 1976.
23. R. C. ALFERNES, N. P. ECONOMOU and L. L. BUHL, "Picosecond optical sampling technique for measuring the speed of fast electro-optic switch/modulators," Appl. Phys. Lett., 37-7, pp. 597-589, 1980.
24. W. KOECHNER, "Solid State Laser Engineering," pp. 489-491, Springer-Verlag, New York, 1976.
25. I. P. KAMINOW, "An Introduction to Electro-Optic Devices," Academic Press, New York 1974.
26. I. P. KAMINOW and E. H. TURNER, "Linear electro-optic materials," in 'Handbook of Lasers,' pp. 447-459, Chemical Rubber Co., Cleveland, Ohio, 1971.

27. I. P. KAMINOW and E. H. TURNER, "Electro-optic light modulators," Proc. IEEE, 54, pp. 1374-1390, 1966 and Appl. Optics, 5, pp. 1612-1628, 1966.
28. R. T. DENTON, F. S. CHEN and A. A. BALLMAN, "Lithium tantalate light modulators," J. Appl. Phys., 38, pp. 1611-1617, 1967.
29. M. R. BIAZZO, "Fabrication of a lithium tantalate temperature stabilized optical modulator," Appl. Opt., 10, pp. 1016-1021, 1971.
30. I. P. KAMINOW and W. M. SHARPLESS, "Performance of LiTaO_3 and LiNbO_3 light modulators at 4 GHz," Appl. Opt., 6, pp. 351-352, 1967.
31. G. WHITE and G. M. CHIN, "Traveling wave electro-optic modulators," Opt. Commun., 5, pp. 374-379, 1972.
32. C. J. PETERS, "Gigacycle-bandwidth coherent light traveling wave amplitude modulator," Proc. IEEE, 53, pp. 455-460, 1965.
33. W. W. RIGROD and I. P. KAMINOW, "Wide-band microwave light modulation," Proc. IEEE, 51, pp. 137-140, 1963.
34. J. KAFKA, PhD. Thesis, University of Rochester, New York, 1983; and see, for example: B. BOYS, "Surfin' USA," Capitol Records.
35. M. DIDOMENICO and L. K. ANDERSON, "Broadband electro-optic traveling-wave light modulators," Bell Sys. Tech. J., 42, pp. 2621-2678, 1963.
36. I. P. KAMINOW and J. LIU, "Propagation characteristics of partially loaded two-conductor transmission line for broadband light modulators," Proc. IEEE, 51, pp. 132-136, Jan. 1963.
37. D. C. AUTH, "Half-octave bandwidth traveling wave X-band optical phase modulator," IEEE J. Quan. Elec., 5, pp. 622-623, 1969.
38. I. P. KAMINOW, T. J. BRIDGES and M. A. POLLACK, "A 964-GHz traveling wave electro-optic light modulator," Appl. Phys. Lett., 16, pp. 416-418, 1970.
39. H. A. WHEELER, "Transmission-line properties of parallel strips separated by a dielectric sheet," IEEE Trans. Microwave Theory Tech., MTT-13, pp. 172-185, 1965.
40. M. V. SCHNEIDER, "Microstrip lines for integrated

54. LABORATORY FOR LASER ENERGETICS, Target fabrication facility, (J. Drumheller).
55. DYNALLOY Number 350, Silver polymer.
56. OMNI-SPECTRA, OSSM Series connectors.
57. C. V. SHANK, R. L. FORK, and F. BEISSER, "Basic design considerations for femtosecond pulse dye lasers," *Laser Focus*, pp. 59-62, June 1983.
58. R. L. FORK, C. V. SHANK, R. YEN, and C. HIRLIMANN, "Femtosecond optical pulses," *IEEE J. Quan. Elec.*, QE-19, pp. 500-506, 1983.
59. D. KUHLKE, W. RUDOLPH, and B. WILHELMI, "Calculation of the colliding pulse modelocking in CW dye lasers," *IEEE J. Quan. Elec.*, QE-19, pp. 526-533, 1983.
60. E. P. IPPEN and C. V. SHANK, "Techniques for measurement," pp. 83-92, in Ultrashort Light Pulses, S.L.Shapiro ed., Berlin, Germany, Springer-Verlag, 1977.
61. EASTMAN KODAK, Chemical number 14351.
62. D. J. BRADLEY, "Methods of generation," in Ultrashort Light Pulses, S. L. Shapiro ed., Springer-Verlag, New York, 1977.
63. B. KOHLNER and D. BLOOM, *Proc. SPIE Conf.*, San Diego, 1983, to be published.
64. F. J. LEONBURGER and C. COX, *Massachusetts Inst. of Tech.*, Boston, Mass.
65. E. P. IPPEN and C. V. SHANK, "Techniques for measurement," in Ultrashort Light Pulses, S. L. Shapiro ed., Springer-Verlag, New York, 1977.
66. M. MAIER, W. KAISER and J. A. GIORDMAINE, "Intense light bursts in the stimulated raman effect," *Phys. Rev. Lett.*, vol. 17-26, pp. 1275-1277, Dec. 1966.
67. G. MOUROU and W. KNOX, "A picosecond jitter streak camera," *Appl. Phys. Lett.*, 36-8, pp. 623-626, 1980.
68. W. KNOX and G. MOUROU, "A simple jitter free picosecond streak camera," *Optics Commun.*, 37-3, pp. 203-206, 1981.
69. D. H. AUSTON, P. LAVALLARD, N. SOL, and D. KAPLAN, "An amorphous silicon photodetector for picosecond pulses," *Appl. Phys. Lett.*, 36-1, pp. 66-68, 1980.

70. P. R. SMITH, D. H. AUSTON, A. M. JOHNSON, and W. M. AUGUSTYNIAK, "Picosecond photoconductivity in radiation damaged silicon on sapphire films," Appl. Phys. Lett., 38-1, pp. 47-50, 1981.
71. C. H. LEE, "Picosecond optoelectronic switching in GaAs," Appl. Phys. Lett., 30-2, pp. 84-86, 1977.
72. G. MOUROU and W. KNOX, "High-power switching with picosecond precision," Appl. Phys. Lett., 35-7, pp. 492-495, 1979.
73. K. K. LI, J. R. WHINNERY, and A. DIENES, "Optical switches for generation and pulse shaping of ultrashort electrical pulses," SPIE Proc. Picosecond Lasers and Applications, vol. 322, pp. 124-130, 1982.
74. D. H. AUSTON, "Impulse response of photoconductors in transmission lines," IEEE J. Quan. Elec., QE-19, pp. 639-648, 1983.
75. See for example: Picosecond Phenomena III, K. B. Eisenthal, R. M. Hochstrasser, W. Kaiser, and A. Laubereau eds., Springer Verlag, New York 1982.
76. Here, we refer to an ideal mathematical situation that does not include any experimental limiting effects.
77. K. MEYER, Private Comm., (Significant noise roll-off occurs near 4 MHz for the argon pumped CPM laser system.)